EMBEDDED PROTOSTARS IN THE DUST, ICE, AND GAS IN TIME (DIGIT) *HERSCHEL* KEY PROGRAM: CONTINUUM SEDs, AND AN INVENTORY OF CHARACTERISTIC FAR-INFRARED LINES FROM PACS SPECTROSCOPY*

Joel D. Green[1], Neal J. Evans II[1], Jes K. Jørgensen[2,3], Gregory J. Herczeg[4,5], Lars E. Kristensen[6,7], Jeong-Eun Lee[8], Odysseas Dionatos[2,3,9], Umut A. Yildiz[6], Colette Salyk[10], Gwendolyn Meeus[11], Jeroen Bouwman[12], Ruud Visser[13], Edwin A. Bergin[13], Ewine F. van Dishoeck[5,6], Michelle R. Rascati[1], Agata Karska[5], Tim A. van Kempen[6,14], Michael M. Dunham[15], Johan E. Lindberg[2,3], and Davide Fedele[5]

and

the DIGIT Team[1]

[1] Department of Astronomy, The University of Texas at Austin, 2515 Speedway, Stop C1400, Austin, TX 78712-1205, USA; joel@astro.as.utexas.edu
[2] Niels Bohr Institute, University of Copenhagen, DK-2100 Copenhagen, Denmark
[3] Centre for Star and Planet Formation, Natural History Museum of Denmark, University of Copenhagen, DK-1350 Copenhagen, Denmark
[4] Kavli Institute for Astronomy and Astrophysics, Peking University, Beijing 100871, China
[5] Max-Planck Institute for Extraterrestrial Physics, Postfach 1312, D-85741 Garching, Germany
[6] Leiden Observatory, Leiden University, P.O. Box 9513, 2300-RA Leiden, The Netherlands
[7] Harvard-Smithsonian Center for Astrophysics, 60 Garden Street, Cambridge, MA 02183, USA
[8] Department of Astronomy and Space Science, Kyung Hee University, Gyeonggi 446-701, Korea
[9] Department of Astronomy, University of Vienna, Türkenschanzstrasse 17, A-1180 Vienna, Austria
[10] National Optical Astronomy Observatory, 950 North Cherry Avenue, Tucson, AZ 85719, USA
[11] Dpt. Fisica Teorica, Universidad Autonoma de Madrid, Campus Cantoblanco, E-28049 Madrid, Spain
[12] Max Planck Institute for Astronomy, D-69117 Heidelberg, Germany
[13] Department of Astronomy, University of Michigan, 500 Church Street, Ann Arbor, MI 48109-1042, USA
[14] Joint ALMA Offices, Av. Alonso de Cordova 3107, Santiago, Chile
[15] Department of Astronomy, Yale University, New Haven, CT 06511, USA

ABSTRACT

We present 50–210 μm spectral scans of 30 Class 0/I protostellar sources, obtained with *Herschel*-PACS, and 0.5–1000 μm spectral energy distributions, as part of the Dust, Ice, and Gas in Time Key Program. Some sources exhibit up to 75 H_2O lines ranging in excitation energy from 100 to 2000 K, 12 transitions of OH, and CO rotational lines ranging from $J = 14 \rightarrow 13$ up to $J = 40 \rightarrow 39$. [O I] is detected in all but one source in the entire sample; among the sources with detectable [O I] are two very low luminosity objects. The mean 63/145 μm [O I] flux ratio is 17.2 ± 9.2. The [O I] 63 μm line correlates with L_{bol}, but not with the time-averaged outflow rate derived from low-J CO maps. [C II] emission is in general not local to the source. The sample L_{bol} increased by 1.25 (1.06) and T_{bol} decreased to 0.96 (0.96) of mean (median) values with the inclusion of the *Herschel* data. Most CO rotational diagrams are characterized by two optically thin components ($\langle \mathcal{N} \rangle = (0.70 \pm 1.12) \times 10^{49}$ total particles). $\mathcal{N}_{CO}$ correlates strongly with L_{bol}, but neither T_{rot} nor $\mathcal{N}_{CO}(\text{warm})/\mathcal{N}_{CO}(\text{hot})$ correlates with L_{bol}, suggesting that the total excited gas is related to the current source luminosity, but that the excitation is primarily determined by the physics of the interaction (e.g., UV-heating/shocks). Rotational temperatures for H_2O ($\langle T_{rot} \rangle = 194 \pm 85$ K) and OH ($\langle T_{rot} \rangle = 183 \pm 117$ K) are generally lower than for CO, and much of the scatter in the observations about the best fit is attributed to differences in excitation conditions and optical depths among the detected lines.

Key words: circumstellar matter – stars: formation – stars: pre-main sequence – stars: winds, outflows – submillimeter: stars

Online-only material: color figures

1. INTRODUCTION

Embedded protostars represent a transition from the core collapse within molecular clouds to the eventual young star and protoplanetary disk system, revealed as the surrounding envelope is accreted and/or removed. Processes occurring in the protostellar stage of evolution determine the conditions in the disks, including the amount and nature of material available for planet formation in later stages of evolution. In a picture of episodic accretion (e.g., Dunham et al. 2010), the disk mass at the end of the protostellar phase may be determined by the phasing of the last burst of accretion onto the star and the end of infall. Tracing the physical processes in these systems will lead to a better understanding of the constraints on planet formation. Physical processes can be traced through a wealth of molecular, atomic, and ionic tracers available to optical, infrared (IR), and millimeter-wave telescopes.

Large samples of protostars in relatively nearby ($d \leqslant 300$ pc) clouds have been developed through recent surveys with the *Spitzer Space Telescope* (e.g., Evans et al. 2009; L. E. Allen et al. 2013, in preparation), along with ground-based surveys (e.g., Jørgensen et al. 2009; Dunham et al. 2013). We have selected a sample of well-studied protostars from these studies, including

---

both Class 0 and Class I objects. Class 0 and Class I sources are characterized observationally by rising spectral energy distributions (SEDs) between near-IR and mid-IR wavelengths.

In addition to the continuum emission, the far-IR/submillimeter bands contain numerous pure rotational transitions of the CO ladder, as well as OH and H_2O, and several fine structure lines, all useful tracers of gas content and properties. The transitions and collisional rates of these simple molecules are well understood (see, e.g., Yang et al. 2010; Neufeld 2012 for a recent update on CO). Thus these lines make excellent diagnostics of opacity, density, temperature, and shock velocities (e.g., Kaufman & Neufeld 1996; Flower & Pineau Des Forêts 2010) of the gas surrounding these systems.

The *Infrared Space Observatory* Long Wavelength Spectrograph (*ISO*/LWS) covered the 20–200 μm spectral region and was well-suited to study the warm ($T > 100$ K) region of protostellar envelopes, distinguishable from the ambient cloud typically probed in ground-based millimeter studies. *ISO*/LWS detected gas phase H_2O, high-J CO rotational transitions, and fine structure emission lines toward protostars and related sources (e.g., Lorenzetti et al. 1999, 2000; Giannini et al. 1999, 2001; Ceccarelli et al. 1999; Nisini et al. 2002). These lines are indicative of the innermost regions of the protostellar envelope, exposed to heating by the central object, and the outflow cavity region, where winds and jets may interact with the envelope and the surrounding cloud.

The *Herschel Space Observatory* (Pilbratt et al. 2010) provides greater spatial and spectral resolution, as well as sensitivity, allowing study of sources with weaker continuum and line emission. *Herschel* is an ESA space-based submillimeter telescope with a 3.5 m primary mirror. The *Herschel*-PACS spectrograph (Photodetector Array Camera and Spectrometer; Poglitsch et al. 2010) provides a generational improvement over the spectral range covered by *ISO*/LWS, and is complementary to the Infrared Spectrograph (IRS; Houck et al. 2004) on the *Spitzer Space Telescope* (Werner et al. 2004). *Spitzer*-IRS revealed a wealth of diagnostics in the mid-IR, at relatively low spectral ($R \sim 60$–600) and spatial ($2''$–$5''$) resolution. For example, H_2O and OH were detected in some protostars (Watson et al. 2007) but in transitions with typically greater critical densities than those detectable by *Herschel*. Combined with enhanced spatial resolution, this difference in excitation requirements can lead to significantly different conclusions on the origin of the emission without the context of the *Herschel* lines (Herczeg et al. 2012). Similarly while pure rotational lines of H_2 were detected with *Spitzer* in many regions (e.g., Maret et al. 2009), CO far-IR lines are often used as a tracer for the warm gas mass, through a conversion factor to H_2.

Fine structure lines are a third example: although [Fe II] and [Si II] were detected as tracers of outflow properties with *Spitzer* (e.g., Maret et al. 2009; Podio et al. 2012), a conversion factor to [O I] 63 μm ($^3P_1$–$^3P_2$) (Hollenbach 1985; Hollenbach & McKee 1989; Hollenbach 1997) was used to derive outflow rates; this [O I] line falls in the *Herschel* bands and can be used to inform models (e.g., Ceccarelli et al. 1997). *Herschel*'s spatial resolution ($9''$–$40''$) resolves envelopes around systems within a few hundred pc. *Herschel*-HIFI (Heterodyne Instrument for the Far Infrared; de Graauw et al. 2010) provides better than 1 km s^{-1} resolution.

In this work we present the first summary of results of the "Dust, Ice, and Gas in Time" (DIGIT; PI: N. Evans) Key Program survey of protostars. We consider the sample as a whole in characteristic spectral lines, using a standardized data reduction procedure for all targets, and analyze the differences in the continuum and gas over the full sample, presenting an overview of trends. Specific sources are detailed in individual papers; a paper including a full inventory of lines with post-mission *Herschel* data calibration will follow. In Section 2 we describe the sample in the context of other surveys, and describe the observations. In Section 3 we present our detailed data reduction method for acquiring accurate continuum SEDs and line fluxes. In Section 4 we present results and statistics for the sample. In Section 5 we analyze rotational diagrams for all detected molecular species. In Section 6 we present correlations among the detected and derived parameters. In Section 7 we consider the origin of the line emission. We conclude in Section 8.

2. OBSERVATIONS

The DIGIT program uses *Herschel* to achieve far-IR spectral coverage of protostars and more evolved young stellar objects in order to make a full inventory of their chemical tracers. The full DIGIT sample consists of 94 sources: 24 Herbig Ae/Be stars, 9 T Tauri stars, 30 protostars observed with PACS and HIFI spectroscopy, and an additional 31 weak-line T Tauri stars observed with PACS imaging. Cieza et al. (2013) presented the results for the weak-line T Tauri stars; various papers are summarizing the results on disks in the Herbig and T Tauri star spectroscopic survey (Sturm et al. 2013; Meeus et al. 2013; Fedele et al. 2013). In this paper we focus on the embedded protostar sample. We presented the first DIGIT observations of a protostar, DK Cha, in van Kempen et al. (2010a). The 30 object sample is drawn from previous studies (summarized by Lahuis et al. 2006), focusing on protostars with high-quality *Spitzer*-IRS 5–40 μm and UV, optical, IR, and submillimeter complementary data. Thus all of the sources in the DIGIT sample are well studied at other wavelengths, and many are part of ongoing studies with *Herschel* in other programs, especially in the Water in Star-Forming Regions with *Herschel* (WISH) program (van Dishoeck et al. 2011; see also Nisini et al. 2010; Kristensen et al. 2012; Karska et al. 2013; Wampfler et al. 2013). Specific outflow positions that are well separated from the central source positions are observed by, e.g., Lefloch et al. (2010), Vasta et al. (2012), Santangelo et al. (2012), Benedettini et al. (2012), and Tafalla et al. (2013). In this work we characterize the DIGIT sample as a whole, using a single standardized data reduction technique. A complementary sample of protostars from a single region (Orion) can be found in Manoj et al. (2013).

2.1. The Sample

The full DIGIT embedded protostellar sample consists of 30 Class 0/I targets. Two sources (IRS44 and IRS46) were observed in a single pointing centered on IRS46. These objects are selected from some of the nearest and best-studied molecular clouds: Taurus (140 pc; six targets), Ophiuchus (125 pc; seven targets), Perseus (230–250 pc; seven targets), R Corona Australis (130 pc; three targets), Serpens (429 pc; two targets), Chamaeleon (178 pc; one target), and four additional isolated cores. The sources span two orders of magnitude in luminosity, from 0.11 to 27.8 $L_\odot$, with bolometric temperatures spanning the Class 0/I divide from 27 to 592 K. Their L_{bol}/L_{submm} ranges from 5 to >10,000, with most (18/22 with well-constrained submillimeter data) falling between 10 and 1000. The full list of targets appears in Table 1 in order of observation and in Table 2 in order of right ascension.

Table 1
Observing Log

Source	Other Name	ObsID (Blue[a], Red[a] SEDs)	Date Obs.	HIFI ObsID	Notes
DK Cha	IRAS 12496-7650	1342188039, 1342188040	2009 Dec 10	. . .	Off-center
L1551-IRS5		1342192805 and	2010 Mar 26 and	. . .	
		1342229711	2011 Sep 24	. . .	
L1527	IRAS 04368+2557	1342192981, 1342192982	2010 Mar 29	. . .	Off-center
TMR 1	IRAS 04361+2547	1342192985, 1342192986	2010 Mar 29	. . .	Off-center
TMC 1A	IRAS 04362+2535	1342192987, 1342192988	2010 Mar 29	. . .	Off-center
Serpens-SMM3		1342193216, 1342193214	2010 Apr 2	. . .	Mult. sources
Serpens-SMM4		1342193217, 1342193215	2010 Apr 2	. . .	Mult. sources
L1455-IRS3	IRAS 03249+2957	1342204122, 1342204123	2010 Sep 8	1342202056	
RCrA-IRS7C		1342206990, 1342206989	2010 Oct 23	1342215843	Mult. sources
RCrA-IRS5A		1342207806, 1342207805	2010 Nov 1	. . .	Mult. sources
RCrA-IRS7B		1342207807, 1342207808	2010 Nov 2	1342215842	Mult. sources
B335		1342208889, 1342208888	2010 Nov 13	. . .	
L1157		1342208909, 1342208908	2010 Nov 13	. . .	
L1014		1342208911, 1342208912	2010 Nov 14	1342196408	
BHR 71		1342212230, 1342212231	2011 Jan 1	. . .	
L1448-MM		1342213683, 1342214675	2011 Feb 2 and 22	. . .	
VLA 1623-243		1342213918, 1342213917	2011 Feb 6	1342205298	
IRAS 03245+3002	L1455-IRS1	1342214677, 1342214676	2011 Feb 23	1342202057	
B1-c		1342216213, 1342216214	2011 Mar 4	1342203204	
L1489	IRAS 04016+2610	1342216216, 1342216215	2011 Mar 5	. . .	
IRAS 03301+3111	Perseus Bolo76	1342215668, 1342216181	2011 Mar 9 and 16	1342202070	
GSS30-IRS1		1342215678, 1342215679	2011 Mar 10	. . .	
B1-a		1342216182, 1342216183	2011 Mar 16	1342203203	
IRAM 04191+1522		1342216654, 1342216655	2011 Mar 23	1342203192	
TMC 1	IRAS 04381+2540	1342225803, 1342225804	2011 Aug 6	. . .	
WL12		1342228187, 1342228188	2011 Sep 5	1342205299	
IRS 63		1342228473, 1342228472	2011 Sep 11	. . .	
IRS 46		1342228474, 1342228475	2011 Sep 11	1342205301	Mult. sources
IRS 44[b]		1342228474, 1342228475	2011 Sep 11	1342205300[b]	Mult. sources
Elias 29		1342228519, 1342228520	2011 Sep 11	. . .	

Notes. Observations log for protostellar sources discussed in this work. If the centroid of the continuum source is more than 3″ distant from the center spaxel (and commanded coordinates), we note this as "off-center."
[a] Blue SEDs are simultaneous 50–75 and 100–150 μm observations; Red SEDs are simultaneous 70–105 and 140–210 μm observations.
[b] IRS 44 was observed in the same exposure as IRS 46, but centered 2 spaxels away from IRS 46.

We utilized two of the three instruments on *Herschel*: PACS and HIFI. The spectral resolving power ($\lambda/\Delta\lambda$) ranges from 1000 to 3000 for PACS and up to 10^7 for HIFI, depending on wavelength and the selected observing mode.

All 30 of the sources in this work were observed with PACS as part of DIGIT during Science Demonstration and Regular Science Phase Cycle 1 schedules between 2009 December and 2011 September. Thirteen sources in the DIGIT embedded sources sample were observed with HIFI at 557 GHz to survey the ground-state H_2O 1_{10}–1_{01} line. All of the DIGIT sources not observed with HIFI as part of DIGIT (17 sources) were observed in the WISH Key Program in similar, but slightly different, observing modes. These are discussed in Kristensen et al. (2012); here we present only the DIGIT portion of the sample (Section 4.3.1).

The sample includes a few outliers from the Class 0/I split. IRS46 appears to be an edge-on disk, perhaps a Stage II source with a Class I SED (Lahuis et al. 2006). GSS30-IRS1 had previously also been an edge-on disk candidate, but has been shown to be a protostar from submillimeter analysis (van Kempen et al. 2009). Additionally, DK Cha is often considered a borderline Class I/II source.

WISH has also observed specific [O I] CO, H_2O, and OH lines with PACS in the line observing mode for 8 of the 30 DIGIT sources (van Kempen et al. 2010b; Wampfler et al. 2010,

2013). These data sample only a small spectral window around a limited number of individual lines but with higher spectral sampling and somewhat higher sensitivity, which facilitates the detection of weak lines. Full PACS spectral scans have been performed within WISH for four Class 0 sources (Herczeg et al. 2012; Goicoechea et al. 2012).

2.2. Herschel-PACS

PACS is a 5×5 array of $9''.4 \times 9''.4$ spatial pixels (hereinafter referred to as "spaxels") covering the spectral range from 50 to 210 μm with $\lambda/\Delta\lambda \sim 1000$–3000, divided into four segments, covering $\lambda \sim 50$–75, 70–105, 100–145, and 140–210 μm. The PACS spatial resolution ranges from $\sim9''$ at the shortest wavelengths (50 μm) to $\sim18''$ at the longest (210 μm). The nominal pointing rms of the telescope is 2″. However, targets observed during certain periods show consistently greater offsets (see below).

For the DIGIT embedded sources sample we utilized the full range of PACS (50–210 μm) in two linked pointed chop/nod rangescans: a blue scan covering 50–75 and 100–150 μm (SED B2A + short R1); and a red scan covering 70–105 and 140–210 μm (SED B2B + long R1). We used six and four range repetitions respectively, for integration times of 6853 and 9088 s (a total of $\sim$16,000 s per target for the entire 50–210 μm scan); excluding overhead, 50% of the integration

Table 2
Source List

Source	Cloud	Dist. (pc)	R.A. (J2000)	Decl.	Pos. Ref.	Dist. Ref.
L1448-MM	Per	232[a]	$03^h25^m38\overset{s}{.}9$	$+30^d44^m05\overset{s}{.}4$	PROSAC	HI
IRAS 03245+3002	Per	250	$03^h27^m39\overset{s}{.}1$	$+30^d13^m03\overset{s}{.}1$	c2d	
L1455-IRS3	Per	250	$03^h28^m00\overset{s}{.}4$	$+30^d08^m01\overset{s}{.}3$	c2d	
IRAS 03301+3111	Per	250	$03^h33^m12\overset{s}{.}8$	$+31^d21^m24\overset{s}{.}2$	c2d	
B1-a	Per	250	$03^h33^m16\overset{s}{.}7$	$+31^d07^m55\overset{s}{.}2$	c2d	
B1-c	Per	250	$03^h33^m17\overset{s}{.}9$	$+31^d09^m31\overset{s}{.}9$	c2d	
L1489	Tau	140	$04^h04^m42\overset{s}{.}9$	$+26^d18^m56\overset{s}{.}3$	B	
IRAM 04191+1522	Tau	140	$04^h21^m56\overset{s}{.}9$	$+15^d29^m45\overset{s}{.}9$	D	
L1551-IRS5	Tau	140	$04^h31^m34\overset{s}{.}1$	$+18^d08^m04\overset{s}{.}9$	2MASS	
L1527	Tau	140	$04^h39^m53\overset{s}{.}9$	$+26^d03^m09\overset{s}{.}8$	PROSAC	
TMR 1	Tau	140	$04^h39^m13\overset{s}{.}9$	$+25^d53^m20\overset{s}{.}6$	H	
TMC 1A	Tau	140	$04^h39^m35\overset{s}{.}0$	$+25^d41^m45\overset{s}{.}5$	H	
TMC 1	Tau	140	$04^h41^m12\overset{s}{.}7$	$+25^d46^m35\overset{s}{.}9$	A	
BHR 71	Core	178	$12^h01^m36\overset{s}{.}3$	$-65^d08^m53\overset{s}{.}0$	c2d	
DK Cha	Cha	178	$12^h53^m17\overset{s}{.}2$	$-77^d07^m10\overset{s}{.}7$	c2d	
GSS30-IRS1	Oph	125	$16^h26^m21\overset{s}{.}4$	$-24^d23^m04\overset{s}{.}3$	c2d	
VLA 1623-243	Oph	125	$16^h26^m26\overset{s}{.}4$	$-24^d24^m30\overset{s}{.}0$	c2d	
WL12	Oph	125	$16^h26^m44\overset{s}{.}2$	$-24^d34^m48\overset{s}{.}4$	c2d	
Elias 29	Oph	125	$16^h27^m09\overset{s}{.}4$	$-24^d37^m18\overset{s}{.}6$	c2d	
IRS 46	Oph	125	$16^h27^m29\overset{s}{.}4$	$-24^d39^m16\overset{s}{.}1$	c2d	
IRS 44	Oph	125	as IRS46[b]	as IRS46[b]	c2d	
IRS 63	Oph	125	$16^h31^m35\overset{s}{.}6$	$-24^d01^m29\overset{s}{.}3$	c2d	
Serpens-SMM3	Ser	429[c]	$18^h29^m59\overset{s}{.}3$	$+01^d14^m01\overset{s}{.}7$	c2d	DZ
Serpens-SMM4	Ser	429[c]	$18^h29^m56\overset{s}{.}7$	$+01^d13^m17\overset{s}{.}2$	c2d	DZ
RCrA-IRS5A	CrA	130[d]	$19^h01^m48\overset{s}{.}1$	$-35^d57^m22\overset{s}{.}7$	N	NE
RCrA-IRS7C	CrA	130[d]	$19^h01^m55\overset{s}{.}3$	$-36^d57^m17\overset{s}{.}0$	L	NE
RCrA-IRS7B	CrA	130[d]	$19^h01^m56\overset{s}{.}4$	$-36^d57^m28\overset{s}{.}3$	L	NE
B335	Core	106[e]	$19^h37^m00\overset{s}{.}9$	$+07^d34^m09\overset{s}{.}7$	PROSAC	O
L1157	Core	325	$20^h39^m06\overset{s}{.}3$	$+68^d02^m16\overset{s}{.}0$	PROSAC	
L1014	Core	200	$21^h24^m07\overset{s}{.}5$	$+49^d59^m09\overset{s}{.}0$	Y	

Notes. List of protostellar sources discussed in this work by region, sorted by R.A. Coordinate reference code: D = Dunham et al. (2006); Y = Young et al. (2004); L = Lindberg et al. (2011); N = Nisini et al. (2005); H = Haisch et al. (2004); HI = Hirota et al. (2011); DZ = Dzib et al. (2010, 2011); O = Olofsson & Olofsson (2009); NE = Neuhäuser & Forbrich (2008); A = Apai et al. (2005); B = Brinch et al. (2007); c2d = Evans et al. (2009); Lahuis et al. (2010); PROSAC = Jørgensen et al. (2009).
[a] The distance to L1448-MM is reported as 232 pc by Hirota et al. (2011).
[b] IRS 44 was observed in the same exposure as IRS 46, but centered 2 spaxels away from IRS 46.
[c] The distance to Serpens was revised upward from 260 pc to 429 ± 2 pc in Dzib et al. (2010, 2011).
[d] The distance to RCrA was revised downward from 170 pc to 130 pc in Neuhäuser & Forbrich (2008).
[e] The distance to B335 was revised downward from 250 pc to 106 pc in (Olofsson & Olofsson 2009).

time is spent onsource and on sky. Thus the effective on-source integration times are 3088 and 4180 s, for the blue and red scans, respectively. The total on-source integration time to achieve the entire 50–210 μm scan is then 7268 s.

The telescope and sky background emission was subtracted using two nod positions $6'$ from the source in opposite directions. The telescope chopped between the source and nod positions, cycling every 1/8 of a second in a pre-determined pattern of on and off positions (Poglitsch et al. 2010) during the integration.

2.3. Herschel-HIFI

The HIFI observations targeting the H_2O 1_{10}–1_{01} line at 556.9 GHz were made with the wide-band spectrograph and high resolution spectrograph in Band 1b. The range of observed frequencies is 554.6–558.6 GHz (lower sideband) and 566.6–570.6 GHz (upper sideband). The observations were executed in single point mode using position switching with a $30'$ offset in both right ascension and declination and the total integration time was 1144 s per observation, with an effective on-source integration time of 318.6 s. The beam size of HIFI is diffraction limited at this frequency ($\sim 39''$; Roelfsema et al.

2012), and the uncertainty in frequency is less than 100 kHz, or 0.05 km s^{-1}.

The HIFI data are reduced in a manner similar to that described in Kristensen et al. (2012). The spectra were reduced in *Herschel* Interactive Processing Environment (HIPE) version 6.0 (Ott 2010) and exported to the "CLASS" analysis package for further reduction and analysis. The reduction consisted of subtracting linear baselines and averaging data from the H- and V-polarizations, the latter only after visual inspection of the data from the two polarizations. A main beam efficiency of 0.75 (Roelfsema et al. 2012) is adopted to convert from antenna temperature (T_A^*) to main beam temperature (T_{MB}), and integration over the line yields a value for the integrated intensity ($\int T_{MB} dv$). The final spectral rms noise is 8–13 mK for a binsize of 0.3 km s^{-1}.

3. DATA REDUCTION WITH PACS

We have two primary science goals for the DIGIT embedded sources sample. First, we want to produce the most reliable SEDs to inform models, better constraining source temperature

and density profiles. For this purpose, our criteria are: (1) the best match between spectral modules and (2) the best consistency with photometric measurements. Second, we want to measure line fluxes for as many gas lines as possible to constrain excitation conditions and chemical evolution of the gas phase emission. For this goal, our main criterion is the best signal-to-noise ratio (S/N) in narrow wavelength regions around lines. In the future, we hope to study weaker, broader features in the continuum emission that may constrain refractory dust and ice components, but the data reduction quality is not yet capable of this last point.

After extensive tests of various reduction methods with different versions of the HIPE program, we found that two different methods and HIPE versions (6.0 and 8.0) performed best in meeting the separate goals of achieving the most accurate SED and the best S/N for line emission. We combined the best features of both to get well-calibrated, low-noise line fluxes, as we summarize below; the full description may be found in Appendix A.

First, we apply a modified pipeline based on the default data reduction script for that version of HIPE. We used an oversampling rate of 2 (closely matching the raw data sampling rate, with 2 pixels per resolution element) in all sources except for our science demonstration phase target, DK Cha, for which we used an oversampling of 1. This target was observed in a slightly different setup not sufficiently sampled in wavelength to use an oversampling of 2; all of the other sources are Nyquist sampled. This process yields spectral cubes for each nod position, which are then averaged to produce the final pipeline data product.

At the edges of each segment, the noise increased greatly and the overall calibration became very erratic ($\lambda < 53.5 \mu$m, and 95.0μm $< \lambda < 102.5 \mu$m) due to decreased sensitivity and order confusion. At the longest wavelengths of PACS ($\lambda > 190 \mu$m), echoes of spectral lines appear at twice their actual wavelength, a side-effect of light leakage from the short wavelengths, combined with decreased sensitivity on the edge of the array. Thus neither the continuum nor the line emission is reliable at these wavelengths, and detections in these ranges are not further considered in this paper; a discussion can be found in the Appendix of Herczeg et al. (2012).

After this point, we used two different procedures, optimized to produce the best results for continuum and lines, respectively. This dual procedure was necessary to produce reliable absolute flux calibration, while also obtaining the best S/N on continuum and lines. For convenience, we refer to these two reductions as the "bgcal" (background calibrated; best for absolute flux calibration) and "calblock" (calibration block; best for S/N, or point-to-point flux calibration) spectra. These two processes are described in detail in Appendices A.1 and A.2. In the next two subsections, we summarize the analysis, including the post-processing needed to deal with the point-source profile (PSF) and extended emission, first for the continuum and then for lines.

3.1. Continuum Emission

The purpose of the steps described here is to produce a SED that can be compared to existing photometry and used to calibrate line fluxes derived from the other reduction. This process used the bgcal reduction, within HIPE 6.0. The individual steps in the reduction are detailed in Appendix A.3. In summary, we calibrate line fluxes from regions of good S/N to a separate determination of the absolute flux level and spectral shape, noting and accounting for extended emission and

mispointing effects. In the most complicated fields, we defer full analysis to individual source papers, as noted below.

First, we determined the centroid position of the continuum (using the HIPE 6.0 reduction) for two wavelength regions in each segment, selected to avoid detectable line emission. Using maps of these regions, we were able to interpolate a peak position to within 0.2 spaxel widths. We find by this method that most of the sources have continuum centroids that fall between 0″.2 and 3″.0 of the center coordinates, with the majority landing within 2″ (0.2 spaxel widths) of the center. For those sources, the pointing is consistent between the "blue" and "red" observations, independent observations executed at different times.

Second, in order to produce a spectrum with the best S/N and an accurate absolute flux density, we chose two apertures for each spectrum: a smaller aperture (S_{sm}) chosen for the best S/N, and a larger aperture (S_{lg}) that included all of the source flux for calibration. To do this, we summed the flux in spaxels containing high-S/N spectra of the source continuum, producing a single spectrum. In most cases, we simply use the central spaxel for this purpose. For some sources we measured a centroid offset from the center of greater than 0.2 spaxels. In particular, the series of DIGIT observations taken between 2010 March 29 and April 2 were consistently offset by 6″, generally to the upper left of the central spaxel. In these cases we extracted a 2×2 spaxel area centered on the apparent centroid location of the central source from the PACS continuum emission, and scaled it to the full 25 spaxel continuum values. We applied this technique to DK Cha, TMR 1, and L1527 (Table 1). In the case of TMC 1A, which was slightly less offset, we used only the two brightest spaxels for the centroid.

Third, we determined the largest set of spaxels containing the source without contamination from other sources in the field-of-view; in most cases this was the full 5×5 array, but in some cases we selected a smaller set of spaxels (see section on extended emission, below). We then computed the flux density summed over these spaxels (the total flux). Fourth, we fitted a second (or smaller) order polynomial scaling factor in wavelength, determined from the ratio of the flux density in the larger aperture to that in the smaller aperture. Then we scaled the spectrum by this correction factor.

This correction is applied module-by-module (e.g., a separate polynomial for each range of 50–75, 70–95, 100–145, and 145–190 μm). After scaling S_{sm} to S_{lg}, the two "blue" (50–75 and 70–95 μm) and the two "red" (100–145 and 145–190 μm) modules were generally well aligned with each other (less than 5% difference on average), but retained the S/N of S_{sm}. Unfortunately, even after applying this entire procedure, S_{lg}(red) $> S_{lg}$(blue) in all cases, a systematic discontinuity at 100 μm for every source. This jump was not uniform; it is most problematic for faint continuum sources IRS63, IRAS 03301, B1-a, L1014, and WL12. Ultimately the SEDs will benefit from comparison to PACS photometry.

Furthermore, there are a few cases where the reduction process did not produce a smooth continuum across modules even within the "blue" or "red" halves. In cases with a significant misalignment, as an optional sixth step we apply an additional correction. The sources that are significantly misaligned between modules are Serpens-SMM3 and SMM4, RCrA-IRS5A, 7B, IRS 46, L1551-IRS5, L1455-IRS3, and L1014. The Serpens and R CrA sources are in highly confused regions; an analysis of PACS 70/100/160 μm imaging can be found in Sicilia-Aguilar et al. (2013). Serpens-SMM3 is the most

Table 3
PACS Photometric/Spectroscopic Flux Calibration

Source	Flux Ratio (70 μm)	Flux Ratio (160 μm)
HD 163296	1.042	0.842
HD 135344	0.982	0.873
HD 104237	1.017	1.179
HD 139614	1.120	0.992
HD 142527	1.283	1.263
HD 36112	1.149	0.893
HD 100453	1.166	1.000
HD 179218	0.991	0.929
IRS 48	1.039	1.040
HD 100546	0.930	0.925
Mean	1.071	0.993
Std. Dev.	0.106	0.136

Notes. Absolute flux calibration from PACS spectroscopy compared to PACS photometry for pointlike Herbig Ae/Be stars in the DIGIT and GASPS disks samples, respectively. The ratios are the photometric value divided by the spectroscopic value, using HIPE 6.0 ("bgcal") calibration.

Figure 1. Comparison of B335 PACS spectroscopy (rebinned to low resolution to remove line emission) and PACS photometry (A. Stutz 2012, private communication), at similar aperture sizes. The PACS photometry is taken from circular apertures of radius 5″3, 15″9, and 26″5, equivalent to 9″4 (black-blue), 28″2 (dark blue), and 47″0 (light blue) squares. The dash lines indicate linear interpolations for the spectra at 100 μm. These sizes are comparable to the central spaxel only, central 3×3 spaxels, and all 25 spaxels, respectively. The agreement is good to better than 10%, except for the central spaxel. The central spectrum is higher than the PACS photometry by 30% at 100 μm.

(A color version of this figure is available in the online journal.)

problematic; the B2A/short R1 observation is 30% higher than the B2B/long R1 observation, probably an effect of the complicated interaction between the extended emission in the region, and the PSF; once again we scaled the B2A/short R1 spectrum up by 30%. IRS46 is complicated by emission from the much brighter nearby source IRS 44. The L1551-IRS5 B2A/short R1 observation is 10% higher than the B2B/long R1 observation, which was observed 1.5 yr later. We scaled up the B2B/long R1 by 10% to match the B2A/short R1 data, for the continuum SEDs. L1455-IRS3 and L1014 are only marginally detected in the continuum; thus when scaling to the full array the noise becomes comparable to the signal, causing the scaling to become unreliable. In this case we scaled the brightest module (the blue half of each observation) to the full array as usual and then scaled the red halves upward by a factor of two to match the blue. This exercise shows that in the case of very faint sources absolute calibration using the full array becomes unreliable. No other additional continuum scaling was performed on any of the other sources in the sample after this point.

In a few cases, we observed clear evidence of *multiple* emitting sources within the PACS field-of-view. In the case of VLA 1623-243 we detected a clear second source to the northeast edge of the grid (Appendix B, Figure 27(h)), and avoided the emission from those spaxels. This is consistent with the emission from the Oph-A ridge detected in SCUBA maps (Wilson et al. 1999; Johnstone et al. 2000). IRS 46 is well-centered, but by design IRS 44 occupies only the southwestern 3 spaxels in the map, which greatly underestimates the true flux density of IRS 44 and distorts the spectral shape. In these cases, we selected spaxels most likely to be attributable to the target source. We extracted the central source, and scaled to the flux in the spaxels clearly attributed to that source; in some cases this amounted to only 60% of the spaxels. In the case of IRS 44 we extracted the flux from only the southwestern 3 spaxels. In the complicated Serpens-SMM3/4 and the RCrA-IRS7B/7C fields we observed significant extended diffuse emission contributing to the flux. We therefore calibrated these to flux density per pixel and detailed analysis will be presented by Dionatos et al. (2013) and J. E. Lindberg et al. (2013, in preparation). In the case of L1448-MM, we were able to decompose the flux based
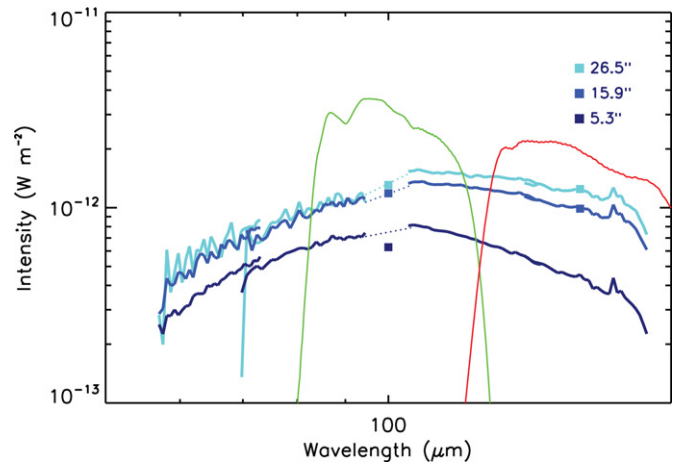
on resolved observations at shorter wavelengths (see the section on continuum analysis for further detail, and Lee et al. 2013).

3.1.1. Absolute Flux Calibration

Comparison to previous photometry in the PACS wavelength range is problematic. The *IRAS* beam was much larger, and MIPS data often suffered from saturation on these sources. The typical MIPS 70 μm flux density is almost always low compared with the PACS spectra extracted from the full array by $\sim$20%, except in the brighter half of our sample, where the MIPS value is even lower—a factor of two—compared with the *Herschel* data.

Instead, we compared SEDs from this reduction method to PACS photometry of disk sources, obtained in the GASPS (PI: W. Dent) Key Program. These isolated point sources provide a better photometric test than the extended, embedded sources. We convolved our SEDs to the transmission curve for each PACS photometric filter and compared the photometry to the resulting spectrophotometry (Table 3). We found the best agreement with HIPE 6.0 using the bgcal reduction, for which we found the following average factors for photometry/spectrophotometry: 1.071 ± 0.106 at 70 μm, and 0.993 ± 0.136 at 160 μm, where the second number is the standard deviation over 10 sources. Eventually, PACS photometry for our embedded sources should become available from other programs. For now, we were able to compare to PACS photometry for one embedded source, B335 (A. Stutz 2012, private communication; Launhardt et al. 2013). The SEDs derived from various combinations of spaxels (central spaxel only, central 3×3 spaxels, and total from all spaxels) are compared to PACS photometry in apertures set to match the solid angle in Figure 1; e.g., circular apertures of radius 5″3, 15″9, and 26″5, equivalent to 9″4 (black-blue), 28″2 (dark blue), and 47″0 (light blue) squares. The spectral flux density at 100 μm was determined from a linear interpolation between the average flux density in the 94–95 μm, and 104–105 μm ranges. The agreement is good to 10%, except for the central spaxel, where the photometric aperture size (10″6 diameter) is very close to

the beam size at $100 \mu m$ ($\sim 10''$) and much less than the beam size at $160 \mu m$ ($\sim 14''$). The extent of the source is well reflected in the rise of flux density as we add increasing numbers of spaxels, but the images show that the emission continues to still larger scales. If this situation is general, our SEDs will underestimate the total flux from the source.

3.2. Line Emission

Our reduction technique for lines utilizes HIPE 6.0 *and* HIPE version 8.0.2489 with the "calibration block," referred to as the "calblock" reduction, which multiplies the chopped spectrum by a similar spectrum of an on-board calibration source. It works in a similar fashion to the continuum procedure, but with several key differences. The steps in the reduction are detailed in Appendix A.4.

Our objective here is to measure line equivalent widths (EWs) for gas phase lines, which are spectrally unresolved, or in a few cases, perhaps slightly resolved. This reduction produced the lowest local (point-to-point) noise but larger shifts between modules and an overall calibration less consistent with photometry. Tests indicate that the EW of lines is independent of reduction. Consequently, we use the calblock reduction to define the EW of lines and then use the bgcal reduction of the same spectral region to convert to line fluxes. This process allows us to combine the best S/N on the EW from HIPE 8.0.v2489 with the best overall line flux calibration using HIPE 6.0. The first step is to extract line fluxes from the HIPE 8 calblock reduction using a narrow region to define the continuum (S_λ) and calculate the EW. We utilized a modified version of the SMART reduction package (Higdon et al. 2004) to fit Gaussians and first- or second-order baselines to the spectra to remove local continuum features. The LAMDA database of lines (Schöier et al. 2005), supplemented by HITRAN (Rothman et al. 2005), was used to identify the features. The fit for the line center varies only by $0.01 \mu m$ or less for our different extraction methods (10%–20% of a resolution element); therefore, the fit uncertainty in velocity space is ~ 30–50 km s^{-1}. Line centers usually lie within 50 km s^{-1} of the theoretical line center from laboratory measurements. At our level of precision, we do not observe believable shifts in our data; nonetheless, our observed shifts are still consistent with shifts observed in other datasets (e.g., Karska et al. 2013). However, the location of the source within each slit also affects the velocity. The uncertainty in EW caused by the fit is quite small (S/N ratios as high as 300 were obtained on bright lines, particularly [O I]), but for faint lines, the uncertainty rises to 20%. In this treatment we do not include lines within the masked wavelength regions ($<55 \mu m$, 95–$102.5 \mu m$, $>190 \mu m$) as they exhibit large calibration uncertainties. The one exception is the CO $J = 27 \rightarrow 26$ line at $96.77 \mu m$; the local rms uncertainty is somewhat larger than, but still comparable to, the local continuum surrounding the CO $J = 28 \rightarrow 27$ line at $93.3 \mu m$, and we only include this line in sources with confirmed detections of CO lines at shorter wavelengths. The line does not significantly affect the derived source properties in the following sections.

3.2.1. Corrections for Spatial Extent, and Comparison to the Empirical PSF

Second, the line fluxes were corrected for PSF and extended emission. As with the continuum, simply adding all the spaxels caused a serious loss of S/N and a diminished rate of line detection, and the PSF correction provided in the standard pipeline does not account for extended emission. Thus we do not use the PSF correction function, but instead compare the flux over different sized apertures to determine an empirical correction for each source. In order to do this, we measured the line flux, $F_{\rm line}({\rm sm})$, in the central spaxel (or a sum over a few spaxels for poorly centered sources) that gave the best S/N on relatively strong lines. Mathematically, the process is identical to the continuum, except for line flux rather than flux density.

Additionally, we correct the fluxes by the ratio between the bgcal and calblock local continuum for each individual line. Because the spatial distribution of line emission could in principle differ from that of the continuum, we did not simply scale the value in the central spaxel by the continuum ratios. To determine the total line fluxes, $F_{\rm line}({\rm lg})$, we applied a polynomial correction, developed by comparing the spectral line flux detected in the central spaxel compared to that in the surrounding spaxels for strong lines—mostly CO lines, but also including strong H_2O lines, a technique developed by Karska et al. (2013). We did not include the 63 and $145 \mu m$ [O I] lines in this correction, because they were frequently extended compared to these species and to the PSF (see Section 3.1). Weaker lines of all species were then scaled with the same factors.

This method assumes that weak and strong lines have similar spatial distributions. In Figure 2, we plot line fluxes of all species measured from 3×3 spaxel regions versus line fluxes contained within just the central spaxel, for four well-pointed sources. For each source we fit a constant ratio from 50 to $100 \mu m$, and a first order polynomial from 100–$200 \mu m$, a simplified fitted version of the PSF correction, to the bright CO and H_2O lines. For this exercise we set a minimum correction factor of 1.4 to the 50–$100 \mu m$ fit, approximately the PSF correction. Although additional lines are plotted, they are not considered in the fit. In the first two cases (L1489 and Elias 29), the pipeline-provided PSF correction (dashed line) is very similar to the analytical correction. In Elias 29, the [O I] (purple) emission exceeds the PSF by a significant margin, indicating that it is extended compared with the PSF. In the third case, BHR71, we find that all line ratios significantly exceed the PSF correction, suggesting a substantial contribution from extended and/or diffuse emission in the field-of-view. In GSS30-IRS1, we find that the long wavelength line emission exceeds the PSF, as does the continuum; at short wavelengths the [O I] line is far more extended than the molecular emission or the continuum (see below). This may be associated with an HCO$^+$ flow extending to the NE from the source position (Jørgensen et al. 2009).

In cases for which we lack sufficient strong lines to determine the correction, we use a linear approximation to the PSF correction. This was applied to IRAS 03245, IRAS 03301, IRAM 04191, IRS 46, IRS 63, L1014, and L1455-IRS3. We also correct IRS 44 with the PSF, but note that the final derived flux is still close to an order of magnitude too low, judging by the *Spitzer* spectra and long wavelength photometry. This is due to the position of the source just off the edge of the PACS footprint; we do not fully see the source peak and lose substantial flux.

4. RESULTS

4.1. Detection Limits

We measured the continuum rms in selected (line-free) portions of the spectrum. The measured rms uncertainties are dominated by three factors. Second-order (B2A and B2B; 50–75 and 70–$105 \mu m$, respectively) spectra have $\sim$ sixfold higher noise for a constant spectral width, at the given integration
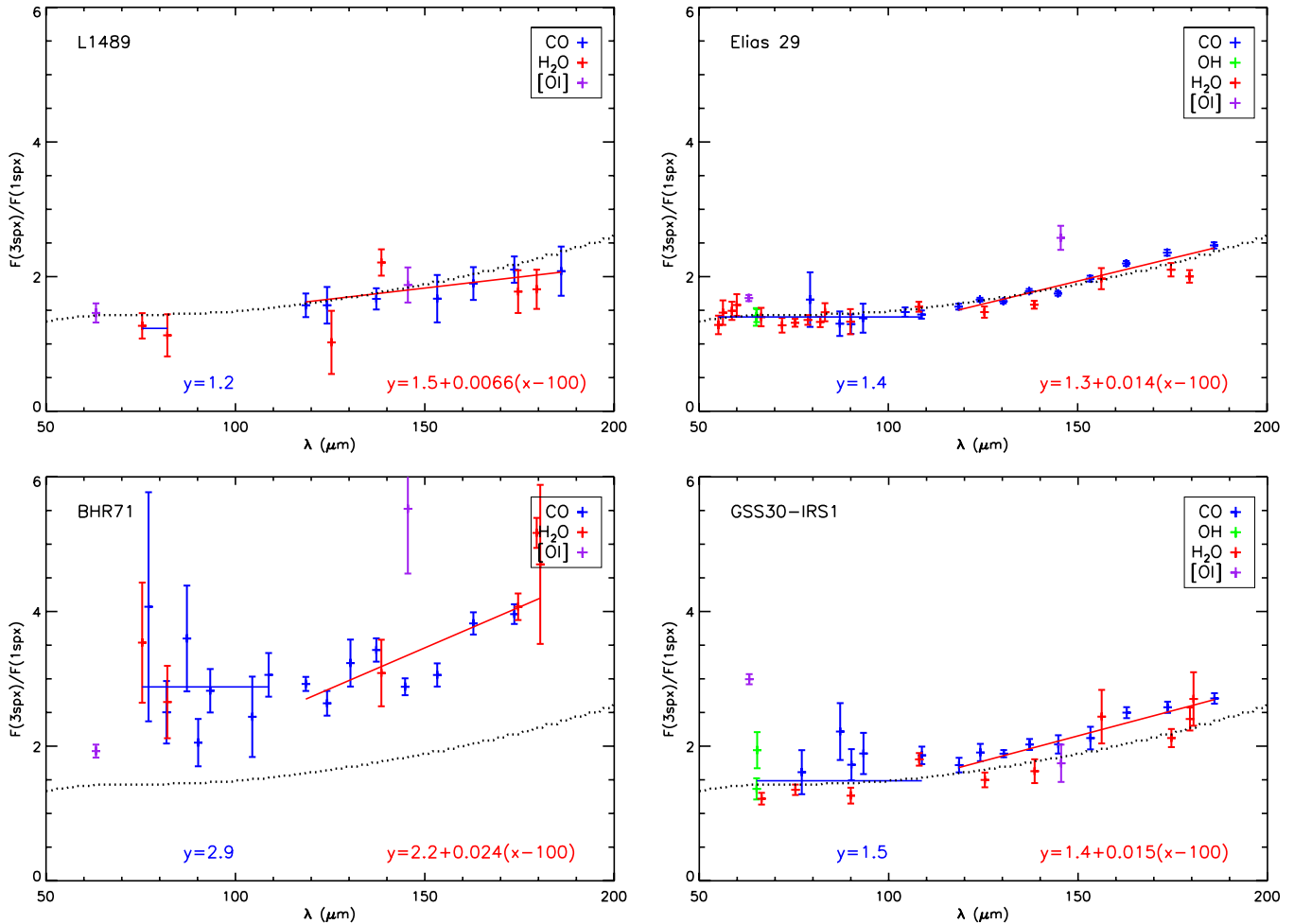
Figure 2. Ratio of the flux of various lines in the 3×3 aperture to the flux from the central spaxel only is plotted vs. wavelength, for L1489 (top left), Elias 29 (top right), BHR71 (bottom left), and GSS30 (bottom right). A constant ratio is fitted to all lines between 50 and 120 μm (solid blue line), and a first-order polynomial to lines between 120 and 200 μm (solid red line). For comparison we plot the pipeline aperture correction function for the PSF (black dashed curve). For this analysis we have selected CO (red) and H_2O (blue) lines only in selected regions of high S/N, ignored blended lines, and *excluded* OH (green), [O I] (purple) and [C II] lines (not shown). In L1489, applying the PSF correction would roughly predict the ratio of 3×3 to the central spaxel, for all detected species. In Elias 29, the [O I] emission is extended compared with the CO and H_2O lines. In BHR71, all lines appear extended, evidence of multiple or diffuse source contributions. In GSS30, the line emission marginally exceeds the PSF overall, with notable differences between species.

(A color version of this figure is available in the online journal.)

time/repetition settings. Figure 3 shows the rms uncertainties versus wavelength for a line-rich source (Elias 29) separated by order, for both CO and H_2O lines, using fitted Gaussian linewidths. The uncertainties in flux are independent of species (unsurprisingly) and broadly decrease with increasing wavelength, discontinuously at the order boundaries. Portions of the spectra within 5 μm of the order edges have far higher uncertainties. Finally, we show the rms uncertainties for the 63 μm [O I] line across the full DIGIT sample, against the local continuum flux. Above a certain continuum strength—greater than $\sim 3 \times 10^{-16}$ W m^{-2} at 63 μm—the rms uncertainty rises roughly linearly with continuum flux, reaching 70×10^{-18} W m^{-2} at a continuum flux of 4000×10^{-18} W m^{-2}. Thus the S/N of lines and the continuum seem to reach a maximum at ~ 60, compared with the continuum rms noise.

4.2. Continuum Results: SEDs

Analysis of the continuum yields several interesting comparisons. In brief, the classification of sources is altered only slightly, but systematically, by the inclusion of the *Herschel* data. Figures 4–8 show the SEDs of our sample over the en-

tire wavelength range with available data. We plot available photometry for comparison, in the following order of precedence: PACS photometry from other programs, *Spitzer*-MIPS photometry (with arrows for lower limits due to saturation), *ISO* photometry, and *IRAS* photometry. Where available, we include *Spitzer*-IRS spectroscopy from the "IRS_Disks" Instrument Team (Furlan et al. 2006) and "Cores to Disks" Legacy (Lahuis et al. 2006, 2010; Boogert et al. 2008) programs. In the case of L1448-MM, *Spitzer*-IRAC/IRS and submillimeter data were used to determine the flux ratio between the two components (separated by 8″, comparable to the PACS beam at the shortest wavelength; Jørgensen et al. 2006). Extracting a separate spectrum from each spaxel in PACS, and from IRS maps, we present in Figure 9 the decomposed SEDs of L1448-MM(A) or (C), and L1448-MM(B) or (S). (S), the southern source, appears to be fainter and bluer than (C). The separated sources are discussed in detail in Lee et al. (2013). For the remainder of our analysis in this paper, we consider the combined SED.

Using our spectral data, along with photometric data for wavelengths not covered by *Herschel*, we have recalculated the bolometric luminosities (L_{bol}) and temperatures (T_{bol}) for the
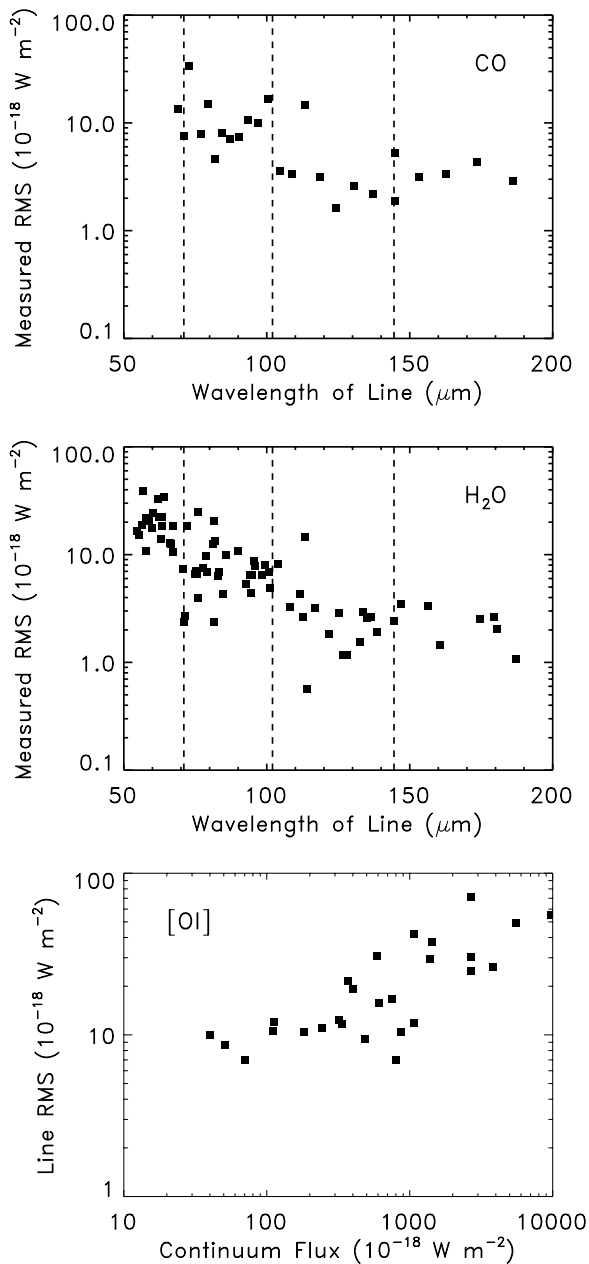
Figure 3. rms uncertainties of measured CO (top left) and H_2O (top right) lines for Elias 29. The dashed lines indicate transitions between the B2A, B2B, and R1 (short and long wavelength) modules. In cases for which a significantly different rms uncertainty is measured for lines in the overlap regions, we choose the higher S/N measurement. The point at 113 μm is a blend of CO and H_2O, and appears consistently high in all sources, even those without detectable H_2O emission. The uncertainties generally decrease to the 100 μm breakpoint, and then flatten to a lower single value ($\sim 3 \times 10^{-18}$ W m^{-2}) for $\lambda > 100\,\mu$m. Bottom: rms uncertainties measured from the [O I] 63 μm line for each source, vs. the flux of the surrounding continuum for the same measured linewidth. Although the uncertainty is flat at low continuum flux, the uncertainty rises steadily at fluxes $> 3 \times 10^{-16}$ W m^{-2}, with a corresponding rise in the detection limit.

sample, using standard definitions (Myers & Ladd 1993) and the calculation algorithm from Dunham et al. (2010). In summary, L_{bol} is the luminosity integrated over the entire SED, while T_{bol} is the temperature of a blackbody with a flux-weighted mean frequency equal to that of the observed SED. The weights of the points are proportional to the fraction of the SED they cover ("trapezoidal" weighting); thus individual points in the PACS and IRS spectra receive little weight relative to the photometric points in sparsely covered regions of the SED.

The dashed lines in the SED plots show a blackbody at T_{bol}; these resemble the full SED only for sources of low T_{bol} with little near-IR emission. Of course, T_{bol} is not meant to fit the SED, but only to characterize it with a single parameter. The values of L_{bol} and T_{bol} with and without *Herschel* data are given in Table 4. The mean, median, and standard deviation of L_{bol}(wHer)/L_{bol}(w/oHer) are 1.25, 1.06, and 0.66, after removing those five with multiple known emitting sources (RCrA-IRS5A, 7B, and 7C, Serpens-SMM3 and SMM4). The mean, median, and standard deviation of T_{bol}(wHer)/T_{bol}(w/oHer) for the sample are 0.96, 0.96, and 0.21, respectively. The sample means now are $\langle L_{bol}\rangle = 6.1\ L_\odot$ and $\langle T_{bol}\rangle = 167$ K. Figure 10 shows the new distribution in L_{bol}–T_{bol} space, plotted alongside the "without *Herschel*" distribution. The sample still represents sources spanning two orders of magnitude in bolometric temperature, and 2.5 orders of magnitude in bolometric luminosity. Using the standard 70 K Class 0/I boundary (Chen et al. 1995), we now have nine Class 0 sources and 16 Class I sources (previously eight and 17, respectively, Table 4), with B1-c and BHR71 shifting across the boundary from Class I to 0, and L1014 shifting from Class 0 to I.

There is some uncertainty in the value of T_{bol}, which is affected by the data at wavelengths shorter than PACS wavelengths, because the short-wavelength data are more extinguished (characterized broadly in similar sources by Dunham et al. 2013), and vary over multiple epochs of observation. Thus different values for the near-IR/optical photometry strongly affect T_{bol} but not L_{bol}. In the case of L1455-IRS3, literature values for $\lambda < 70\,\mu$m were an order of magnitude too high. Investigation revealed these data to be associated with stronger nearby sources, and thus we exclude them from the SED. Despite these uncertainties, our measurements for T_{bol} and L_{bol} are generally consistent with Karska et al. (2013). There are six sources that show substantial (>20%) shifts in this space. GSS30-IRS1, IRS46, L1014, L1455-IRS3, all show substantial decrease in T_{bol} and increase in L_{bol} while VLA1623 shows the reverse effect. Of these five sources, VLA1623 is the only source that falls on the Class 0 side of the T_{bol} line, while the other four fall on the Class I side. IRS44 shows the reverse trend of the four Class I sources; this is due to its position on the edge of the array footprint, as noted earlier, missing a large amount of flux; the IRS 44 PACS flux is too low by a factor of a few even after applying the typical PSF correction. Thus we conclude that overall the PACS data is substantially increasing the derived luminosity in bluer sources for which it samples the peak and longer wavelengths. *Spitzer*-MIPS and *IRAS* photometry were previously used to sample this region; the MIPS data is often close to saturation in these sources. Without the PACS data, one will consistently derive lower L_{bol}, and higher T_{bol}, in Class I sources.

Another diagnostic of evolutionary state is L_{bol}/L_{submm}. By this metric, a source with $L_{bol}/L_{submm} < 200$ is Class 0. Using this criteria, our original sample consisted of 16 Class 0 and nine Class I sources, rather than eight and 17, respectively, even when including three sources (BHR71, IRS 44, and IRS46) lacking submillimeter under Class I. This total was unchanged by the addition of *Herschel*-PACS data. The Class 0 sources under this definition include all of the Class 0 sources from the T_{bol} diagnostic (except BHR71, which lacked submillimeter data to be classified) and nine additional sources identified as Class I by T_{bol}. The submillimeter luminosity diagnostic is also stable with respect to what data are included, as long as sufficient submillimeter data are available, and evolutionary
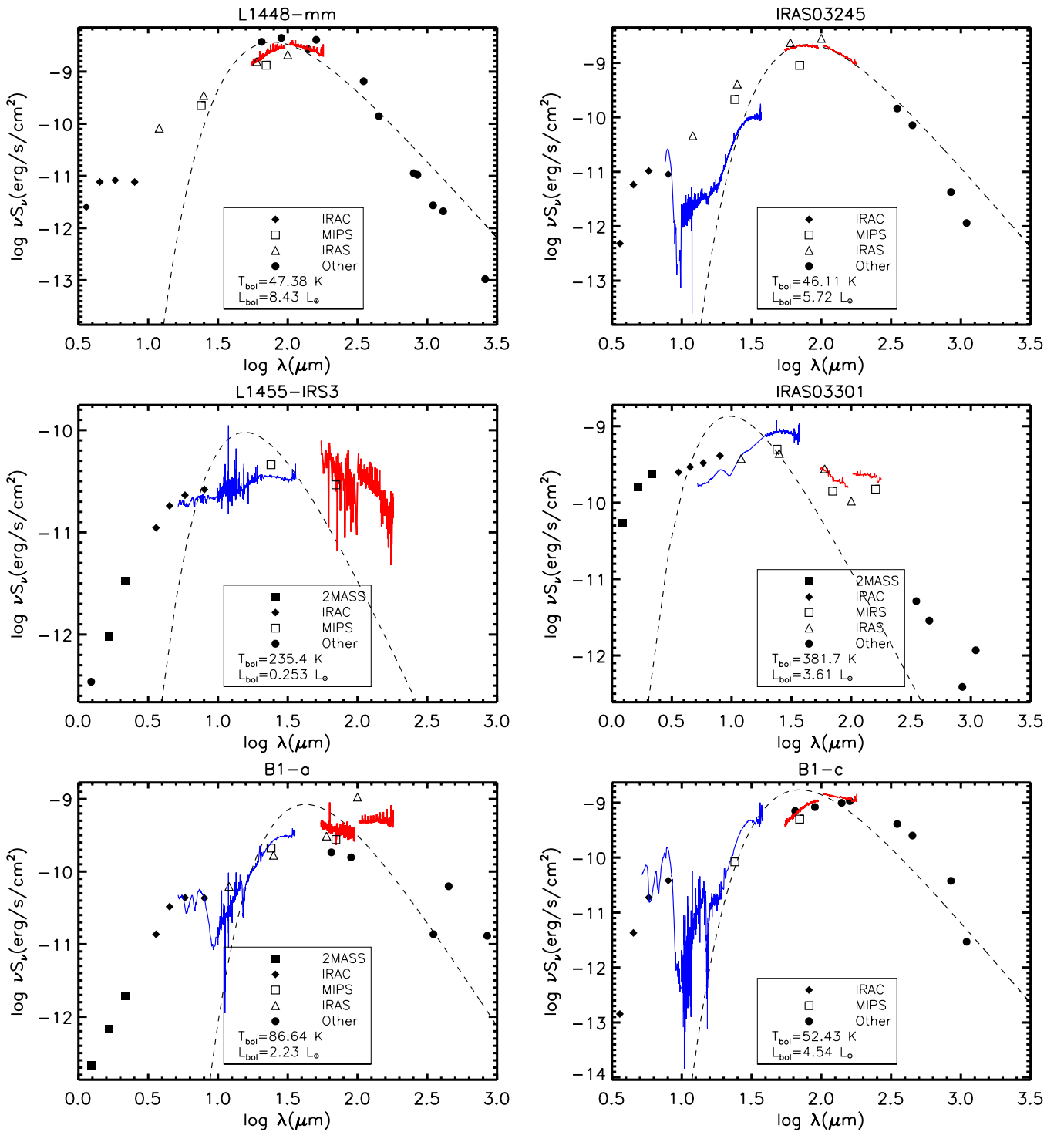
Figure 4. 0.5–1000 μm SEDs. The IR photometric points are primarily from Two Micron All Sky Survey (2MASS, JHK; filled squares), *Spitzer*-IRAC (3.6, 4.5, 5.8, 8.0 μm; filled diamonds), *IRAS* (12, 25, and 100 μm; open triangles), *ISO* (10, 13, 15, 20, 25 μm; open diamonds), and *Spitzer*-MIPS (24, 70 μm; open squares). The MIPS 70 μm point is frequently saturated and falls below the PACS spectrum. The submillimeter are from SHARC-II (350 μm; Wu et al. 2007), BOLOCAM (1.1, 1.2 mm; Enoch et al. 2006), SCUBA (450, 850 μm; Di Francesco et al. 2008; Visser et al. 2002), *AKARI* (9, 18 μm; IRSA catalog), IRAM (1.3 mm; Motte & André 2001), and SEST (1.2, 1.3 mm; various). The blue spectrum is 10–36 μm *Spitzer*-IRS, from the "c2d" legacy program (Lahuis et al. 2006; Enoch et al. 2009) and the "IRS_Disks" GTO program (Furlan et al. 2006). For cases in which the SH (10–20 μm) and LH (20–36 μm) spectra do not match in flux, we have scaled the SH to the larger aperture LH. The red spectrum is the PACS data (this work). The dashed line is a blackbody spectrum for the measured values of L_{bol} and T_{bol} (this work). (A color version of this figure is available in the online journal.)

models indicate that it is a better guide to the evolutionary stage (Young & Evans 2005), though both indicators become less reliable in models with episodic accretion (Dunham et al. 2010). However, we chose to focus on the T_{bol} classification for

two reasons: first, for straightforward comparison to the existing work (e.g., Manoj et al. 2013; Karska et al. 2013), and second, as we lack sufficient data to classify all of our sources by the L_{bol}/L_{submm} method.
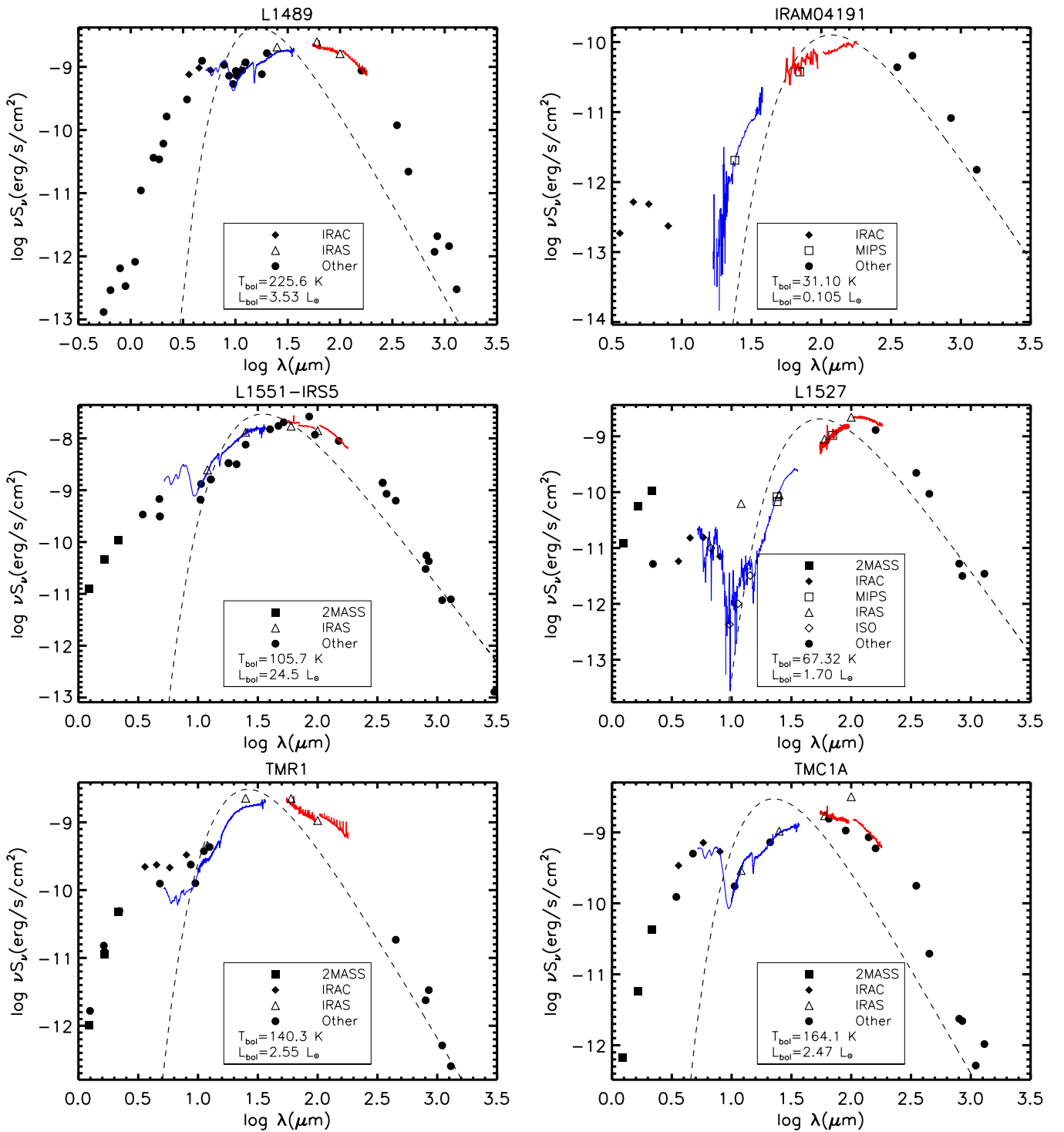
Figure 5. 0.5–1000 μm SEDs, as in Figure 4.
(A color version of this figure is available in the online journal.)

4.3. Lines: Atomic and Molecular Emission

4.3.1. Detection Statistics

In general, the PACS spectra are very rich in line emission, including [O I], CO, OH, and H_2O emission lines, and absorption only in two sources (in OH 119 μm) and diffuse [C II]. Spectra characteristic of three kinds of sources, classified by their highest J CO line observed, are shown after removal of the continuum (Figures 11–13). Although the sources are classified by their CO emission, there are aspects of other lines common to each subset. L1014 (Figure 11) has almost no line emission, with only [O I] at 63 μm detected. The lack of CO is a significant non-detection; by contrast, the faintest source in our sample (IRAM04191) does show CO emission. L1551-IRS5 (Figure 12)—one of the most luminous sources in our sample—shows more lines, including 15 CO lines, 13 H_2O lines and the two lowest energy OH doublets in the 3/2–3/2 ladder at 84 and 119 μm; unusually, the lowest excitation OH
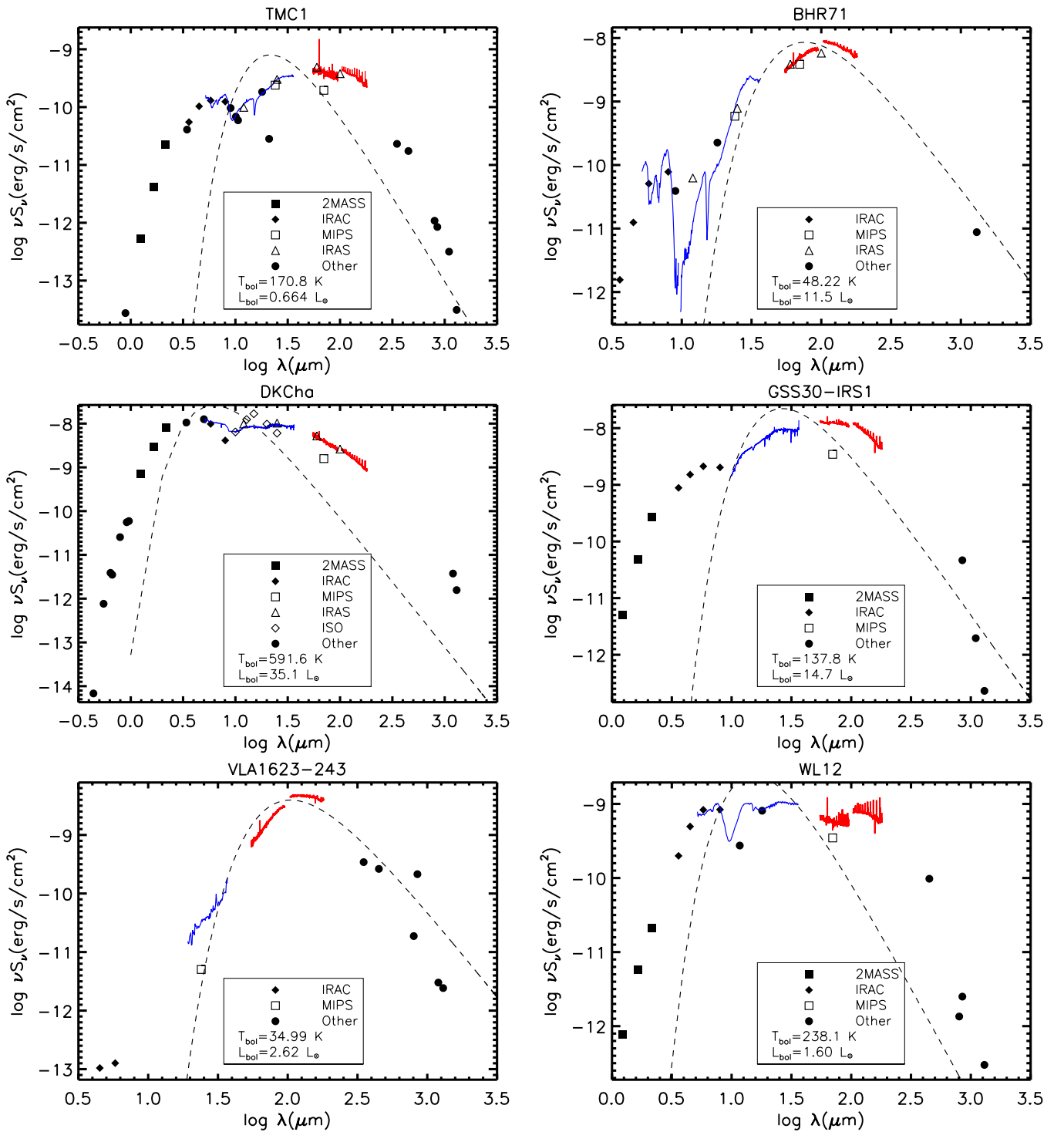
Figure 6. 0.5–1000 μm SEDs, as in Figure 4.
(A color version of this figure is available in the online journal.)

doublet at 119 μm is in absorption. Finally, Elias 29 (Figure 13) shows the richest spectrum in the sample, with 25 CO lines (ranging from $J = 13 \rightarrow 12$ up to CO $J = 38 \rightarrow 37$; $E_u = E_{upper}/k$, expressed in Kelvin, of 503–4080 K), 18 OH lines (in eight resolved pairs from two different ladders, and four blended or cross-ladder transitions ($E_u = 121$–875 K), and 74 lines of H_2O including one blended pair ($E_u = 114$–1729 K). No atomic species other than [O I] ($^3P_1$–$^3P_2$ and $^3P_0$–$^3P_1$) and [C II] ($^2P_{3/2}$–$^2P_{1/2}$) and no molecular species other than

CO, OH, and H_2O have so far been identified in any of these spectra.

The measured line fluxes for seven characteristic lines are shown in Table 5, including corrections for extended emission (see Section 4.3.1, below). A full inventory of lines will appear in a later paper including the final post-mission *Herschel* calibration dataset. The lines selected as characteristic are as follows: [O I] at 63.18 μm, CO $J = 29 \rightarrow 28$ at 90.16 μm, CO $J = 16 \rightarrow 15$ at 162.81 μm, OH 3/2-3/2 (7/2+ $\rightarrow$ 5/2−) at
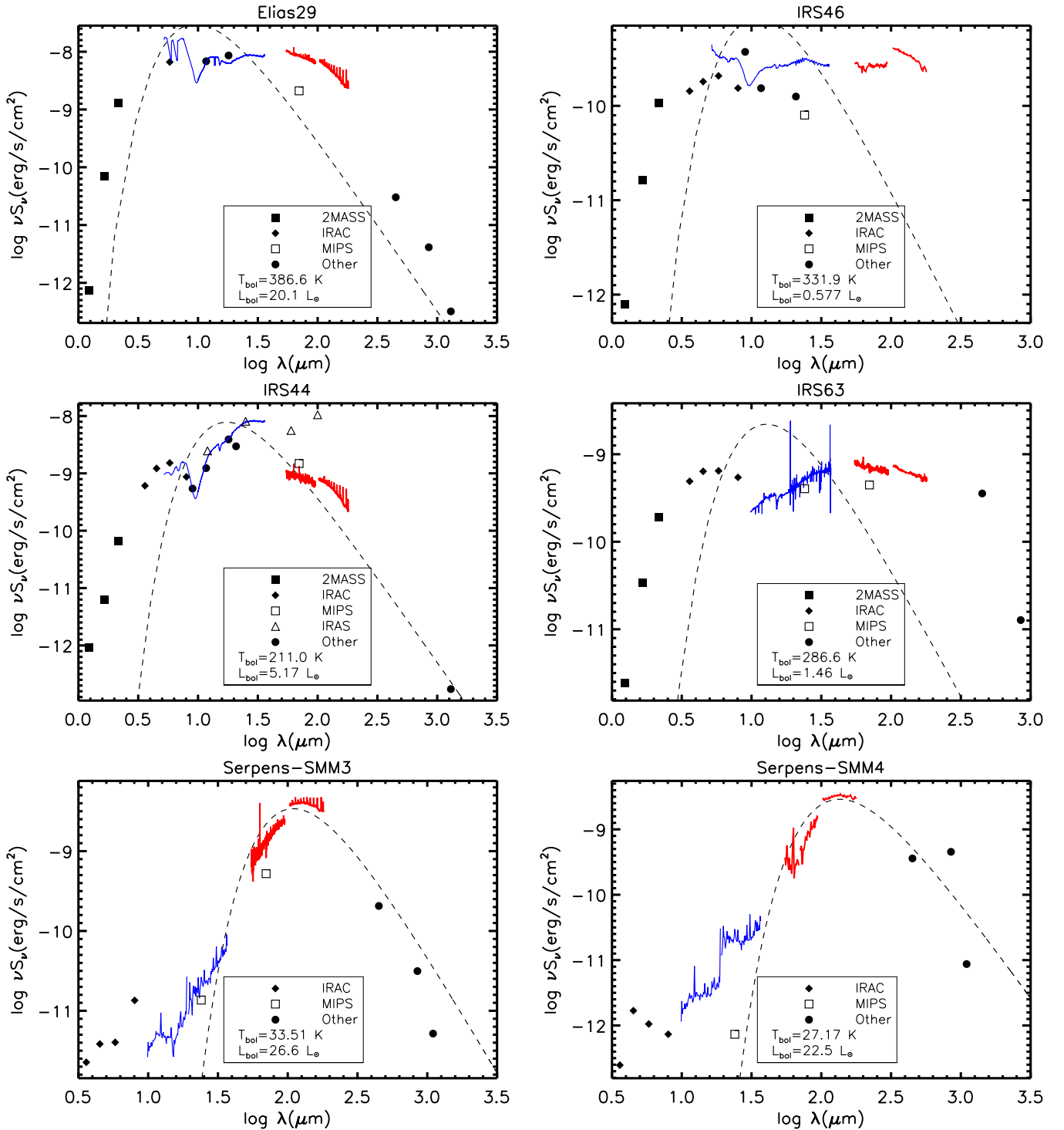
Figure 7. 0.5–1000 μm SEDs, as in Figure 4. IRS44 is not corrected for PSF or its location on the edge of the PACS array.
(A color version of this figure is available in the online journal.)

84.61 μm, OH 3/2–3/2 (9/2+ $\rightarrow$ 7/2−) at 65.28 μm, ortho-H_2O ($2_{12} \rightarrow 1_{01}$) at 179.53 μm, and ortho-H_2O ($3_{30} \rightarrow 2_{21}$) at 66.44 μm. These lines were chosen to represent species and/or excitation above the ground state, quantified by E_u, and roughly characterized as "cool" ($E_u < 300$ K), "warm" ($E_u \sim 500$ K), and "hot" ($E_u > 1000$ K). Although both OH lines are doublets, the individual lines in the selected transitions are cleanly resolved at the resolution of PACS. We avoided the 119 μm doublet because it is complicated in at least

two sources (L1551-IRS5 and B1-c) by apparent foreground absorption.

All 30 sources have at least one detected line, including the two very low luminosity objects (L1014 and IRAM04191). The most universal is the [O I] line at 63 μm, detected in 29 of 30 sources (only B1-c lacks a detection of this line). [O I] at 145 μm is also detected in 24 of these 29 sources. The [C II] emission line at 158 μm is also widely seen, and in some cases (DK Cha, IRAM04191, and TMC1) is spatially coincident with the local
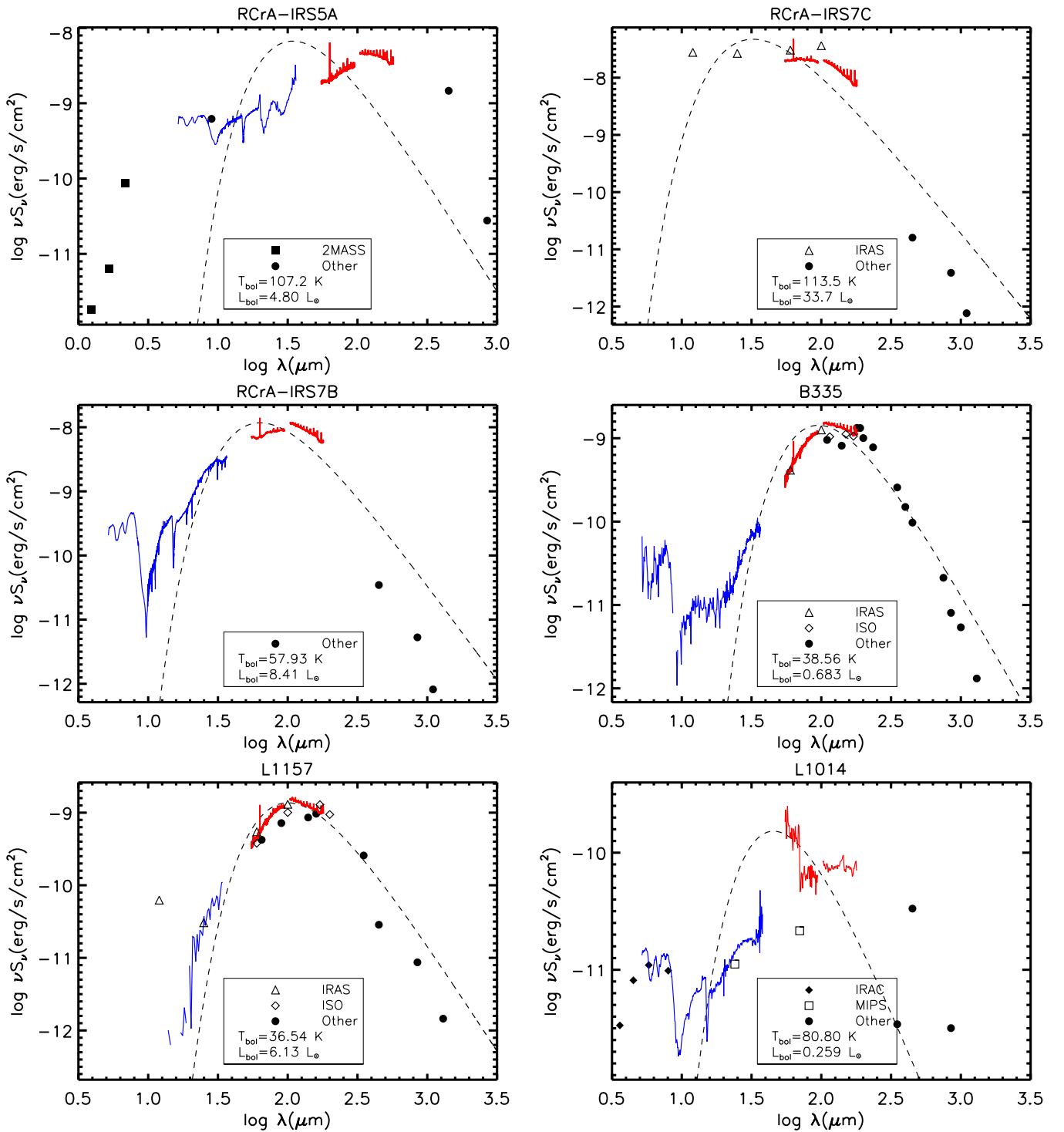
Figure 8. 0.5–1000 μm SEDs, as in Figure 4. L1014 is not detected in continuum emission at $\lambda < 75\,\mu$m.

(A color version of this figure is available in the online journal.)

continuum and with the [O I] emission. More often the peak emission is offset, and in several cases appears in absorption, indicating stronger emission in the reference position. When seen in emission, it shows little correlation with the continuum or other lines. We conclude that it mostly arises from the general cloud and is not related to the source. We do not consider it further in this paper.

Across the full sample, the detection of "warm" CO ($J = 16 \rightarrow 15$; $E_u = 752$ K) is nearly universal, appearing in 27

of 30 sources (including IRAM04191, but not the slightly more luminous L1014). Most of these (22/27) also show "hot" CO ($J = 29 \rightarrow 28$; $E_u = 2400$ K). Similarly, the "cool" o-H_2O $J_{K_{-1}K_{+1}} = 2_{21} \rightarrow 1_{01}$ line at 179.5 μm ($E_u = 114$ K) is detected in 23 of 30 sources, while the "warm" o-H_2O line at 66.5 μm ($E_u = 411$ K) is detected in 14/23 of these. "Cool" OH 3/2–3/2 (7/2+ $\rightarrow$ 5/2−) at 84.61 μm ($E_u = 291$ K) appears in 27 of 30 sources, whereas "warm" OH at 65.28 μm ($E_u = 511$) appears in 15/27 of these. When higher excitation lines of a given species
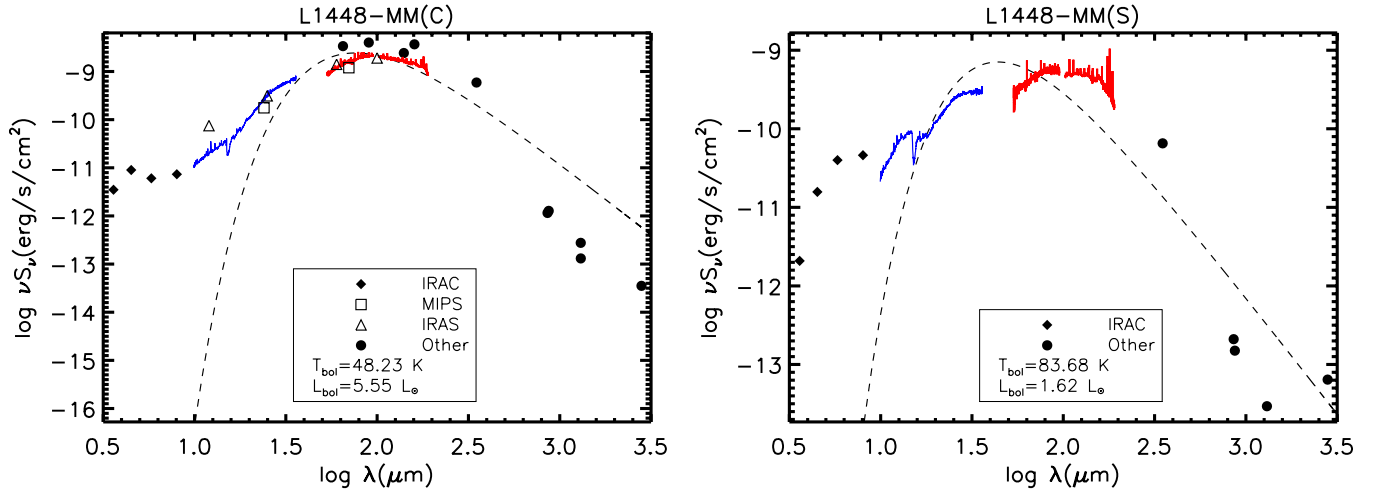
Figure 9. 0.5–3000 μm SED of L1448-MM, decomposed into sources C and S, with unresolved photometry ($\lambda > 8\,\mu$m) weighted by the ratio of their IRAC 8 μm flux densities. *Spitzer*-IRS spectra are extracted from separate pointings, and the SH (10–20 μm) spectrum is scaled up to match the LH (20–36 μm) spectrum.
(A color version of this figure is available in the online journal.)

Table 4
Bolometric Luminosities and Temperatures

Source	$L_{\rm bol}$ (wHer) ($L_\odot$)	$T_{\rm bol}$ (wHer) (K)	$L_{\rm bol}$ (w/oHer) ($L_\odot$)	$T_{\rm bol}$ (w/oHer) (K)	$L_{\rm bol}/L_{\rm submm}$
L1448-MM	8.4	47	4.4	69	38
IRAS 03245+3002	5.7	46	4.2	59	64
L1455-IRS3	0.32	204	0.3	221	18
IRAS 03301+3111	3.6	382	3.2	438	903
B1-a	2.4	88	1.5	132	39
B1-c	4.5	52	1.8	76	14
L1489	3.5	226	3.7	238	259
IRAM 04191+1522	0.11	31	0.11	24	5
L1551-IRS5	24.5	106	28	97	107
L1527	1.7	67	2.0	36	45
TMR 1	2.6	140	3.7	144	734
TMC 1A	2.5	164	2.2	172	143
TMC 1	0.66	171	0.7	139	114
BHR71	9.7	55	7.1	84	. . .
DK Cha	27.8	592	27.7	565	>10000
GSS30-IRS1	14.5	138	4.4	254	5150
VLA1623-243	2.6	35	1.0	35	30
WL12	1.6	238	2.6	440	145
Elias 29	20.1	387	4.8	383	4215
IRS 46	0.5	352	0.8	633	. . .
IRS 44	5.1	213	. . .	. . .	. . .
IRS 63	1.5	287	1.6	580	33
B335	0.68	39	0.54	37	27
L1157	6.5	40	6.0	42	44
L1014	0.26	81	0.21	64	14

Notes. Recalculated bolometric luminosity and temperature for the DIGIT embedded sources sample, including *Herschel*-PACS data in the fit. The bolometric luminosities (both old and new) for B335 and L1448-MM are adjusted to the new distances. The ratio of $L_{\rm bol}/L_{\rm submm}$ is derived using a submillimeter cutoff wavelength of 350 μm. Values for confused regions (Serpens and R CrA) are presented in subsequent papers, as noted in the text.

appear, the lower excitation lines are always present. OH and H_2O emission are both commonly detected but not always in the same source: 23 of 27 sources with OH also have H_2O emission at 179 μm, but L1551-IRS5, IRAM04191, L1455-IRS3, and IRS 63 all show some OH emission but no H_2O; B1-c is the only source with H_2O emission but no detected OH emission. Note that we do not see a "cool" component of CO with PACS; we reserve the term for the observed ~100 K component with SPIRE and HIFI (Yıldız et al. 2012; Goicoechea et al. 2012;

L. E. Kristensen et al. 2013, in preparation; J. D. Green et al. 2013, in preparation).

The DIGIT HIFI data add spectrally resolved measurements of the emission in a low excitation line of H_2O: $J_{K_{-1}K_{+1}} = 1_{10} \rightarrow 1_{01}$ at 557 GHz ($E_{\rm u} = 60$ K). In Figure 14 we show the line profiles from each source. We detect H_2O in 9 of 13 sources, 3 of which show an inverse P Cygni profile. The sources without line detections are IRAM04191, L1014, IRAS03301, and L1455-IRS3. Additionally, WL12 and IRAS03245 are

Table 5
Line Fluxes

Source	CO $J = 29 \rightarrow 28$ 90.16 μm (10^{-18} W m^{-2})	CO $J = 16 \rightarrow 15$ 162.83 μm	OH 65.28 μm	OH 84.61 μm	H_2O 66.45 μm	H_2O 179.53 μm	[O I] 63.18 μm	H_2O 557 GHz $\int T_{MB} dv$ (K km s^{-1})
L1448-MM	197 ± 26	574 ± 12	163 ± 14	232 ± 16	76 ± 31	2147 ± 71	760 ± 33	
IRAS 03245	20 ± 6	50 ± 5	<49	47 ± 4	<28	17 ± 1	96 ± 9	0.50 ± 0.02
L1455-IRS3	<25	<15	<22	33 ± 10	<20	<18	17 ± 3	<0.08
IRAS 03301	35 ± 10	38 ± 5	145 ± 33	146 ± 5	57 ± 14	29 ± 6	324 ± 14	<0.08
B1-a	<33	51 ± 6	73 ± 7	81 ± 6	29 ± 4	70 ± 12	298 ± 12	1.51 ± 0.02
B1-c	<63	85 ± 10	<74	<74	<68	334 ± 11	<116	5.41 ± 0.05
L1489	24 ± 3	76 ± 6	67 ± 8	63 ± 8	59 ± 12	72 ± 7	405 ± 15	
IRAM 04191	<27	19 ± 4	<25	32 ± 6	<33	<10	75 ± 9	<0.08
L1551-IRS5	61 ± 11	138 ± 7	<165	164 ± 36	<93	<32	7194 ± 110	
L1527	<25	30 ± 6	<28	59 ± 15	<27	51 ± 5	483 ± 27	
TMR1	58 ± 15	137 ± 5	129 ± 16	141 ± 11	134 ± 26	36 ± 5	594 ± 35	
TMC1A	37 ± 7	37 ± 4	67 ± 17	60 ± 9	<12	14 ± 2	682 ± 19	
TMC1	45 ± 4	69 ± 7	104 ± 15	101 ± 11	20 ± 4	33 ± 5	837 ± 14	
BHR71	319 ± 16	624 ± 21	89 ± 9	116 ± 20	<63	447 ± 14	2350 ± 77	
DK Cha	280 ± 11	440 ± 23	269 ± 24	321 ± 16	<34	106 ± 6	2702 ± 53	
GSS30	164 ± 11	374 ± 9	224 ± 15	229 ± 9	362 ± 13	234 ± 15	1720 ± 22	
VLA1623	94 ± 18	185 ± 16	<41	105 ± 6	<39	123 ± 10	658 ± 41	5.71 ± 0.04
WL12	38 ± 5	85 ± 3	59 ± 2	95 ± 7	52 ± 5	27 ± 5	441 ± 14	0.20 ± 0.01
Elias29	199 ± 9	535 ± 6	457 ± 5	615 ± 13	355 ± 15	185 ± 5	1787 ± 33	
IRS46	<24	17 ± 3	<29	<30	<25	<13	60 ± 13	1.26 ± 0.02
IRS44	77 ± 23	473 ± 9	<118	175 ± 31	172 ± 30	232 ± 13	887 ± 52	3.21 ± 0.03
IRS63	<28	<12	<24	17 ± 3	<24	<13	190 ± 12	
B335	24 ± 4	131 ± 4	<31	48 ± 5	<27	80 ± 5	381 ± 15	
L1157	48 ± 6	141 ± 6	<34	72 ± 12	23 ± 4	187 ± 6	532 ± 15	
L1014	<25	<18	<29	<29	<27	<20	123 ± 13	<0.08

Notes. Census of selected lines in the sample, corrected for extended emission: CO $J = 29 \rightarrow 28$, representing the hot component; CO $J = 16 \rightarrow 15$, representing the warm component; OH 84.61 μm; H_2O 179.53 μm, representing low-lying states of their respective species; OH 65.28 μm, H_2O 66.45 μm, representing higher states; [O I], tracing excited gas in the disk, envelope, and outflow. 3σ upper limits are given for non-detected lines, accounting for the PSF correction. The final column lists integrated intensities for the 557 GHz H_2O line for sources observed with HIFI in the DIGIT embedded sources sample; for HIFI non-detections, we provide 3σ upper limits assuming a width of 20 km s^{-1}.
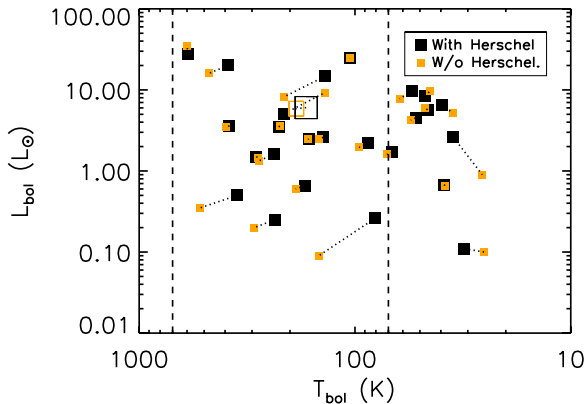

Figure 10. The distribution in L_{bol} and T_{bol} before (orange small squares) and after (black large squares) supplementing the SEDs with the DIGIT PACS data. The vertical dashed lines represent the Class 0/I and I/II boundaries. The hollow squares are the sample means before (small orange) and after (large black). Dotted lines connect each source in the distribution.

(A color version of this figure is available in the online journal.)

marginal detections. IRAM04191, L1014, and L1455-IRS3 are three of the faintest sources in our sample. However IRAS03245 is considerably more luminous than IRS46 and B1-a, both of which show strong detections. The integrated intensities are tabulated in the last column of Table 5. Eight of nine sources with 557 GHz H_2O detections also show the H_2O 179 μm line, the sole exception being IRS46, which suffers from confusion with IRS44. It is possible that the H_2O in the

IRS46 HIFI data is related to IRS44; the PACS map suggests that IRS44 is the main source of molecular emission in the region. IRAS03301 has a rich PACS H_2O spectrum, but a very weak 179 μm H_2O line, and no detection with HIFI. The reverse is slightly more common: L1551-IRS5 and IRS63 both show detections with HIFI (Kristensen et al. 2012)—the latter very faint—but no H_2O 179 μm emission with PACS in our sample.

4.3.2. Spatial Extent of Continuum and Line Emission

The PACS data were taken as a single footprint, so the data are not designed for detailed analysis of spatial structure. We discuss here some simple metrics regarding spatial extent and discuss a few examples of interesting structure.

The simplest metric of spatial extent is the ratio of the emission from the central 3×3 spaxels to the emission from the central (highest S/N) spaxel. We have used this metric to scale the spectrum from the central spaxel (Section 3.2), and by comparing this ratio to that of a point source, we can roughly characterize the extent of emission.

We characterize source extent across the sample with this metric, for both continuum and the characteristic lines, in Tables 6 and 7. Signs of extended emission are seen in both line and continuum in some sources, and the line emission is not always coupled to the continuum, but many sources are essentially pointlike at *Herschel* wavelengths. To simplify the comparison, we consider only the 15 sources in our sample that are well centered (we exclude DK Cha, TMR1, TMC1A,

Table 6
Line and Continuum Spatial Extent

Source	CO $J = 29 \rightarrow 28$	CO $J = 16 \rightarrow 15$	OH 65.28 μm	OH 84.61 μm
PSF	1.45	2.04	1.43	1.45
IRAS 03245	...	$2.24 \pm 0.28\ (2.42 \pm 0.03)$	...	...
IRAS 03301	...	...	$1.36 \pm 0.35\ (2.96 \pm 0.75)$	$1.33 \pm 0.19\ (1.20 \pm 0.41)$
B1-a	...	$2.44 \pm 0.45\ (3.67 \pm 0.17)$	$1.77 \pm 0.41\ (1.78 \pm 0.11)$	$1.29 \pm 0.18\ (1.38 \pm 0.24)$
B1-c	...	$3.50 \pm 0.47\ (2.06 \pm 0.03)$	...	...
L1489	...	$1.91 \pm 0.23\ (2.10 \pm 0.04)$	$2.24 \pm 0.45\ (1.45 \pm 0.03)$	$1.37 \pm 0.44\ (1.48 \pm 0.04)$
L1551-IRS5	$1.19 \pm 0.35\ (1.80 \pm 0.01)$	$1.62 \pm 0.19\ (2.55 \pm 0.01)$	...	$1.33 \pm 0.39\ (1.58 \pm 0.01)$
TMC 1	...	$2.25 \pm 0.18\ (2.36 \pm 0.17)$	...	$0.96 \pm 0.28\ (1.48 \pm 0.20)$
BHR71	$2.09 \pm 0.31\ (2.63 \pm 0.02)$	$3.15 \pm 0.14\ (3.59 \pm 0.03)$	...	$1.18 \pm 0.47\ (2.56 \pm 0.02)$
GSS30-IRS1	$1.67 \pm 0.19\ (2.89 \pm 0.02)$	$2.51 \pm 0.08\ (5.34 \pm 0.06)$	$1.71 \pm 0.19\ (2.23 \pm 0.01)$	$1.58 \pm 0.15\ (2.80 \pm 0.22)$
VLA1623	...	$3.36 \pm 0.32\ (4.30 \pm 0.05)$	...	$2.48 \pm 0.35\ (2.74 \pm 0.03)$
WL12	...	$1.99 \pm 0.17\ (3.60 \pm 0.14)$	...	$1.29 \pm 0.25\ (1.41 \pm 0.13)$
Elias 29	$1.29 \pm 0.13\ (2.25 \pm 0.02)$	$2.14 \pm 0.03\ (3.98 \pm 0.04)$	$1.42 \pm 0.06\ (1.82 \pm 0.01)$	$1.42 \pm 0.08\ (2.16 \pm 0.38)$
IRS 63	...	...	...	...
B335	...	$1.88 \pm 0.14\ (2.30 \pm 0.03)$	...	...
L1157	...	$1.90 \pm 0.14\ (1.93 \pm 0.03)$	...	...

Notes. Comparison of spatial extent for lines and local continuum for the 15 well-centered sources with no known source confusion at the resolution of *Herschel*. Each entry is a pair of values: the ratio of the line flux in the central 3×3 spaxels over the line flux in the central spaxel, and in parentheses the ratio of the average continuum flux density in the central 3×3 spaxels over the continuum flux in the central spaxel, in a selected range of wavelengths near the line. Formal errors are provided for each line ratio, but systematic calibration uncertainties and spaxel-to-spaxel variation are not included.

Table 7
Line and Continuum Spatial Extent

Source	H$_2$O 66.45 μm	H$_2$O 179.53 μm	[O I] 63.18 μm
PSF	1.43	2.27	1.43
IRAS 03245	...	...	$2.95 \pm 0.45\ (1.47 \pm 0.04)$
IRAS 03301	...	...	$1.37 \pm 0.10\ (2.23 \pm 0.29)$
B1-a	$4.23 \pm 1.26\ (1.69 \pm 0.80)$	$2.99 \pm 0.63\ (4.68 \pm 0.41)$	$2.86 \pm 0.16\ (1.81 \pm 0.15)$
B1-c	...	$3.44 \pm 0.13\ (2.27 \pm 0.03)$	...
L1489	...	$1.81 \pm 0.27\ (2.25 \pm 0.06)$	$1.55 \pm 0.13\ (1.46 \pm 0.04)$
L1551-IRS5	...	...	$1.88 \pm 0.05\ (1.51 \pm 0.02)$
TMC 1	...	$3.19 \pm 0.70\ (2.44 \pm 0.21)$	$2.04 \pm 0.08\ (1.39 \pm 0.19)$
BHR71	...	$4.95 \pm 0.20\ (3.75 \pm 0.03)$	$2.02 \pm 0.09\ (2.30 \pm 0.06)$
GSS30-IRS1	$1.23 \pm 0.08\ (2.26 \pm 0.21)$	$2.36 \pm 0.16\ (5.60 \pm 0.15)$	$3.03 \pm 0.07\ (2.14 \pm 0.02)$
VLA1623	...	$3.36 \pm 0.24\ (4.70 \pm 0.04)$	$5.67 \pm 0.38\ (2.78 \pm 0.17)$
WL12	...	...	$1.17 \pm 0.10\ (1.60 \pm 0.11)$
Elias 29	$1.40 \pm 0.12\ (1.84 \pm 0.25)$	$2.00 \pm 0.09\ (4.40 \pm 0.06)$	$1.69 \pm 0.04\ (1.79 \pm 0.02)$
IRS 63	...	...	$1.35 \pm 0.23\ (1.75 \pm 0.08)$
B335	...	$2.02 \pm 0.18\ (2.46 \pm 0.04)$	$2.02 \pm 0.16\ (1.81 \pm 0.11)$
L1157	$4.23 \pm 1.60\ (1.61 \pm 0.11)$	$2.36 \pm 0.09\ (2.05 \pm 0.03)$	$1.89 \pm 0.09\ (1.62 \pm 0.11)$

Notes. Comparison of spatial extent for lines and local continuum for the 15 well-centered sources with no known source confusion at the resolution of *Herschel*. Each entry is a pair of values: the ratio of the line flux in the central 3×3 spaxels over the line flux in the central spaxel, and in parentheses the ratio of the average continuum flux density in the central 3×3 spaxels over the continuum flux in the central spaxel, in a selected range of wavelengths near the line. Formal errors are provided for each line ratio, but systematic calibration uncertainties and spaxel-to-spaxel variation are not included.

L1527, and IRS 44), lack clear evidence for multiple, spatially separated emission peaks at the resolution of *Herschel* (we exclude Serpens-SMM3/4, RCrA-IRS5A/7B/7C, L1448-MM, and IRS 46), and have sufficient flux density to be detectable in continuum at all PACS wavelengths (we exclude L1455-IRS3, L1014, and IRAM 04191). DK Cha is clearly extended despite the mispointing. We restrict further analysis of the extent of line emission to the 15 sources with sufficient S/N, and to lines with clear detections in the 3×3 spectrum.

The PACS PSF is larger at longer wavelengths. Thus a source must be more extended to exceed the PSF at longer wavelengths and appear extended in our data. The ratio of the continuum flux density in the full 3×3 spaxel array to the emission from the central spaxel averages 1.83 ± 0.40 (median 1.79) at 63 μm, the average being higher by a factor of 1.28 than the PSF correction factor of 1.43. At 163 μm the ratio averages 3.09 ± 1.06 (median 2.55), with the average a factor of 1.51 higher than the PSF correction factor of 2.04. On average (and median) our sources are marginally extended, and more extended at the longer wavelengths. However, the lower median values compared with the mean values indicate that the extended emission is dominated by a few sources. In Tables 6 and 7, we only include formal errors in the local continuum rms; the overall calibration uncertainties may be much higher, including photometric calibration and
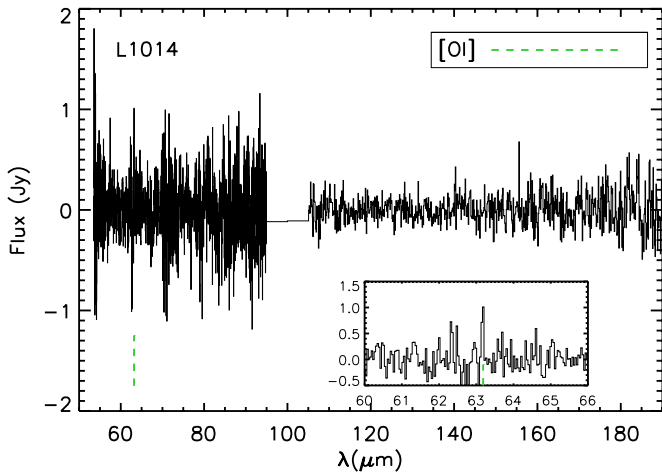
Figure 11. Continuum-subtracted spectrum of L1014, representative of the "cool" subset. The only detected line is [O I] 63.18 μm. Inset: zoom-in on the detection of [O I].

(A color version of this figure is available in the online journal.)

spaxel-to-spaxel variation. If we assume the uncertainty in the 3 × 3 and the central spaxel continuum is dominated by the photometric uncertainty (~20%), then adding this to the

ratio in quadrature, we would expect the ratio to be uncertain by ~28%. The continuum ratios in IRAS03245, IRAS03301, B1-a, BHR71, GSS30, VLA1623, and Elias 29 significantly exceed the PSF correction (by more than 28%), at most sampled wavelengths with sufficient S/N. In contrast, B1-c, L1489, L1551-IRS5, TMC1, WL12, IRS63, B335, and L1157 are consistent with a point source at most wavelengths (within the DIGIT sample, we are characterizing the compact core; notably L1157 contains an extended outflow on arcmin scales; Nisini et al. 2010). There are no objects that show a ratio significantly smaller than that of a point source.

There is no obvious distinction between the sources in these two groups (e.g., L_{bol}, T_{bol}, class/stage, or source distance). This measure will be a bit misleading as our method characterizes an extended source with an equally strong central peak as "pointlike;" PACS imaging suggests this may be the case for B335 in particular (A. Stutz 2012, private communication; Launhardt et al. 2013). Additionally, for a given source, there can be a trend with wavelength. WL12 is a bit of an outlier in that it shows greatly extended continuum at λ > 150 μm but is otherwise pointlike. The trend to larger sizes, relative to a point source, can also be seen in Figure 15 for GSS30-IRS1, where a trend toward displacement of the emission centroid toward the northeast with increasing wavelength can be seen. *H*-band Very
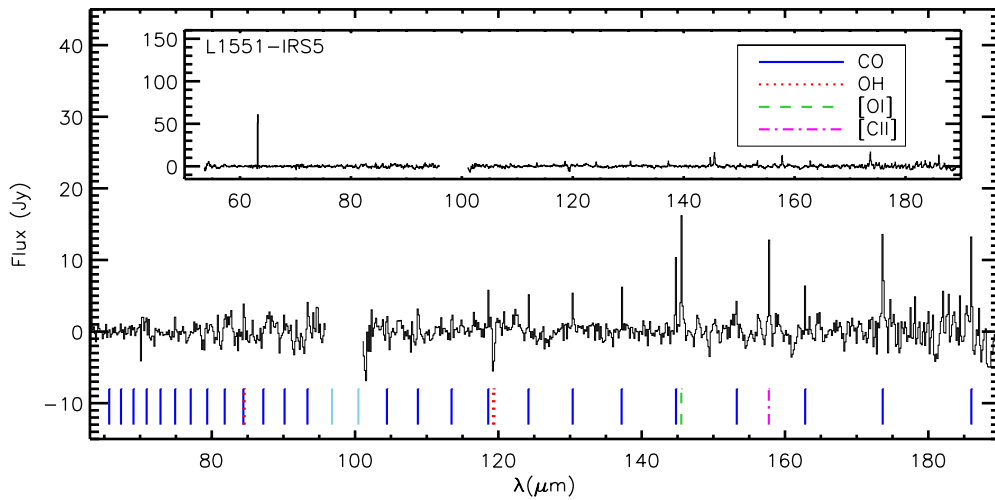
Figure 12. Continuum-subtracted spectrum of L1551-IRS5, a representative of the "warm" subset of the DIGIT embedded sources sample. The spectrum is rebinned to lower resolution at longer wavelengths to clarify line peaks. Inset: a zoomed-out image revealing the contrast between the strength of the [O I] 63.2 μm line and the remaining spectral lines.

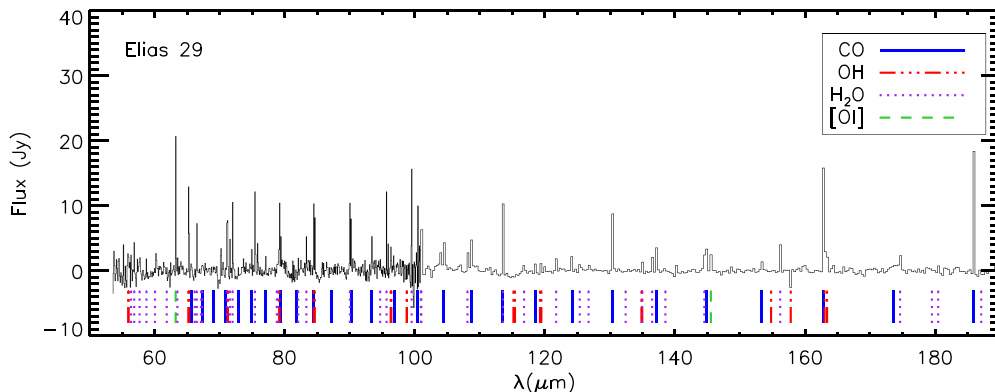(A color version of this figure is available in the online journal.)

Figure 13. Continuum-subtracted spectrum of Elias 29, a representative of the "hot" subset and the most line-rich spectrum in the DIGIT sample. The spectrum is rebinned to lower resolution at longer wavelengths to clarify line peaks.

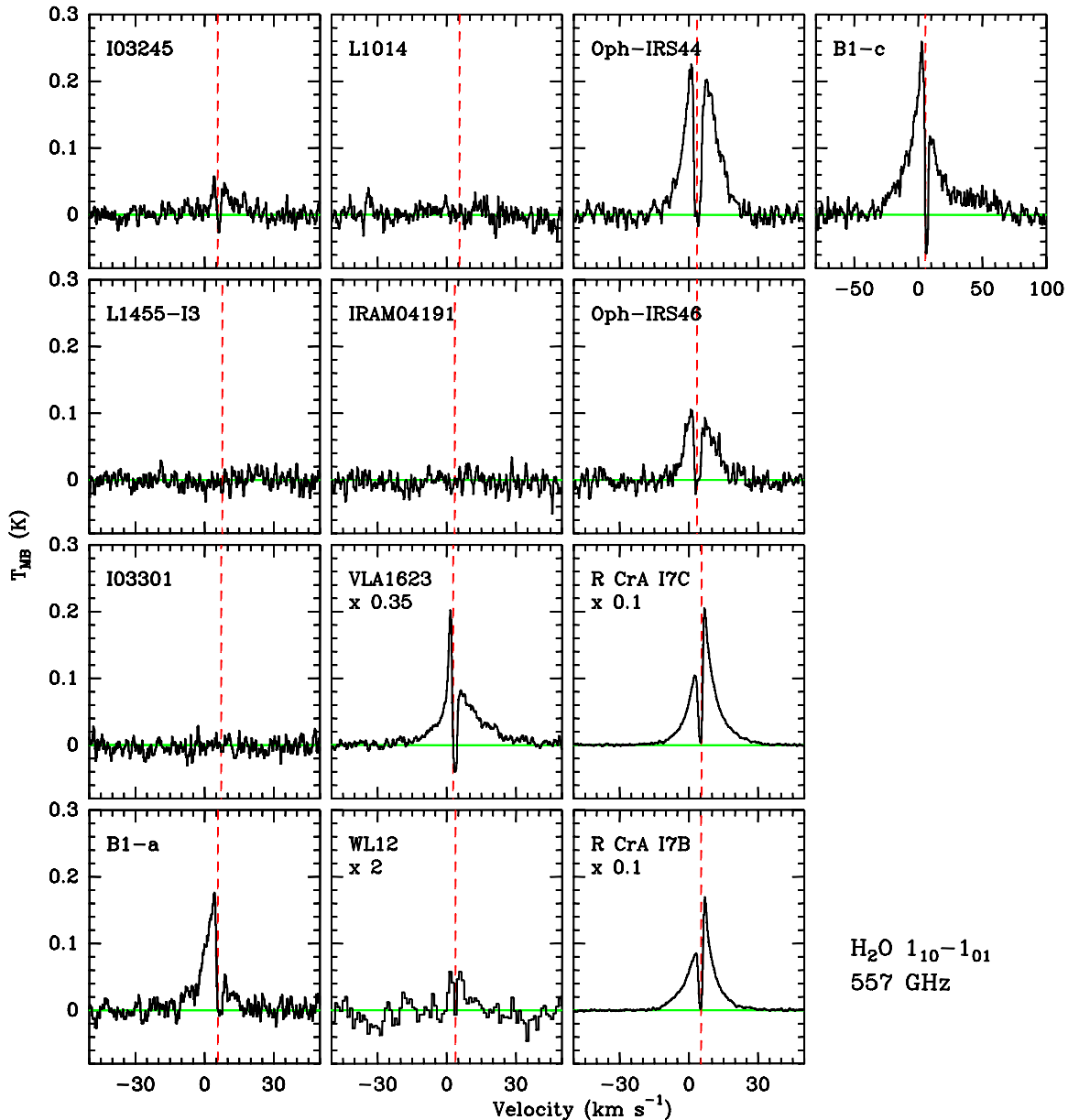(A color version of this figure is available in the online journal.)

18

Figure 14. HIFI observations of the 557 GHz H_2O line for the DIGIT sample. The source velocity is marked with a dashed red line, and the zero-point with a solid green line.

(A color version of this figure is available in the online journal.)

Large Telescope images (Chen et al. 2007) also show extended emission in this direction.

The extent of the line emission need not be coupled to continuum. Tables 6 and 7 also give the ratios for the characteristic lines. For the CO $J = 16 \rightarrow 15$ line, the ratio averages 2.38 ± 0.60 (median 2.24), a factor of 1.17 above the PSF correction factor of 2.04, smaller than the value for the adjacent continuum at 163 μm. In contrast, the ratio for the [O I] 63 μm line-flux averages 2.25 ± 1.15 (median 2.02), 1.57 times the PSF correction of 1.43. Thus the [O I] line is more extended, on average, than the adjacent continuum. The CO $J = 29 \rightarrow 28$ line ratio averages 1.56 (median 1.51, PSF correction: 1.45), and is thus essentially pointlike where detected. The H_2O 66.5 μm line ratio is measured in four sources, two of which appear to be extended (B1-a, L1157). There are a few that appear *less*

extended than the PSF; in each case the line is only faintly detected above the noise in the extended aperture, but is strongly peaked in the central spaxel—most notably the CO, but not the [O I], in L1551-IRS5. The [O I] partially tracks extended outflow emission around L1551-IRS5, while the CO is more compact. Again, in the ensemble, the line emission appears to be slightly extended, particularly in the [O I] line; this does not necessarily correlate with extended continuum emission.

In a minority of our sample we can discern significant spatial differences between [O I] and the molecular species. For example, GSS30-IRS1 (Figure 16) shows compact, well-centered emission for all the lines except [O I], which is extended and peaks toward the northeast, similar to but more strongly than the continuum at long wavelengths (Figure 15). Similarly, in B1-a, the [O I] emission peaks $\sim 5''$ east of center. The shift is
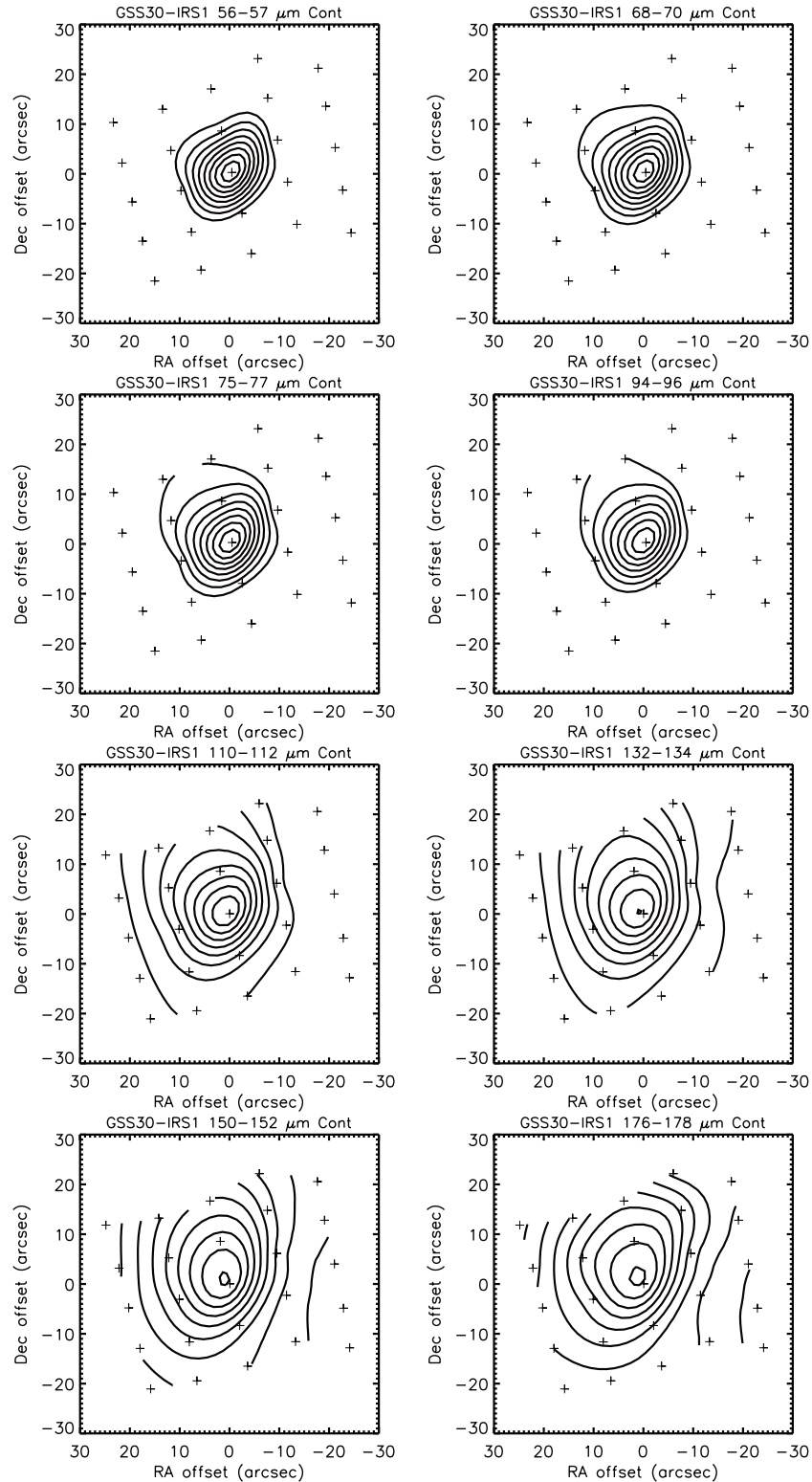
Figure 15. Maps of continuum bands in GSS30-IRS1. The "+" indicate the positions of the PACS spaxels. The contours are in increments of 10% of the central spaxel value, but cut off below the 3σ level. The bands are, in order (μm): 56–57, 68–70, 75–77, 94–96, 110–112, 132–134, 150–152, and 176–178.

particularly convincing as it appears in both [O I] lines in both GSS30 and B1-a.

Additional examples of spatially extended emission appear in Appendix B. The resolution of multiple sources in the L1448-MM region is apparent: the continuum at all wavelengths is relatively compact and centered, but the [O I] emission tracks the

chain of sources to the south. Additionally, the lower excitation lines of CO and H_2O are centered further south, while the higher excitation lines (including both OH lines) track the continuum. IRAS03245 shows an extended wing of [O I], CO, and H_2O to the southwest; H_2O is nearly absent from the source position. B1-a shows a southwest extension in long wavelength
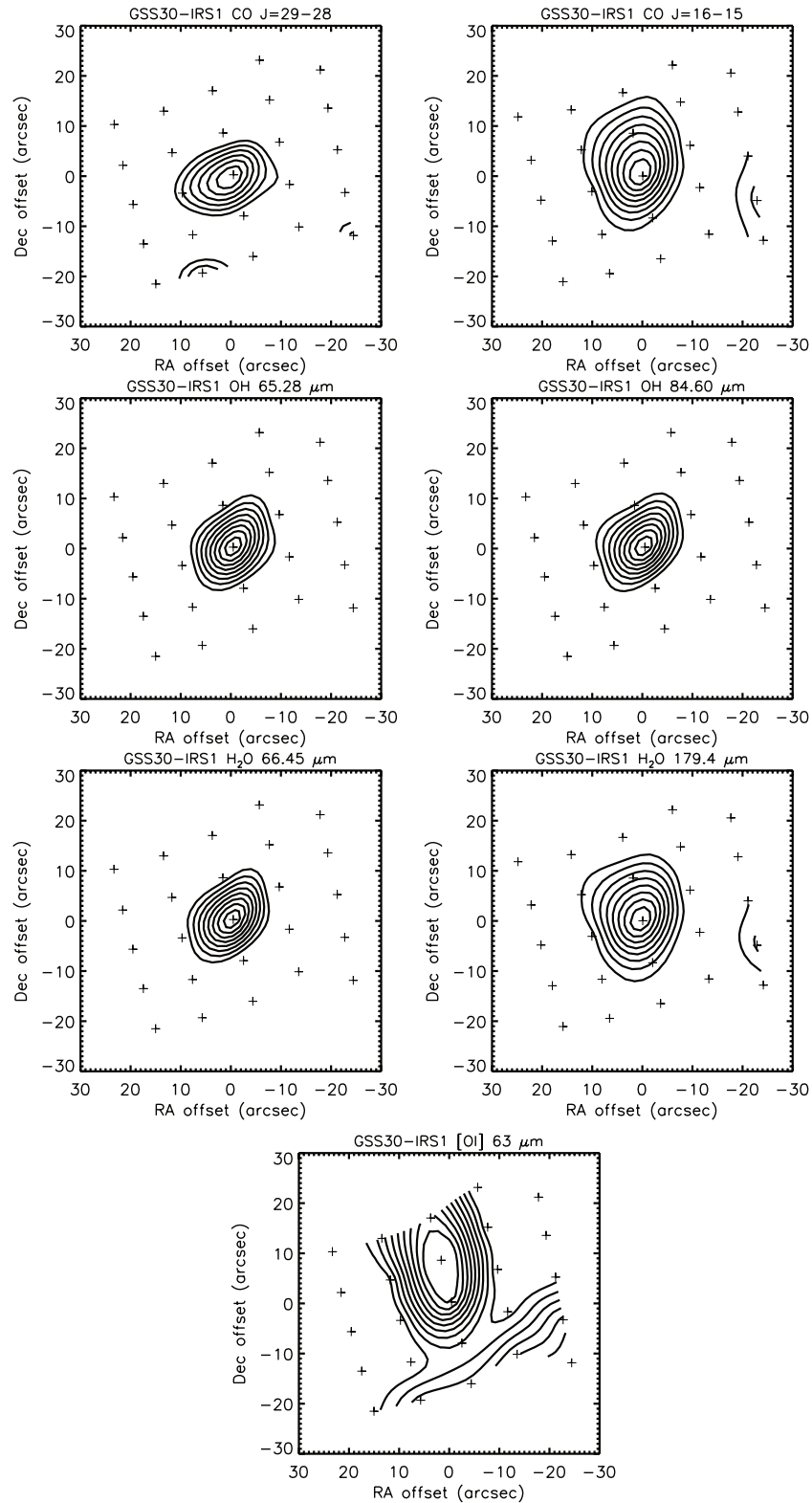
Figure 16. Contour maps of archetypal lines in GSS30-IRS1. The "+" indicate the positions of the PACS spaxels; the lines are identified above. The contours are in increments of 10% of the central spaxel value, but cut off below 3σ. The left column shows contours for the high energy line tracers in the sample, while the right column shows contours for the low energy line tracers.

continuum that is not replicated in the line emission. B1-c shows extended bipolar emission in CO along the southeast–northwest axis, but no accompanying [O I]. VLA1623 shows [O I] in a strong east-west band (without any particular peak on the source) and extended long-wavelength continuum emission to the northeast.

In summary, the majority of the DIGIT sources show only limited variation in spatial extent within the PACS footprint, in line or continuum. This does not necessarily hold across all samples, or those with denser spatial sampling; Karska et al. (2013) find that most of their extended sources are the Class 0 objects; we do not see a particular trend in the DIGIT sample.

4.3.3. Line Fluxes and Luminosities

The measured fluxes and uncertainties for the eight characteristic lines identified in Section 4.3.1 are shown in Table 5, including corrections for extended emission. We do not include fluxes for sources in confused regions; refer to Dionatos et al. (2013; Serpens SMM 3/4) and J. E. Lindberg et al. (2013, in preparation; RCrA-IRS5A, 7B, and 7C) for detailed studies of these sources. We include in our statistics the composite L1448-MM spectrum. The uncertainties are calculated as the residual from a Gaussian plus first-order baseline fit to line-free sections of the local continuum for each line. For undetected lines we provide 3σ upper limits derived from local continuum, using a linewidth equal to the average over the detected lines near that wavelength in the sample. The average linewidths are: $0.0454\,\mu m$ (CO $J = 29 \rightarrow 28$ and OH $84.60\,\mu m$), $0.0468\,\mu m$ (OH $65.28\,\mu m$ and H_2O $66.45\,\mu m$), and $0.1232\,\mu m$ (CO $J = 16 \rightarrow 15$ and H_2O $179\,\mu m$). A full inventory of all lines across the sample will appear in a followup paper following a reprocessing with post-mission calibration.

Figure 17 shows histograms of these line fluxes. In each we show a typical value for the rms noise (dashed vertical lines). The distributions of line fluxes differ among the lines. The [O I] $63.2\,\mu m$, CO $J = 16 \rightarrow 15$, and perhaps the H_2O $179.5\,\mu m$ line fluxes appear to peak above the detection limit, while the CO $J = 29 \rightarrow 28$, and H_2O $66.5\,\mu m$ line fluxes peak near the detection limit, suggesting that deeper integrations would see lines in more sources (as confirmed by Karska et al. 2013). In all cases, the line fluxes spread over 1–2 orders of magnitude above the detection limit (Figure 18).

4.3.4. Non-detection of ^{13}CO in PACS

The highest line fluxes are found in the lowest J ^{12}CO lines detectable with PACS; the highest of the 15 well-centered sources is BHR71, with CO $J = 15 \rightarrow 14$ ($173.63\,\mu m$) $F_{line} = 7.9 \times 10^{-16}$ W m^{-2}. The laboratory wavelength of ^{13}CO $J = 15 \rightarrow 14$ is at $181.6\,\mu m$. Using the local continuum we set a 3σ upper limit to the flux of the ^{13}CO line at 1.0×10^{-16} W m^{-2}, a factor of ~ 7.8 below the ^{12}CO flux. Assuming an interstellar abundance ratio of 70, and an equal emitting area, we estimate an upper limit to the optical depth τ of ~ 9.0. This upper limit is improved if we consider line "stacking." If we assume the same warm T_{rot} component for the ^{13}CO and ^{12}CO gas, we can add the statistical weight of all non-detections of ^{13}CO in the PACS range, in comparison to the detections of ^{12}CO—excluding cases in which either line falls within the trimmed regions. For this dataset (22 lines in total), using a weight inversely proportional to the rms noise in the local continuum for each line (Fedele et al. 2012), we derive an upper limit on the ^{12}CO/^{13}CO ratio of 13.7, or an upper limit to τ of 5.1. This is consistent with the models of Visser et al. (2012), where the ^{12}CO emission probed with PACS is optically thin.

5. ROTATIONAL DIAGRAMS ACROSS THE SAMPLE

5.1. Rotational Diagrams for H_2O and OH

The simplest way to analyze multiple molecular rotational transitions is the rotational diagram, introduced by Linke et al. (1979). A detailed description can be found in, e.g., Goldsmith & Langer (1999), and we give a full description of our method in Appendix C, with a brief overview here of the assumptions required for each step. We use the subscript J as shorthand for the full state descriptor for the more complex species characterized by multiple quantum numbers. If the emission lines are optically thin, the number of molecules per degenerate sub-level in the upper state of the transition, $\mathcal{N}_J/g_J$, is proportional to the line flux. If the resulting plot of the logarithm of $\mathcal{N}_J/g_J$ versus excitation energy of the upper state (in units of K) can be fit by a straight line, one can assign a rotational temperature (T_{rot}). Finally, if all the levels are in LTE, one can set $T_{rot} = T_K$, but this last step is not necessarily implied by a good fit to a single T_{rot}. In LTE, the total number of molecules at that value of T_K (denoted by $\mathcal{N}$) can be calculated by the y-intercept of the fit and the value of the partition function at T_K. If the levels are not in LTE, one can still compute $\mathcal{N}$, but the partition function may be incorrect. The values of $\mathcal{N}$ discussed below carry this caveat.

A characteristic rotational diagram for each detected molecular species (H_2O, OH, CO) in the source Elias 29 is shown in Figure 19. While a line can be fitted to the H_2O and OH diagrams, the scatter is much larger than the intrinsic uncertainties; we include line-flux uncertainties in our rotational diagram fits. This scatter is probably related to the existence of sub-thermal excitation in some lines, along with optical depth effects (see, e.g., Herczeg et al. 2012). There are 18 sources with enough detected H_2O lines to fit a single temperature component. The fits for T_{rot} for H_2O range from 76 to 379 K, with $\langle T_{rot} \rangle = 194 \pm 85$ K, and ranging from 80 to 520 K, with a mean of 183 ± 117 K, for OH. Accurate measurement of the OH line fluxes is hampered by line-blending as most of the transitions are only marginally resolved by *Herschel*. The OH excitation itself is complicated by radiative (IR) pumping via the cross-ladder transitions, and sub-thermal excitation (Wampfler et al. 2013; Lee et al. 2013). Additionally, B1-c appears to have $\mathcal{N}(H_2O)$ six times greater than the next highest in the sample; B1-c is the only source without a detectable [O I] line, and one of only two sources showing the OH $119\,\mu m$ doublet in absorption. This is consistent with its extremely strong 557 GHz H_2O emission. Since both OH and H_2O molecules require more complex analysis beyond the scope of this paper, we restrict further discussion of rotation diagrams to CO.

5.2. Rotational Diagrams for CO

CO is the simplest case to analyze because the critical density, E_u, and detected frequency all increase monotonically as a function of upper state J. We present all CO rotational diagrams for the sources with detectable CO in Figures 19 and 20. The CO rotational diagrams generally show a positive curvature, for those sources with sufficient detected lines and low relative scatter; this may be indicative of a smooth continuum of excitation temperatures (see also Neufeld 2012; Manoj et al. 2013). A simpler model presumes that the CO at certain ranges of upper state J is dominated by at most a pair of temperatures. We assume that the CO $J = 23 \rightarrow 22$ line is a blend with H_2O, and the CO $J = 31 \rightarrow 30$ line is a blend with OH, and ignore both in our fits. For statistical analyses of CO, we chose a single breakpoint, at $E_u = 1800$ K (as in Manoj et al. 2013) and fitted separate power laws to transitions with E_u below ("warm;" $J < 25$) and above ("hot;" $J > 25$) the breakpoint. Fits are provided in Table 8 for sources with sufficient data. We fitted two temperatures only for sources with at least four detected CO lines with E_u above the breakpoint, as we found the fits to be unstable with fewer lines. For sources with fewer CO lines, we fit only a single component, to the lines below 1800 K. There are 22 sources with sufficient CO lines to fit a warm component, 10 of which include a hot component in
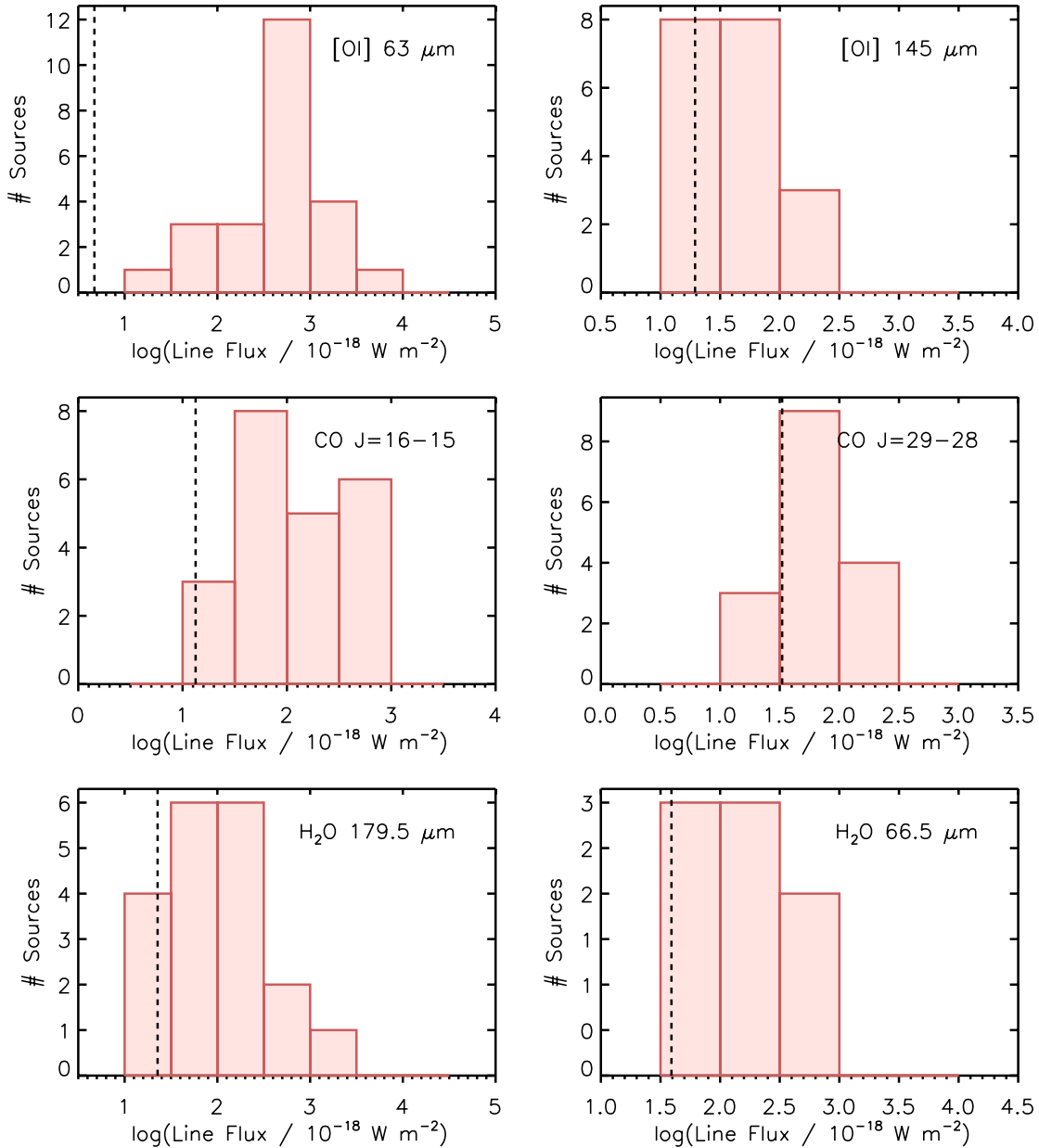
Figure 17. Histograms of line fluxes for characteristic lines. The dashed line represents the 1σ uncertainty in line flux for BHR71, one of the brighter sources in the sample, and can be taken as a conservative 1σ noise. The number of sources with upper limits is 25—the total number plotted—for each histogram (i.e., plots do not include the five confused sources in our sample).

(A color version of this figure is available in the online journal.)

addition; only six of those with hot components are statistically well-constrained (i.e., are fit with $\mathcal{N}(\text{hot})$ and $T_{\text{rot}}(\text{hot})$ greater than their derived uncertainties). If the lower excitation lines become optically thick, the state populations derived from the optically thin approximation would exhibit curvature and diverge from the fitted line. If the higher excitation lines are sub-thermally populated, the derived state populations may fall below the fitted line (Goldsmith & Langer 1999, Figure 6). The direct correspondence between E_{u} and the wavelength of the transition simplifies the analysis, in the case of CO; neither of these effects is seen in CO rotation diagrams for this sample. It should be noted that if *all* lines are sub-thermally excited (for very low densities), the curvature becomes positive and the state

populations may fall above the fitted line (Goldsmith & Langer 1999; Neufeld 2012).

5.2.1. Statistics and Trends Across the Sample

We consider the fits to rotation diagrams across the sample. In summary, while we fit both warm and hot components to the CO diagrams, we never observe the hot component in absence of the warm, and both components scale in proportion to the bolometric luminosity of the system. Figure 21 shows the distribution of T_{rot} for the warm and hot components of CO, along with the distributions of $\mathcal{N}$ for each component. The values of $T_{\text{rot}}(\text{warm})$ range from 200 to 589 K, with $\langle T_{\text{rot}} \rangle = 354 \pm 92$ K. Lower T_{rot} would be difficult to distinguish with
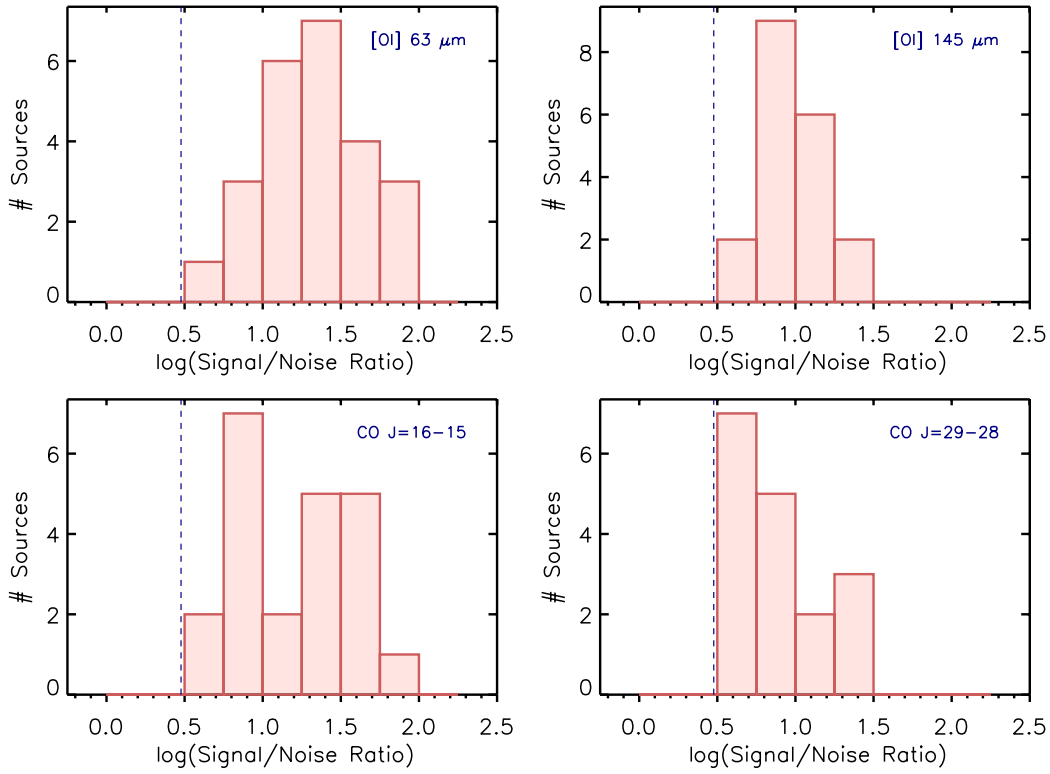
Figure 18. Histograms of the S/N ratio for characteristic lines. The blue vertical dashed line indicates a S/N of 3. We are complete in [O I] 63 μm and CO $J = 16 \rightarrow 15$, but less so in [O I] 145 μm and CO $J = 29 \rightarrow 28$.

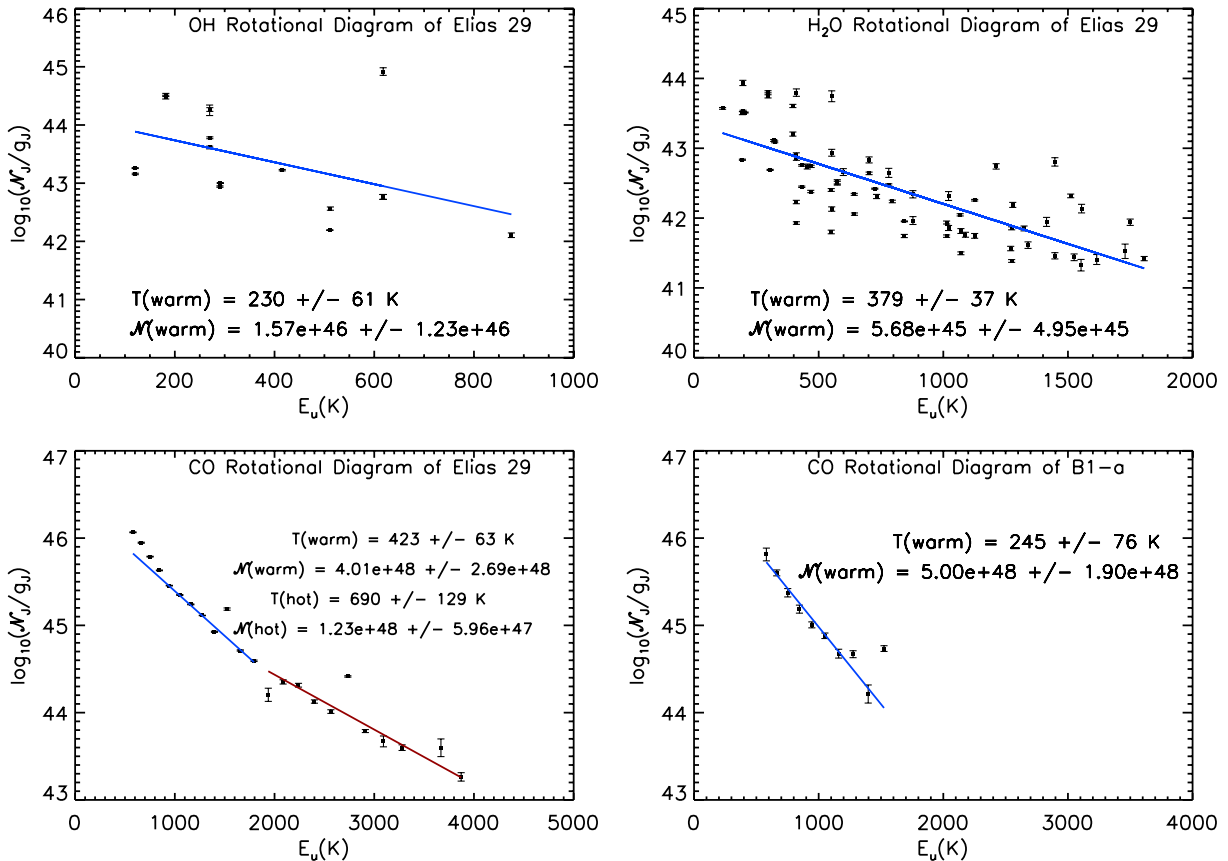(A color version of this figure is available in the online journal.)

Figure 19. Rotational diagrams for OH (upper left), H$_2$O (upper right), and CO (lower left) for Elias 29, showing the results of typical fits. We also show the rotational diagram for a source with only a detected warm component, B1-a (lower right). In all CO rotational diagram fits, we ignore the CO $J = 23 \rightarrow 22$ ($E_u = 1524$ K) and CO $J = 31 \rightarrow 30$ ($E_u = 2735$ K) datapoints, which are blended with H$_2$O and OH respectively.

(A color version of this figure is available in the online journal.)

24
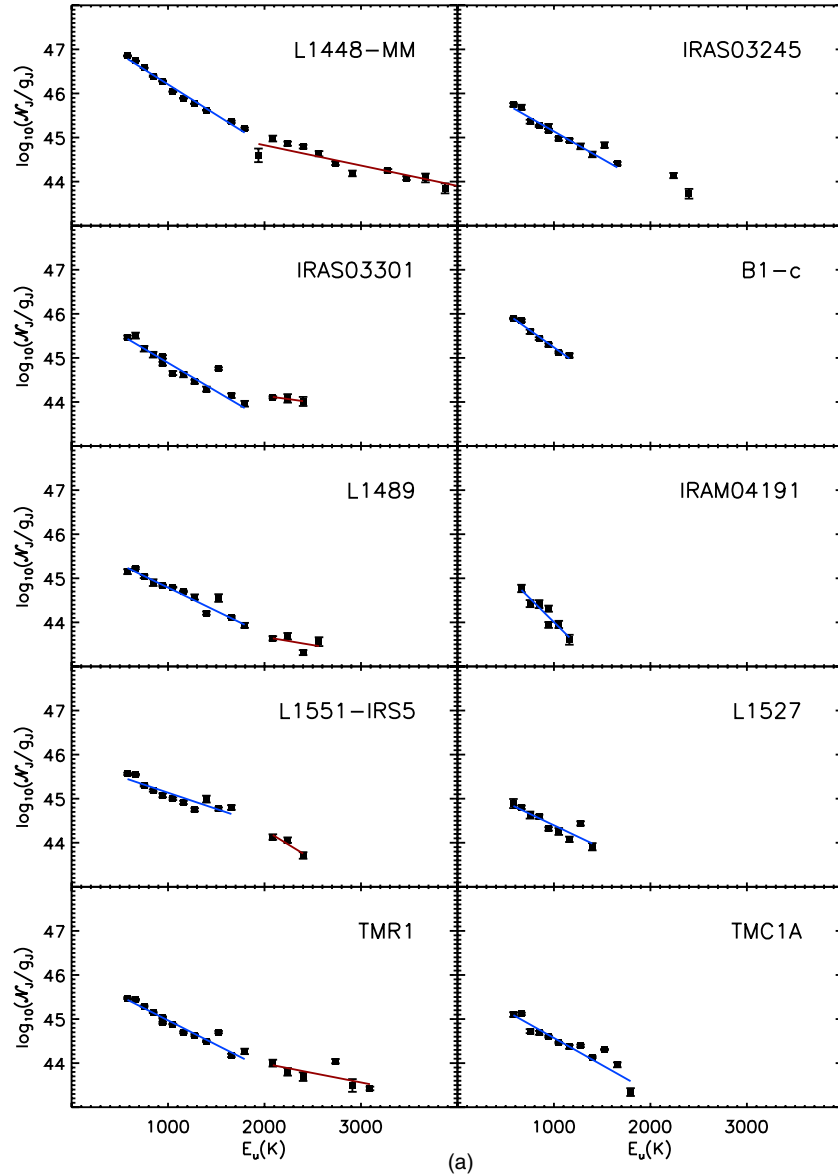
Figure 20. CO rotational diagrams for the full sample.
(A color version of this figure is available in the online journal.)

the values of E_u for the lines we observe. Further exploration of the lower T_{rot} region awaits data on lower excitation transitions. The distribution of hot components has $\langle T_{rot}\rangle = 932 \pm 217$ K for the six sources with statistically significant fits, similar temperatures to those found by fitting the noise in Elias 29, but with much higher $\mathcal{N}$. Typical errors for T_{rot}(warm) are of order 100 K, but the hot component is much less constrained. The sources with T_{rot}(hot) $\lesssim$ 1000 K are reasonably well constrained ($\pm$300 K), but all sources with T_{rot}(hot) > 1030 K are derived from highly uncertain fits ($\pm$ 1000 K or greater) and are consistent with temperatures $\lesssim$1000 K. Thus there is little evidence of a distinct component above 1000 K. For the 12 sources with a warm component but with no detected hot component, the T_{rot}(warm) values average 339 $\pm$ 98 K, very similar to the 373 $\pm$ 39 K average for the 10 sources with both components, although with greater volatility due to increased uncertainties. All CO lines are at least 3σ detections.

Of the 10 sources with fitted hot components, the ratio of molecules in the warm component is 5–10 times that of the hot component, but in two cases (B335 and L1448-MM), we find a relatively small hot component. B335 is a likely outlier because we detect only six CO lines in the hot component, leading to very uncertain fits. This is not the case for L1448-MM, which has one of the richest CO spectra in the sample; this may reflect a larger emitting region of warm gas compared with the hot gas, consistent with the source line map shown in Appendix B of this work. L1551-IRS5 has a higher warm T_{rot}(CO) than the rest of the sample, at 589 $\pm$ 335 K; it also has a relatively low line-to-continuum ratio and shows little emission from molecules other than CO.

Across the sample, the total number of CO molecules in warm and hot components, $\mathcal{N}$ (excluding the R CrA and Serpens sources and those sources with no detectable CO component) ranges from 0.02 to 4.56 $\times$ 10^{49} molecules, with $\langle \mathcal{N}\rangle = (0.70 \pm 1.12) \times 10^{49}$.
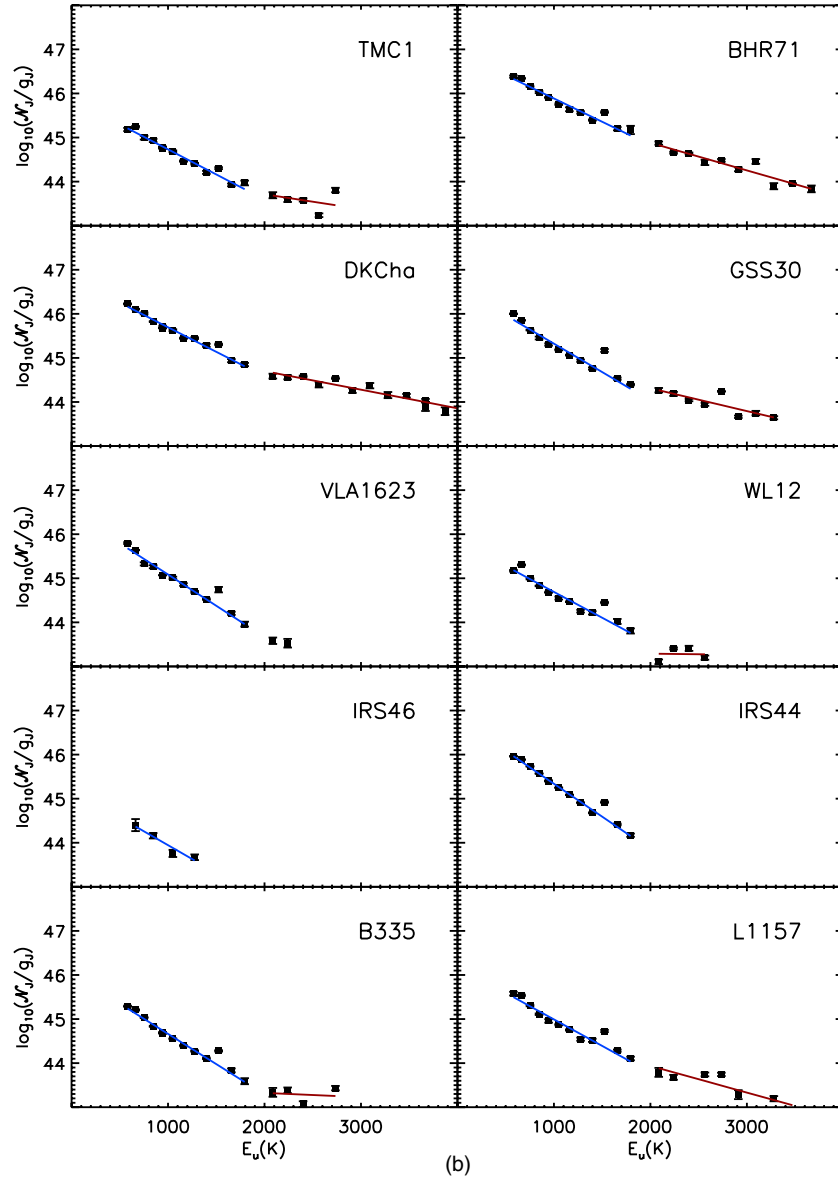
Figure 20. (Continued)

5.2.2. Caveats to the Two-temperature Fits

Fitting two components with a breakpoint to CO rotation diagrams is a common approach (e.g., van Kempen et al. 2010a; Manoj et al. 2013), but the results may be affected by relative flux calibration uncertainties, the selection of the breakpoint, or uncertainties in the fluxes of fainter lines. A scaling factor adjusting the absolute flux of all lines will increase the derived $\mathcal{N}$ for a given $T_{\rm rot}$, while a relative scaling factor between modules may affect the derived temperatures. The $E_{\rm u} = 1800$ K breakpoint corresponds to the transition between the second and first orders, thereby avoiding effects of misalignment of orders on the derived values of a single component, although the ratio of the $\mathcal{N}$ of the two components would be affected. However the analysis is not qualitatively affected by moving the breakpoint by $\leqslant 2$ transitions in either direction. Shifting the breakpoint to a lower excitation will cause both temperatures to decrease, and both $\mathcal{N}$ values to increase (Table 9).

As noted above, the values of $T_{\rm rot}$ need not correspond to kinetic temperatures. Moreover, the interpretation of rotation diagrams in terms of two distinct regimes of $T_{\rm rot}$ is not unique. The broken power law can also be fitted by a polynomial with terms up to second order. The two components can also be described by a positive second order term (curvature upward to lower J). More than two temperature components or a power-law distribution of temperatures will produce a distribution with a positive second derivative (e.g., Goldsmith & Langer 1999; Neufeld 2012; Manoj et al. 2013; J. K. Jørgensen et al. 2013, in preparation). Heating and cooling across a shock produces a distribution of temperatures (Flower & Pineau Des Forêts 2010; Dionatos et al. 2013). Figure 13 in Karska et al. (2013) contains the CO $T_{\rm rot}$ values from the full shock models from Kaufman & Neufeld (1996).

Even more interesting effects can be seen if the lines are not in LTE. In particular, Neufeld (2012) has shown that, at quite low ($n < 10^5$ cm^{-3}) densities, but very high $T_{\rm K}$ ($\sim$2000 K), a positive curvature can appear in the rotation diagram because of the behavior of the collision rates and the excitation balance. Figure 22 shows the fraction of CO molecules in each state J, normalized to $\mathcal{N}$, for B335, overplotted on the models from
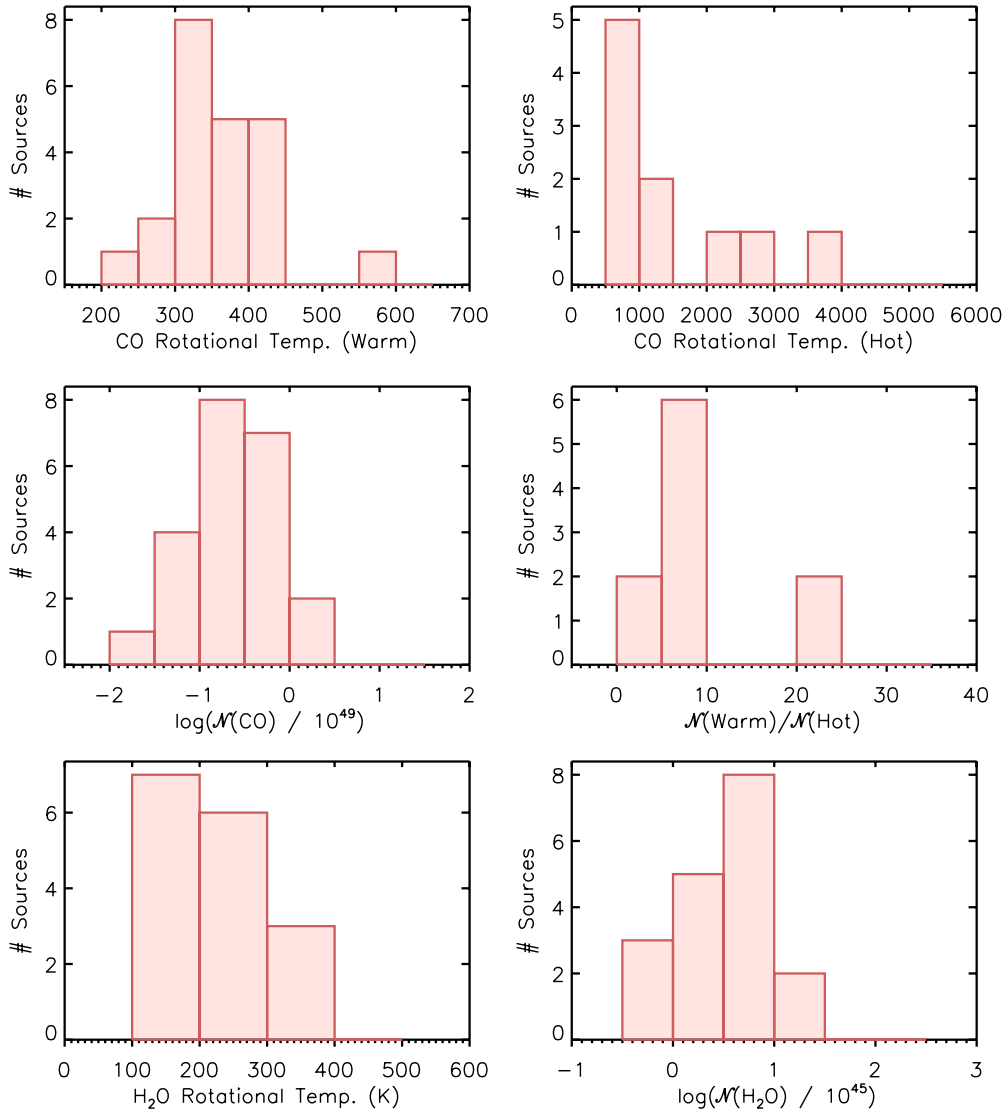
Figure 21. Histograms of $\mathcal{N}$ and $T_{\rm rot}$ for CO and H_2O. Top: CO rotational temperatures for the warm and hot components. Middle: total number of CO molecules for the warm component, and ratio of molecules in the warm/hot populations. Bottom: temperature and $\mathcal{N}$ for H_2O.

(A color version of this figure is available in the online journal.)

Figure 5 from Neufeld ([2012](#)). The best fit density appears to vary from 10^5 to 10^6 cm^{-3} over the full range of J, suggesting that the 1000 K (isothermal) optically thin model will not match the CO line fluxes for $J \gtrsim 23$. However, if we increase T_K to 3000 K, a good fit to all the CO lines in B335 can be obtained for a surprisingly low density, $n = 10^4$ cm^{-3} (Figure [22](#)). Deciding whether such an extreme solution is physically reasonable is examined in other papers that study individual sources in this sample.

6. CORRELATIONS

We consider here a few correlations across the sample. A Pearson's $r > 0.63$ is considered significant at the 3σ level, for our sample of $N = 24$ (except where noted below); we use this metric for straightforward comparison to Karska et al. ([2013](#)). We use formal errors for each line, calculated from the residual rms after fitting a Gaussian and first-order polynomial to the local continuum, added in quadrature to an overall calibration

uncertainty floor of 10%. As an aside, we also considered all of the above correlations using the $L_{\rm submm}$ classification for Class 0/I sources; qualitatively the results were unchanged. In general, we found that $T_{\rm rot}$ for each species was generally uncorrelated with any other properties, while $\mathcal{N}$ and $L_{\rm bol}$ tracked each other fairly well (but with significant scatter in the cases of OH and H_2O).

A tight correlation exists between the $\mathcal{N}_{\rm CO}$ and CO $J = 16 \rightarrow 15$ line luminosity ($r = 0.88$), indicating that a single line of CO will trace the warm component well (Figure [23](#)). The warm component is also a strong predictor for $\mathcal{N}_{\rm CO}$(hot), as the CO $J = 16 \rightarrow 15$ and CO $J = 29 \rightarrow 28$ line luminosities correlate very well ($r = 0.93$). The other molecular species correlate with the warm CO. $\mathcal{N}_{\rm H_2O}$ correlates with $\mathcal{N}_{\rm CO}$ ($r = 0.86$), suggesting a similar abundance ratio between CO and H_2O in all sources, although there is more scatter in the Class 0 sources. OH 84.60 μm ($r = 0.72$, $N = 20$) correlates as well. In the case of OH 65.28 μm ($r = 0.53$, $N = 12$), we do not show a statistically significant correlation; this is the only case where
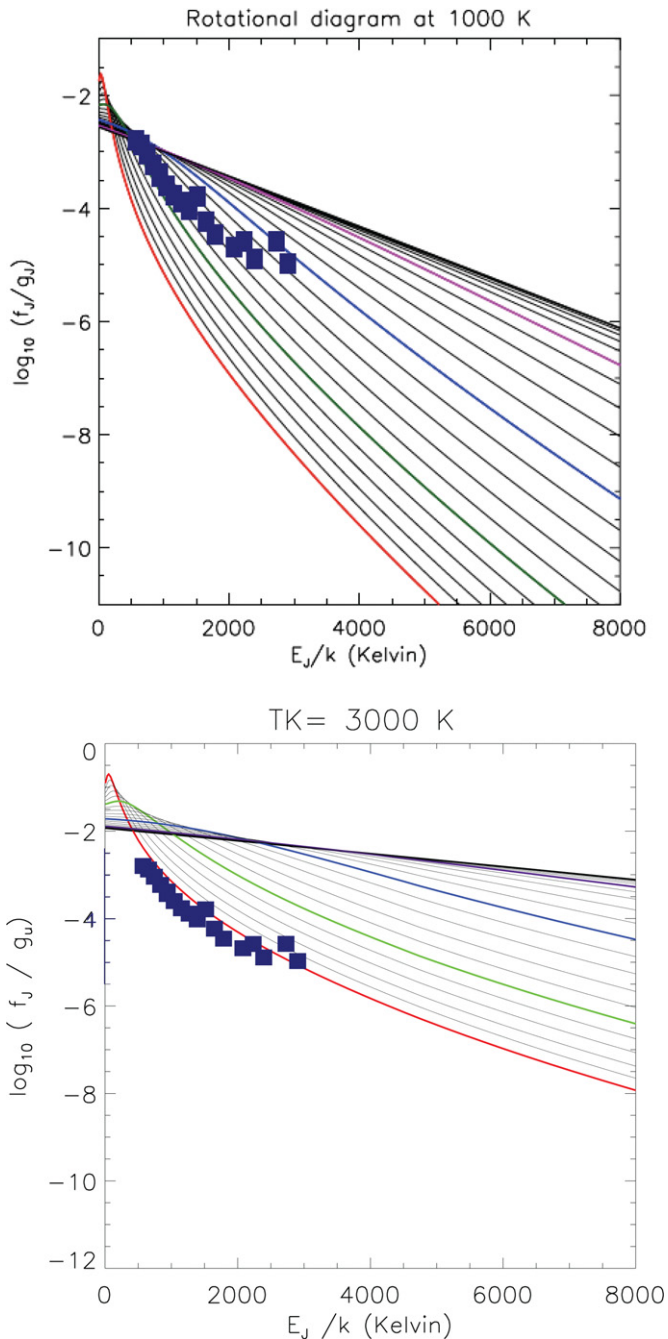
Figure 22. Top: comparison of the CO state populations (blue squares) in B335 overplotted on models for a 1000 K isothermal, optically thin emitting region, from Figure 5 in Neufeld (2012). We use the same axis labels for clarity; E_J is the energy of the upper state J. The solid lines are constant density; the purple line is the solution for $n = 10^7$ cm^{-3}, the blue line is for 10^6, the green line is for 10^5, and the red (lowest) line is for 10^4. Bottom: the same data compared to a 3000 K model.

(A color version of this figure is available in the online journal.)

Table 8
CO Rotational Temperatures and Total Number of Molecules

Source	T_{rot}(Warm) (K)	T_{rot}(Hot) (K)	$\mathcal{N}$(Warm) (10^{49})	$\mathcal{N}$(Hot) (10^{47})
L1448-MM	315 ± 78	942 ± 288	4.37 ± 2.18	19.0 ± 8.9
IRAS 03245	348 ± 117	...	0.31 ± 0.15	...
L1455-IRS3	...	...	...	...
IRAS 03301	336 ± 89	...	0.18 ± 0.10	...
B1-a	245 ± 76	...	0.50 ± 0.19	...
B1-c	277 ± 150	...	0.64 ± 0.19	...
L1489	409 ± 133	1177 ± 3846	0.11 ± 0.06	1.09 ± 0.04
IRAM 04191	200 ± 96	...	0.11 ± 0.19	...
L1551-IRS5	589 ± 335	...	0.16 ± 0.09	...
L1527	416 ± 219	...	0.04 ± 0.02	...
TMR1	392 ± 121	1016 ± 1163	0.17 ± 0.09	2.56 ± 0.42
TMC1A	351 ± 98	...	0.08 ± 0.04	...
TMC1	381 ± 114	1290 ± 979	0.10 ± 0.05	1.13 ± 0.44
BHR71	410 ± 133	693 ± 298	1.30 ± 0.70	33.9 ± 8.5
DK Cha	389 ± 119	1030 ± 471	0.91 ± 0.49	13.0 ± 5.0
GSS30	336 ± 89	838 ± 632	0.50 ± 0.25	6.74 ± 1.24
VLA1623	306 ± 74	...	0.35 ± 0.18	...
WL12	369 ± 108	...	0.10 ± 0.05	...
Elias29	423 ± 63	690 ± 129	0.401 ± 0.269	12.3 ± 6.0
IRS46	345 ± 260	...	0.02 ± 0.005	...
IRS44	291 ± 66	...	0.71 ± 0.36	...
IRS63	...	...	...	...
B335	316 ± 78	4513 ± 11497	0.124 ± 0.063	0.54 ± 0.20
L1157	360 ± 103	716 ± 410	0.20 ± 0.11	3.66 ± 0.69
L1014	...	...	...	...

Notes. Rotational diagram fits to the sample. Sources with > four CO lines of excitation energy >1800 K are fitted with two temperatures, "warm" and "hot," with a breakpoint at 1800 K. Three sources (IRS 63, L1014, and L1455-IRS3) show little or no detectable CO emission and cannot be analyzed with a rotational diagram. Of the remaining 27 sources, we fit "hot" components to 10 of them, of which 6 produce a statistically significant fit.

Table 9
Breakpoint in CO Rotational Diagrams

Breakpoint (K)	$\mathcal{N}$(Warm) $(\times 10^{49})$	$\mathcal{N}$(Hot) $(\times 10^{47})$	T_{rot}(Warm) (K)	T_{rot}(Hot) (K)
2300	1.22	35.8	433	684
2100	1.22	30.1	431	718
1900	1.30	33.9	410	693
1700	1.44	43.3	378	648
1600	1.59	45.6	352	639

Notes. The effect of shifting the breakpoint between the "warm" and "hot" temperature components in the CO rotational diagram for BHR71. The 1800 K breakpoint is equivalent to the 1900 K entry (there are no transitions between 1800 and 1900 K as we exclude the CO $J = 26 \rightarrow 25$ line in this work).

we see a striking split between Class 0 and I sources, but attribute this to small sample size. The total number of molecules shows no significant correlation with T_{rot} (Figure 24), either for CO ($r = -0.13$) or H$_2$O ($r = -0.37$), primarily due to the large uncertainty in T_{rot}.

We also consider the correlations with properties of the SED derived from ancillary data. The total number of molecules ($\mathcal{N}$) correlates with L_{bol} (Figure 25) for CO (warm component: $r = 0.61$, $N = 22$; hot: $r = 0.85$, $N = 10$) but not very well

for H$_2$O ($r = 0.67$, $N = 18$). The ratio of the hot to warm component is uncorrelated with L_{bol} ($r = 0.28$, $N = 7$), for those sources with robust hot components.

While the molecular emissions correlate with each other and with L_{bol} (as noted in Manoj et al. 2013), the excitation (characterized by T_{rot}) differs substantially among the molecules. Together with the lack of correlation with T_{rot}, these correlations suggest that the emission is driven by a process related to the luminosity of the source, but that the excitation (T_{rot}) is determined by the physics of the interaction, such as the properties of a shock front, and the much greater critical densities for H$_2$O and OH, compared with CO.
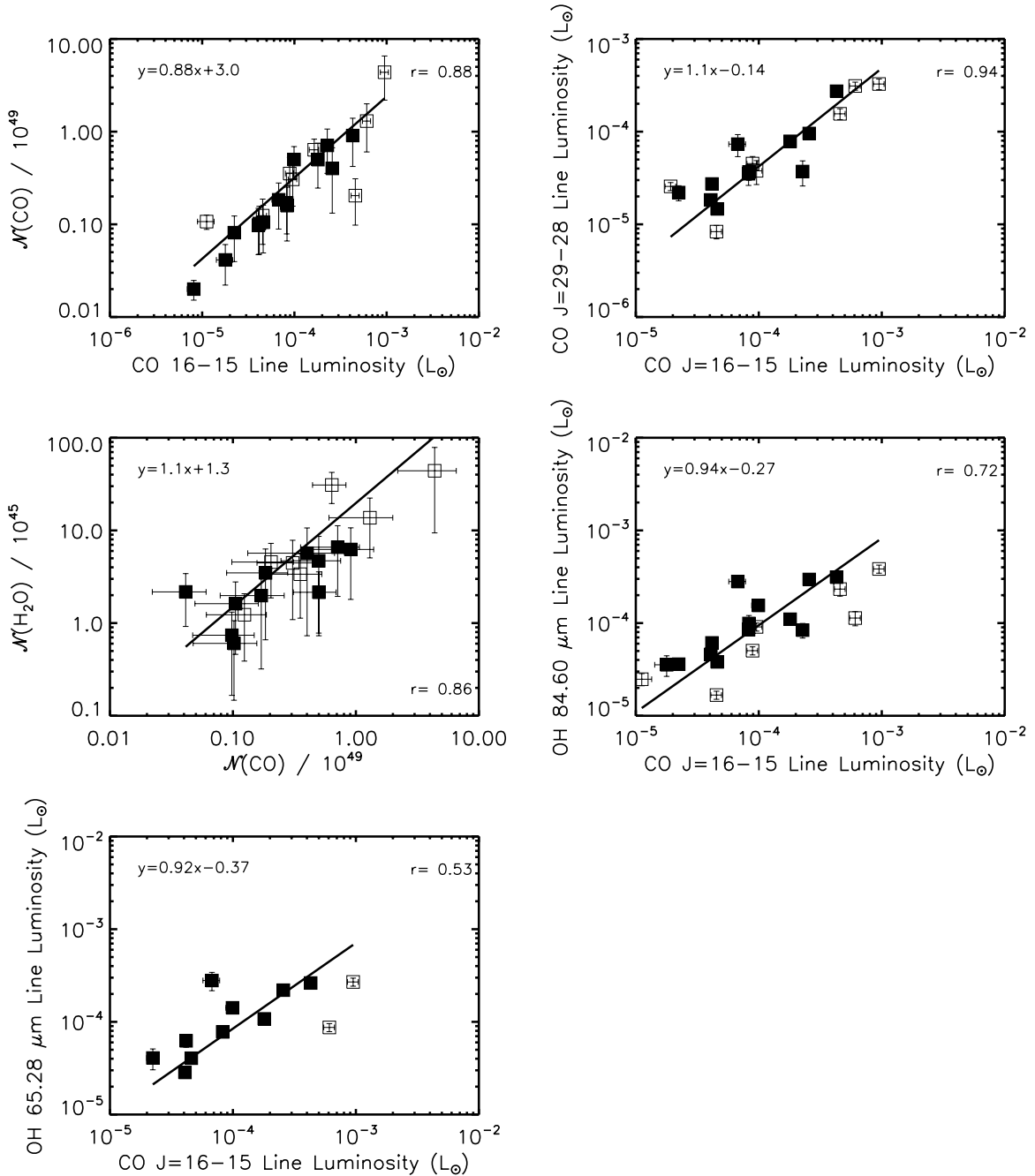
Figure 23. Top left: $\mathcal{N}_{CO}$ plotted vs. a single line of CO (the $J = 16 \rightarrow 15$). This line (and other nearby transitions) closely predict $\mathcal{N}_{CO}$. Top right: CO $J = 29 \rightarrow 28$ vs. CO $J = 16 \rightarrow 15$ line luminosity. Middle left: $\mathcal{N}_{CO}$ vs. $\mathcal{N}_{H_2O}$, showing a close correlation. Middle right: OH 84.60 μm vs. CO $J = 16 \rightarrow 15$ line luminosity. Bottom: OH 65.28 μm vs. CO $J = 16 \rightarrow 15$ line luminosity. In all panels, Class 0 sources (according to T_{bol}) are plotted as open symbols and Class I sources are plotted as filled symbols. Plotted values without error bars have errors less than the symbol size.

6.1. Comparison with the WISH and HOPS Samples

Karska et al. (2013) consider a larger sample from the WISH survey; here we compare results. On most statistical trends we find close agreement. We detect H_2O 179.5 μm in most sources, and find that about 50% of those also show more highly excited water.

We detect CO up to $\sim J = 40 \rightarrow 39$ in the brightest sources, although Karska et al. (2013) detect even higher-order transitions due to their increased sensitivity. We also noted the strong correlation between the detection of 179 μm H_2O and relatively

low-J CO lines as seen by them. We find a very similar warm temperature component in the rotational diagrams with perhaps a slightly higher T_{rot}(hot), but within the errors in agreement with the Karska et al. (2013) result. We have noted the lack of distinction between Class 0 and I sources in the DIGIT sample, a somewhat different result from that of Karska et al. (2013), based on a more complete comparison of cooling by various species.

Manoj et al. (2013) analyze the Herschel Orion Protostar Survey (HOPS; PI: T. Megeath) sample of protostars in Orion. Their sample includes 21 protostars ranging 1–200 L_{bol},
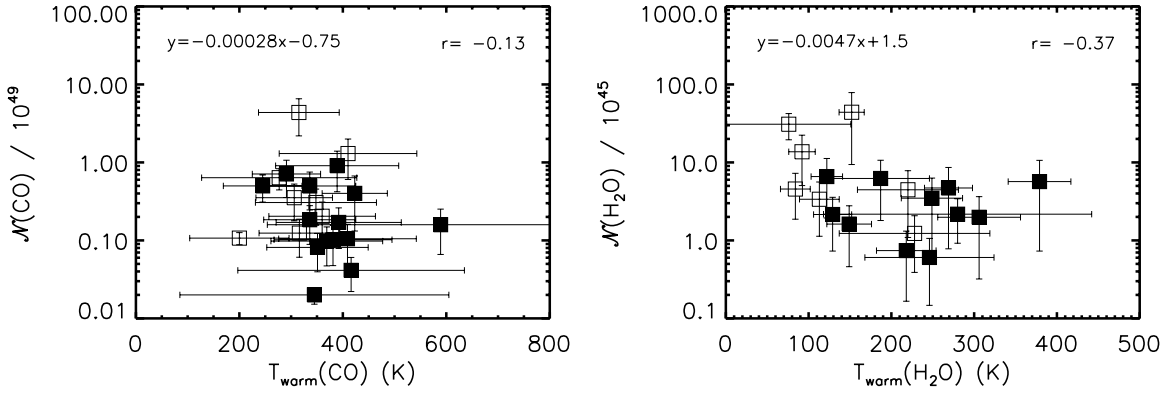
Figure 24. Left: $\mathcal{N}_{CO}$ vs. $T_{warm}(CO)$, illustrating a lack of correlation between other properties and rotational temperature. Right: same comparison for H_2O. In all panels, Class 0 sources (according to T_{bol}) are plotted as open symbols and Class I sources are plotted as filled symbols.
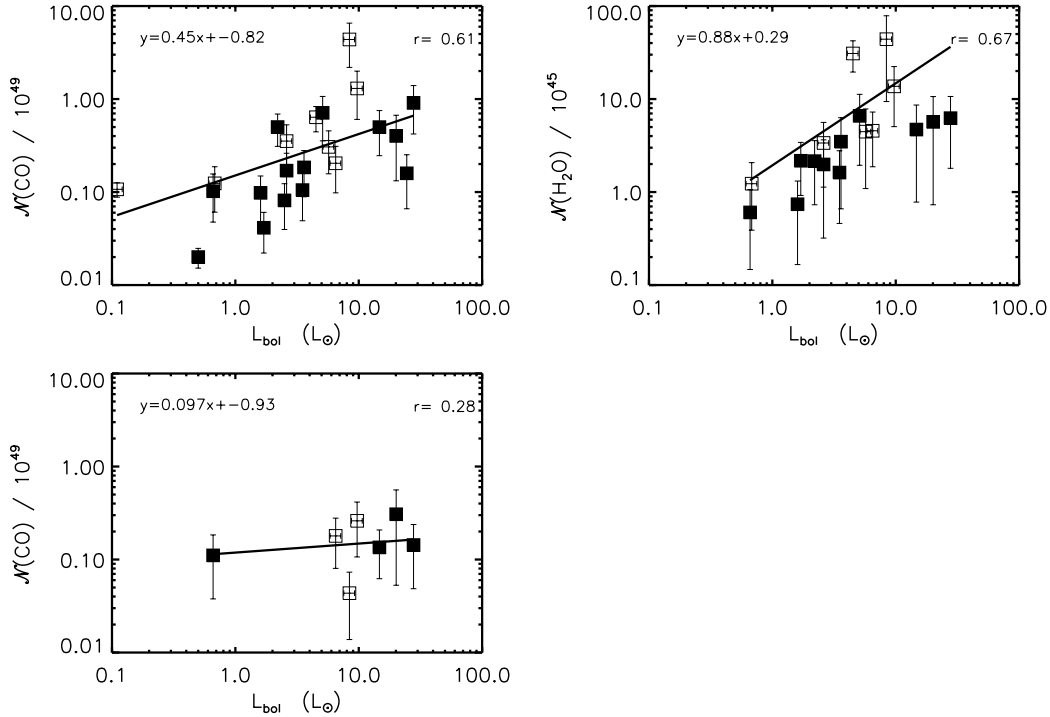

Figure 25. Top left: $\mathcal{N}_{CO}(warm)$ vs. L_{bol}. Top right: $\mathcal{N}_{H_2O}$ vs. L_{bol}. The values are correlated over two orders of magnitude, for both CO and H_2O. B1-c exhibits an order of magnitude higher $\mathcal{N}_{H_2O}$ than the sample correlation would suggest, but this is likely due to large uncertainties in the fit, taken from only four lines. The greatest outlier is L1551-IRS5, which exhibits from low luminosity in CO, and no detected H_2O. Bottom left: $\mathcal{N}_{CO}$ (hot)/(cold) vs. L_{bol}. Only the seven sources with both components detected (i.e., at least five CO lines above $J = 24 \rightarrow 23$ in excitation energy) are shown. In all panels, Class 0 sources (according to T_{bol}) are plotted as open symbols and Class I sources are plotted as filled symbols. In each case, we take the uncertainty in L_{bol} to be dominated by the overall calibration uncertainty of 10%.
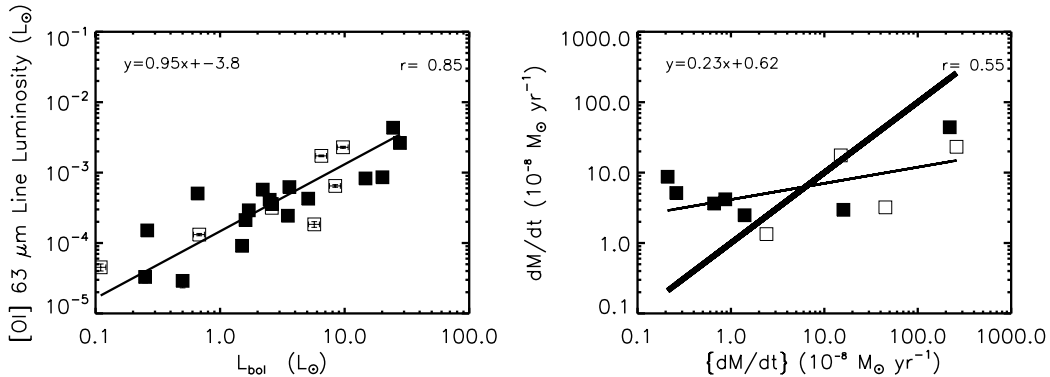
Figure 26. Left: [O I] 63 μm luminosity ($L_{\odot}$) vs. L_{bol} ($L_{\odot}$) for the DIGIT embedded sources sample. Right: outflow rate derived from [O I] 63 μm luminosity (10^{-8} $M_{\odot}$ yr^{-1}) vs. outflow force derived from CO $J = 3 \rightarrow 2$ (10^{-5} $M_{\odot}$ yr^{-1} km s^{-1}) divided by a velocity of 1000 km s^{-1}, for sources in the DIGIT embedded sources sample. The outflow rate is derived from ground-based CO $J = 3 \rightarrow 2$ maps. The thin solid line is a fit to the data, while the thick line assumes a match between the current and time-averaged values, at a velocity of 1000 km s^{-1}. In all panels, Class 0 sources (according to T_{bol}) are plotted as open symbols and Class I sources are plotted as filled symbols.
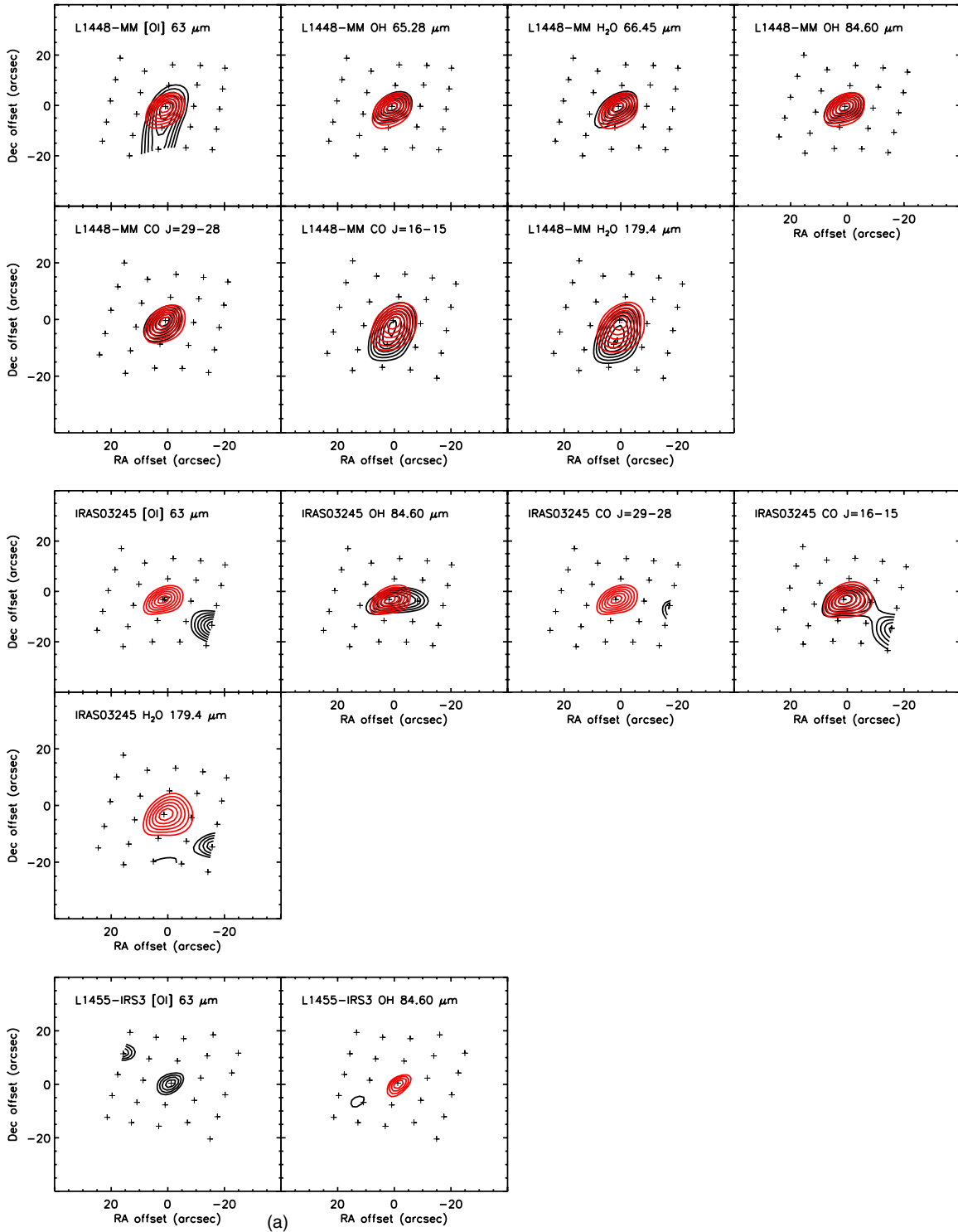
Figure 27. (a)–(j) Spatial distribution of lines (black) vs. local continuum (red). The contours are in increments of 10% from the peak flux (usually in the central spaxel), plotted down to the noise limit. The noise limit is computed as 2× the average flux of the outer ring of 16 spaxels, with the exception of the IRS 46/44 map, for which we avoid the edge spaxels containing IRS 44. (i) Note that in the case of IRS 46, the [O I] and CO lines are detected in the central spaxel, but at less than 10% the peak value from IRS 44 (see Table 5); thus it does not appear at the 10% significance level compared with contours derived from IRS 44.

(A color version of this figure is available in the online journal.)

spanning a similar dynamic range but approximately an order of magnitude brighter than the DIGIT sample. They find similar excitation for CO, but also detect higher transitions, ranging up to $J = 46 \rightarrow 45$. Using the same breakpoint in their rotation diagrams, they find a median $T_{\rm rot}$(warm) of 315 K (354 K for DIGIT), and $T_{\rm rot}$(hot) ranging from 703 to 924 K (690–1290 K for DIGIT under similar assumptions). Although they consider more luminous sources compared with DIGIT, the HOPS team
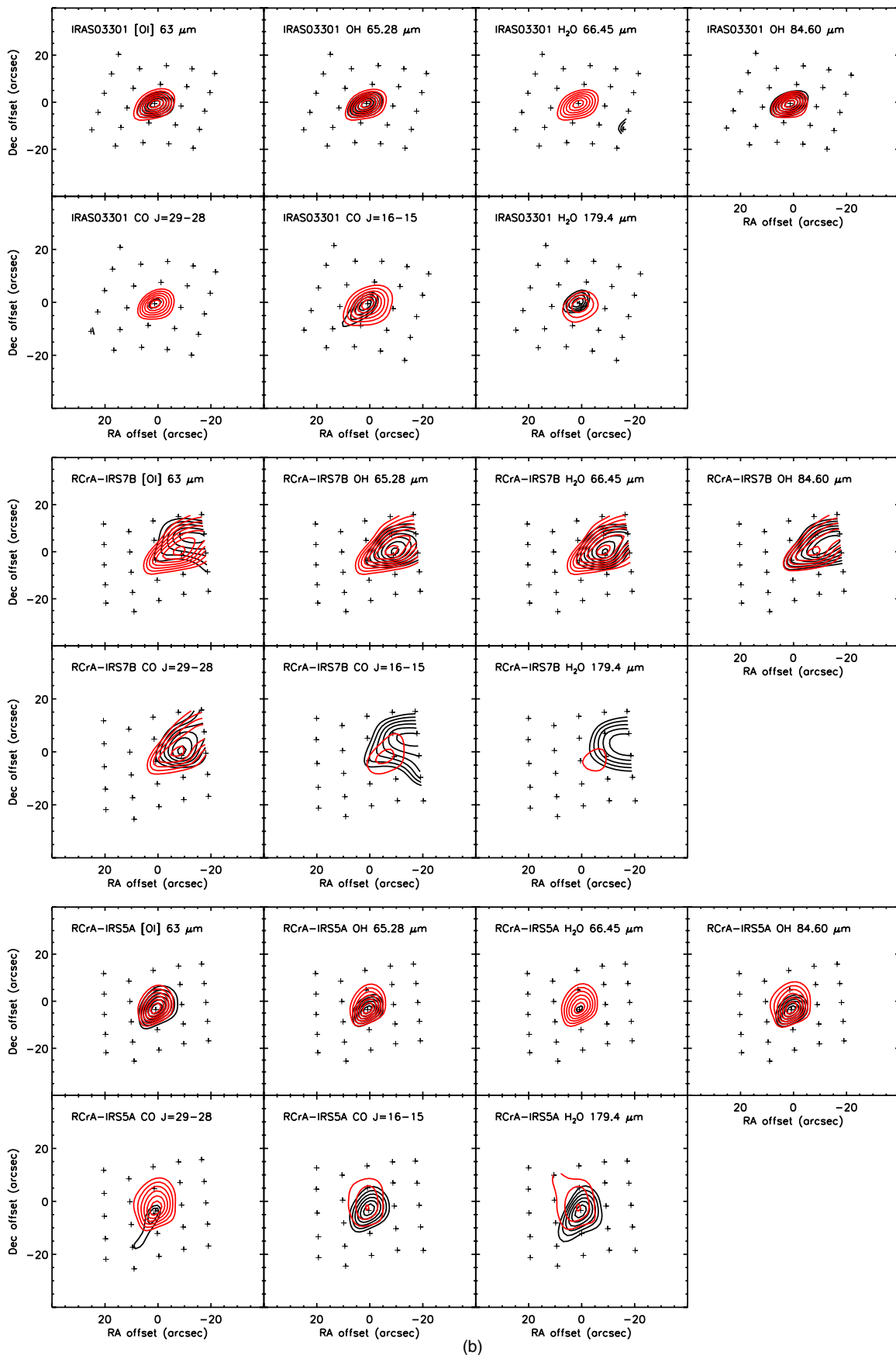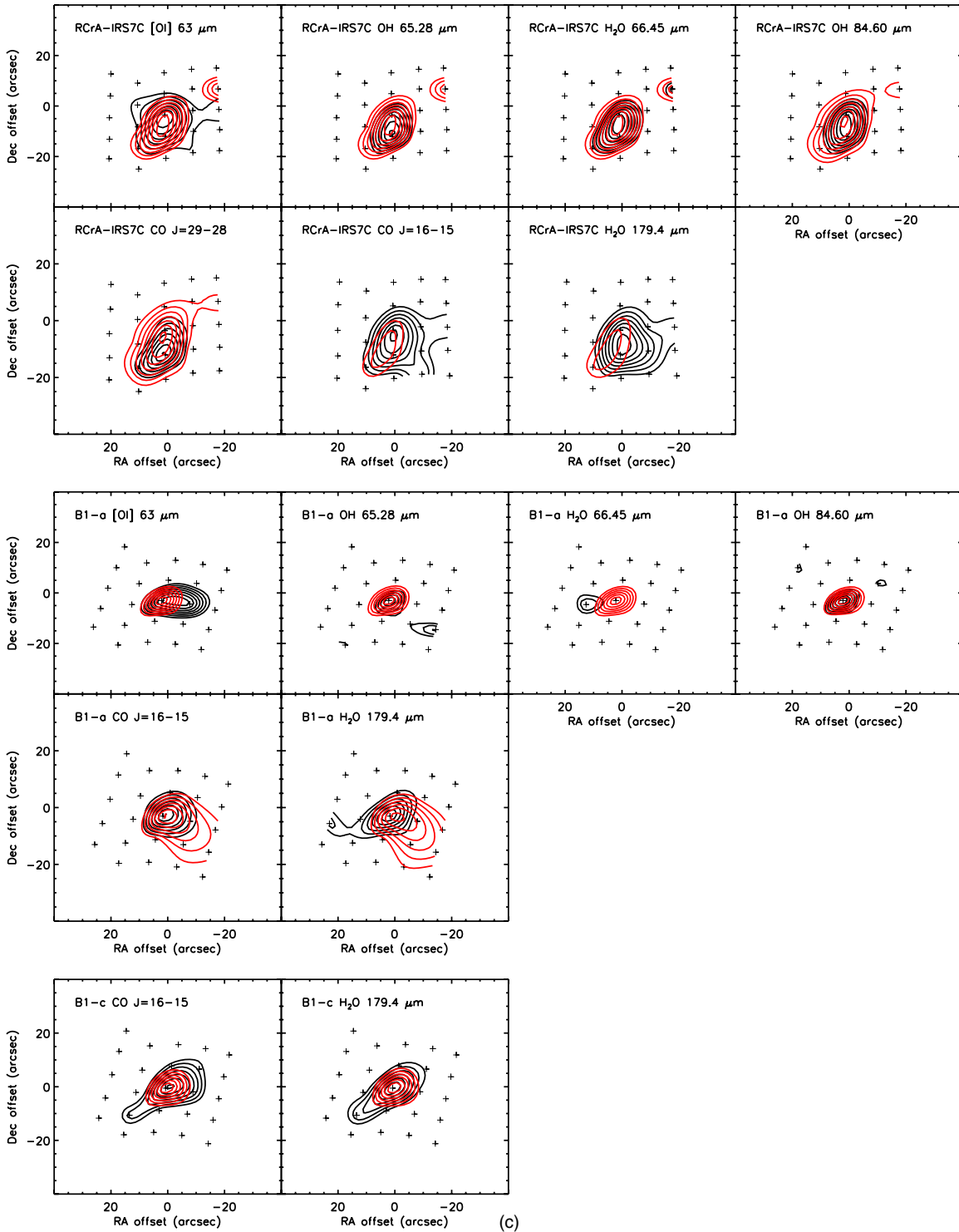
Figure 27. (Continued)

Figure 27. (Continued)

finds a similar lack of correlation between T_{rot} and L_{bol}. In combination with our results, we suggest that there is no trend between T_{rot} and L_{bol} over three orders of magnitude in L_{bol} (from 0.1 to 200 $L_{\odot}$). Manoj et al. (2013) posit sub-thermal excitation using the prescription from Neufeld (2012). Although the DIGIT sources are nearer to us than the HOPS sources and thus closer to being spatially resolved, the DIGIT CO results are

consistent with both the sub-thermal low density/high temperature solution and the thermal/low temperature (close to T_{rot}) solution.

6.2. [O I] 63 μm Emission as a Wind Indicator

Hollenbach & McKee (1989) suggested that emission of [O I] would be a good tracer of the current mass loss rate in a stellar
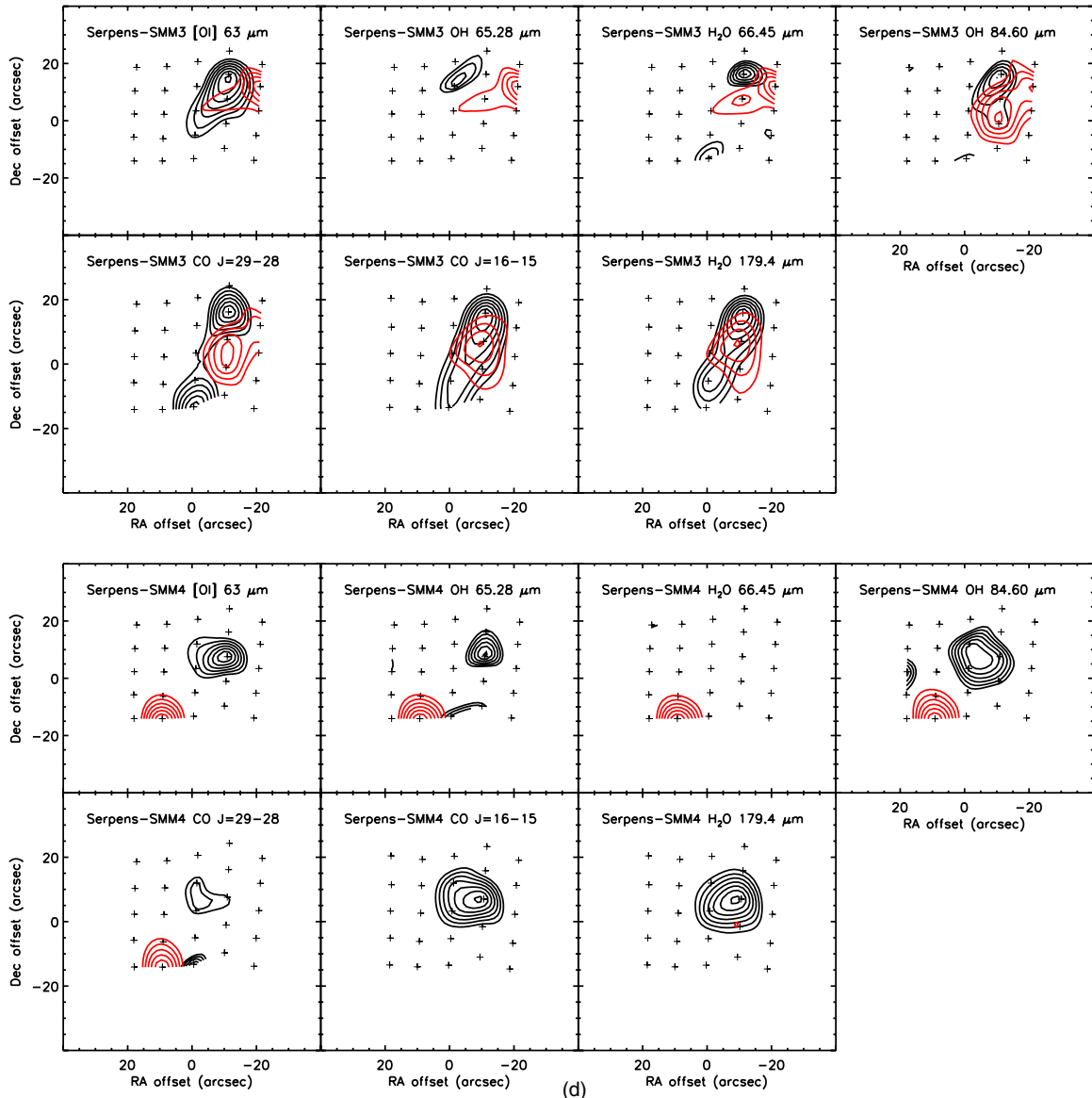
Figure 27. (Continued)

wind. In Figure 26, we plot the [O I] 63 μm line luminosity versus L_{bol}; it shows a significant correlation ($r = 0.85$). We also plot the mass loss rate ($\dot{M}_{wind}$) from the equation in Hollenbach & McKee (1989) versus the time-averaged mass loss rate ($\langle \dot{M}_{wind} \rangle$) derived from maps of low J CO lines collected by Yıldız et al. (2012) and Kristensen et al. (2012). Given the smaller number of sources with suitable data, the correlation is not significant. Furthermore, the relation of Hollenbach & McKee (1989) only comes close to reproducing observed fluxes if an unrealistically high wind velocity of 1000 km s^{-1} is assumed.

These data suggest that [O I] 63 μm is not a particularly good quantitative measure of the time averaged mass loss rate in these sources. However, the measurements of $\langle \dot{M}_{wind} \rangle$ from CO maps are not uniformly derived in the literature, so this question should be reexamined when a consistent data set is available. The mean [O I] 63/145 μm line flux ratio is 10.6±6.5; shock models predict ratios of 14–20, higher than typical in our sample.

7. THE ORIGIN OF THE LINE EMISSION

Since the line emission from many of the sources in this sample is distributed in a way consistent with a point source, we need to check whether it could arise in a disk. Although some disks do show many of the CO and OH lines detected in the embedded sample (Sturm et al. 2013; Fedele et al. 2012; Meeus et al. 2013; Fedele et al. 2013; C. Salyk et al. 2013, in preparation), most are not detected in gas lines other than [O I] and [C II]. Detections of H$_2$O are particularly difficult in these objects (mostly Herbig Ae/Be stars), although some features have been identified from deep PACS or HIFI exposures (e.g., Fedele et al. 2012). It is unlikely that the circumstellar disk dominates the emission in *Herschel* beams because of its small spatial extent. We can be more quantitative by comparing to disk samples. The Herbig/T Tauri sample portion of DIGIT is discussed in detail in forthcoming papers (Meeus et al. 2013; Fedele et al. 2013); we note here that the embedded sources are much more luminous in gas features than disk sources. The
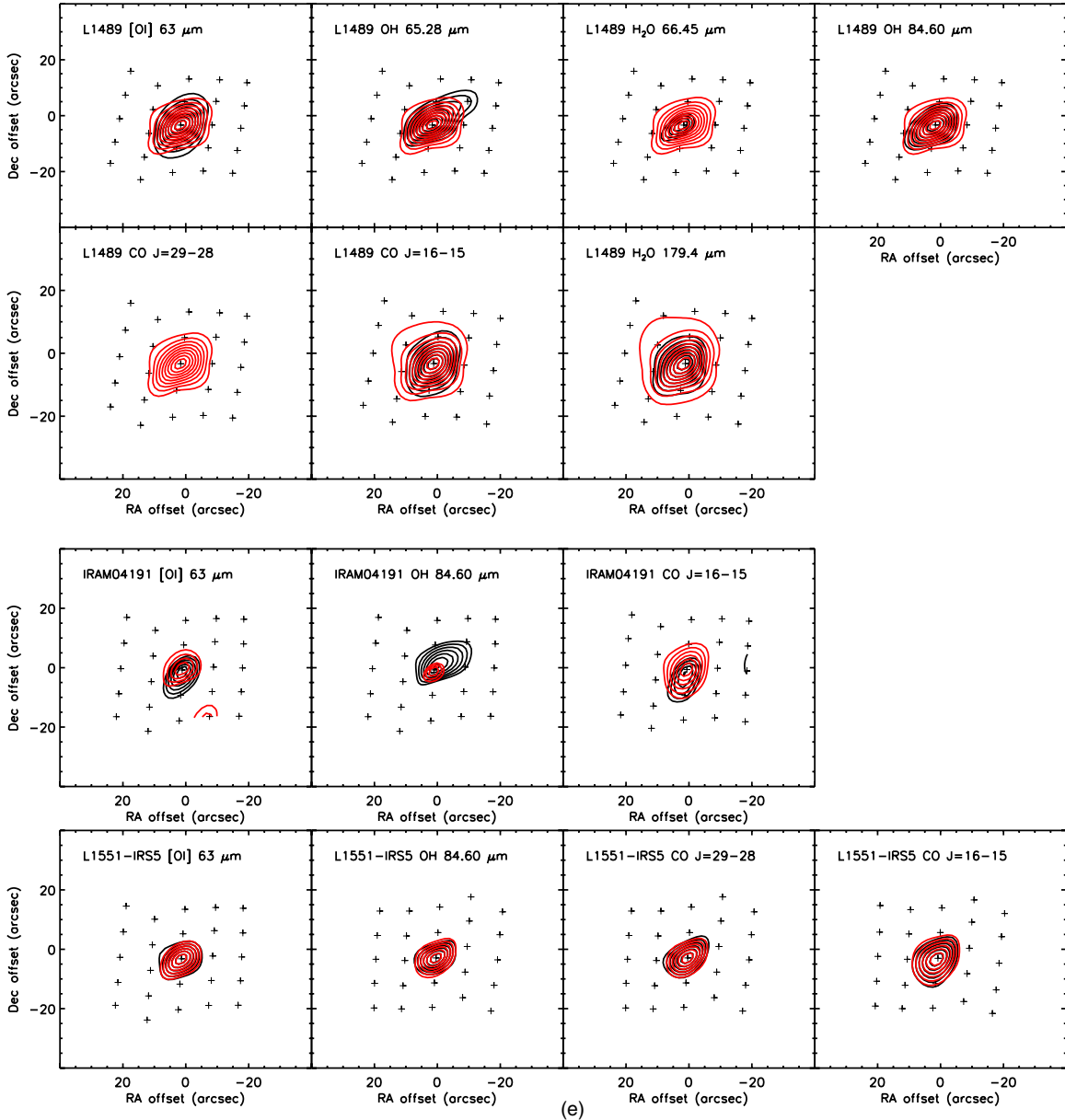
Figure 27. (Continued)

[O I] line flux in the disks sample ranges up to a few $\times\ 10^{-5}L_\odot$ roughly the same as the weakest [O I] line among the embedded sources. Similarly the CO $J = 16 \rightarrow 15$ line luminosity ranges up to $10^{-4}\ L_\odot$ in HD 100546 (Meeus et al. 2013); the range in the embedded sources is between 10^{-3} and $10^{-5}\ L_\odot$.

The closest comparison to a disk source in our embedded sample is IRS46, itself a candidate edge-on disk (van Kempen et al. 2009). It is the second-lowest luminosity source with a detected warm component in our sample (ahead of only IRAM 04191), and it has the lowest inferred $\mathcal{N}$(warm)—comparable to that of HD 100546. However, HD 100546 is a Herbig Ae/Be star with a bolometric luminosity over two orders of magnitude greater. The CO line luminosity in IRS46 is low, but follows the same relationship with source luminosity as the rest of the sample. From the line luminosity, it is consistent with disk sources, particularly T Tauri stars (Meeus et al. 2013). Thus

it is possible that the disk emission may contribute to the CO or [O I] emission in the faint sources, but it is unlikely to affect our overall statistics. It is clear from these comparisons that the circumstellar disk is not a significant contributor to the emission from embedded objects in the PACS bands.

Lahuis et al. (2010) provide an overview of many of these sources using the IRS spectra. The source sizes they derive would be unresolved by *Herschel*, with the possible exception of VLA1623. They note detections of extended [Fe II] only in L1448 and Serpens-SMM3/4—it is not detected in IRAS03245, L1455-IRS3, B1-a, B1-c, GSS30, VLA 1623, WL12, IRS63, IRS46, or the RCrA sources. VLA1623 is detected in [Si II] extended emission. There is no obvious correlation between these sources in [Fe II] or [Si II] and their [O I] emission strength, which in principle are linked as shock tracers (Hollenbach & McKee 1989). [Ne II], which is associated with the source in
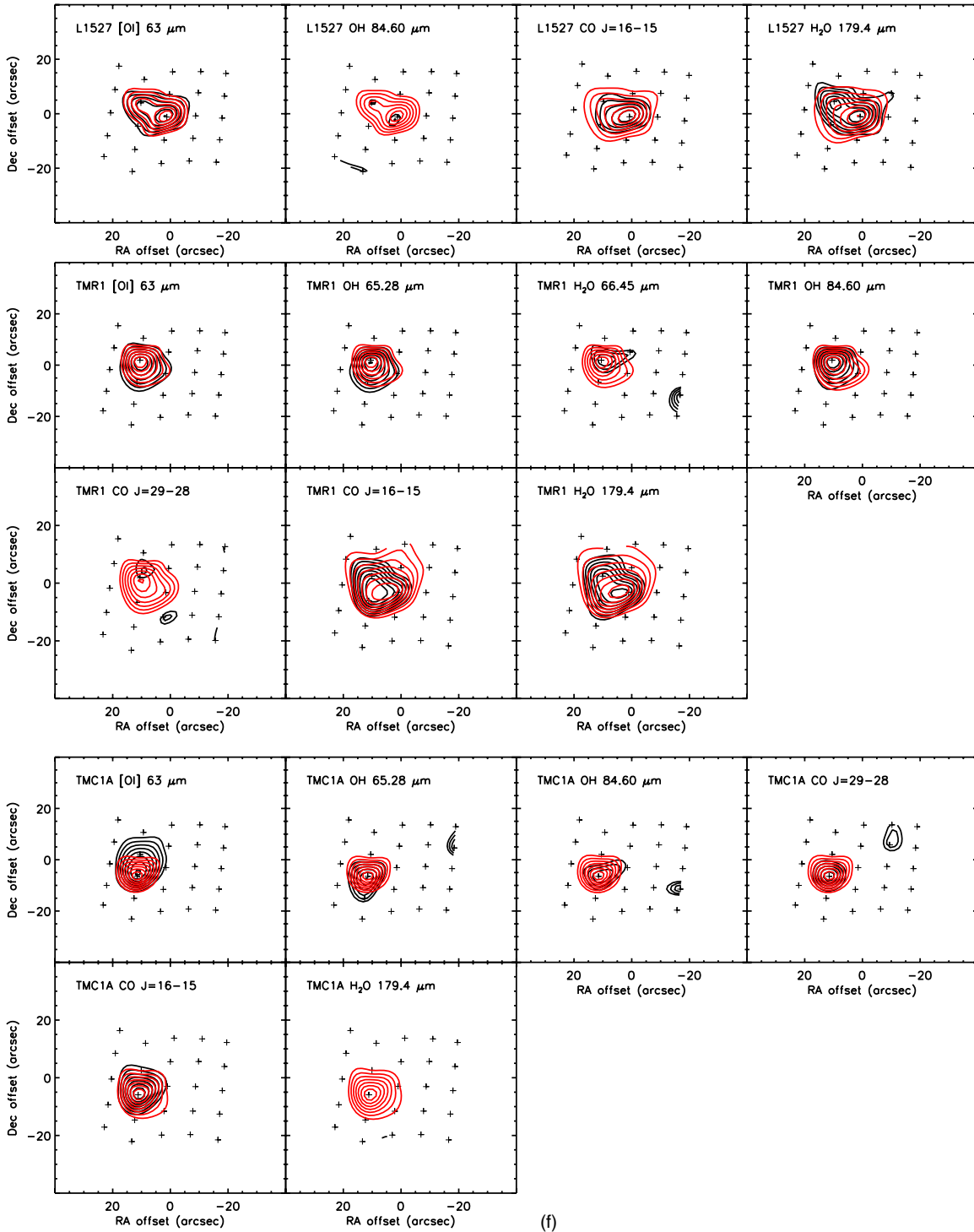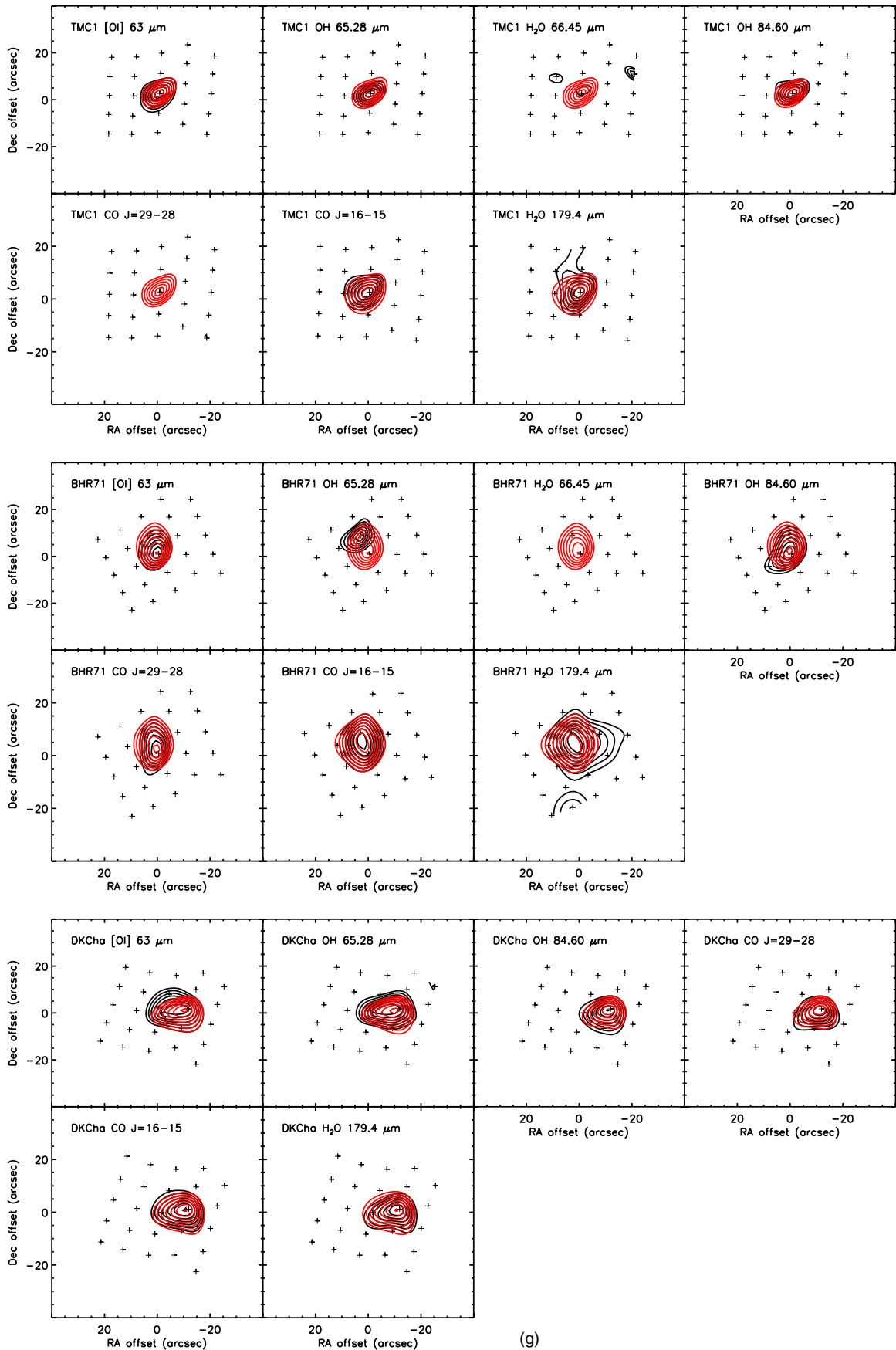
Figure 27. (Continued)

IRAS 03301, B1-a, and the RCrA sources, is also not well-correlated with [O I]. Hot H_2 is found in IRAS 03425, B1-a, B1-c, WL12, and RCrA-IRS7A/7B; the first four sources are compact in the *Herschel* data. "Warm" (in this case, $T \sim 100$ K) H_2 is much more prominent, found in all except IRAS03301, B1-c, WL12, IRS63, RCrA-IRS5, and IRS46; all of these sources except RCrA-IRS5 have relatively low L_{bol}. With the possible exception of Elias 29, we do not see evidence for a colder

component (<250 K) in PACS CO; observations with SPIRE will test the presence of this component (J. D. Green et al. 2013, in preparation). In this source, the warm component fit underestimates the CO $J = 14 \rightarrow 13$ through $J = 16 \rightarrow 15$ line intensities, hinting at a cooler component. The 500–1500 K "hot" temperature is only reported for a few sources, including B1-a at 615 K (which does not show a hot component in CO). In summary, the CO and H_2 do not seem closely linked across
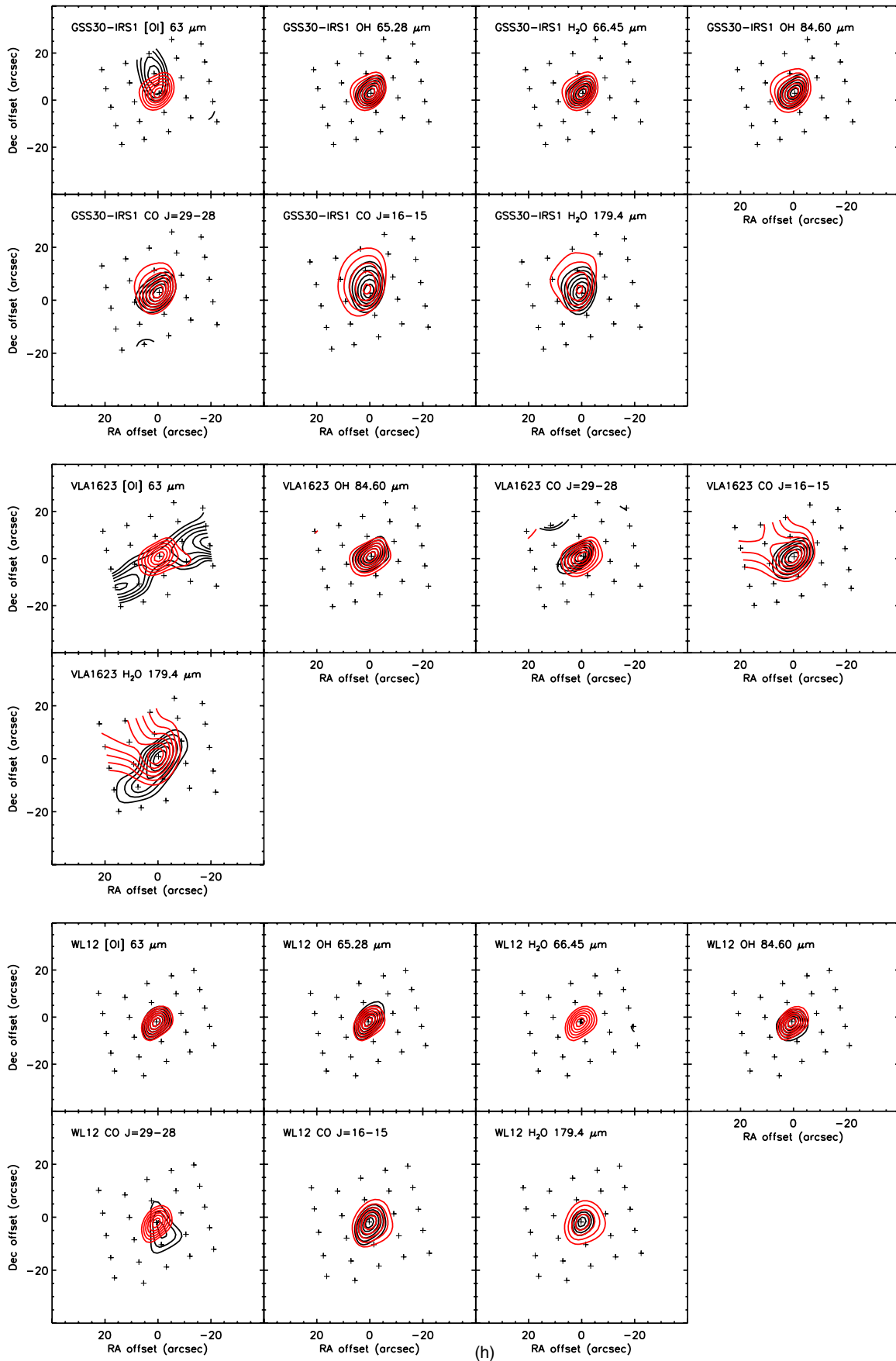
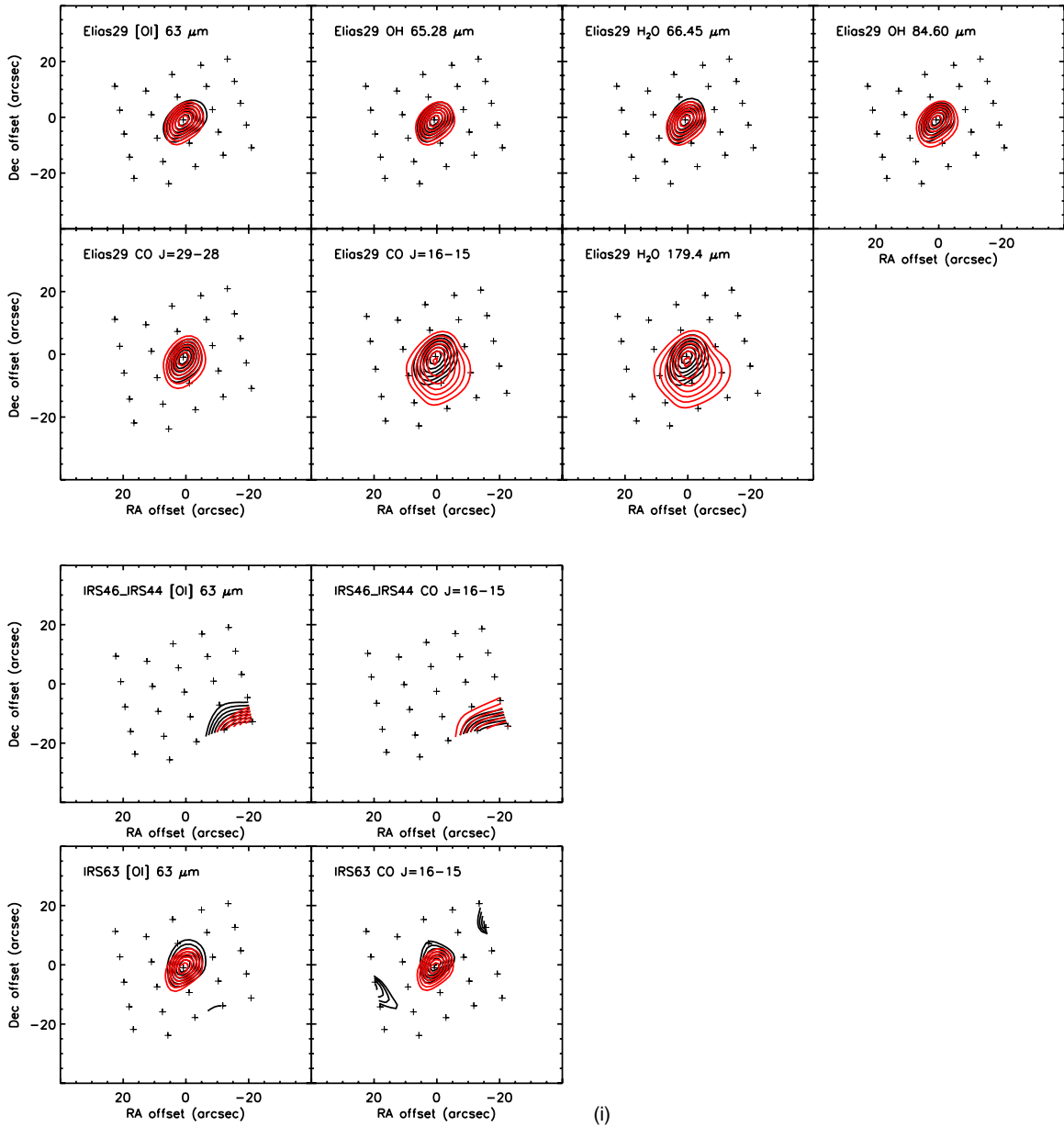**Figure 27.** (Continued)

Figure 27. (Continued)

Figure 27. (Continued)

the full sample; neither are [O I] and mid-IR fine structure lines.

The emission lines in embedded sources may arise from multiple regions of differing density and temperature; some evidence for this is found in resolved line profiles showing multiple velocity components for H_2O and CO, in high spectral resolution observations from HIFI (H_2O 557 GHz, CO $J = 16 \to 15$ and $J = 10 \to 9$; Kristensen et al. 2011; Santangelo et al. 2012; Vasta et al. 2012; Nisini et al. 2013; Yıldız et al. 2013) and ground-based instruments such as APEX (in CO $J = 6 \to 5$; van Kempen et al. 2009; Yıldız et al. 2012). The hot CO and nearly all H_2O emission may be excited by the shocks along the outflow cavity (van Kempen et al. 2010b; Visser et al. 2012), or inside the mostly evacuated outflow cavity (Manoj et al. 2013). In recent models, the UV-heating from the central protostar contributes significantly to the PACS CO lines, particularly in more evolved sources (Visser et al. 2012).

However, UV-heating seems to play only a minor role in the PACS H_2O lines, compared with heating from outflow-driven shocks (Manoj et al. 2013).

8. CONCLUSIONS

We have presented a statistical analysis of the full sample of 30 Class 0/I protostars from the DIGIT key project using *Herschel*-HIFI and PACS spectroscopy, utilizing improvements in calibration and sensitivity from the data pipeline in the first two years of the mission.

1. We present 0.5–1000 μm SEDs of all 30 sources in our sample, and refine calculations of bolometric temperature and luminosity for each source. The addition of the PACS data has a modest effect on the classification of sources by bolometric temperature in our sample, shifting the number (of the 25/30 sources with good continuum
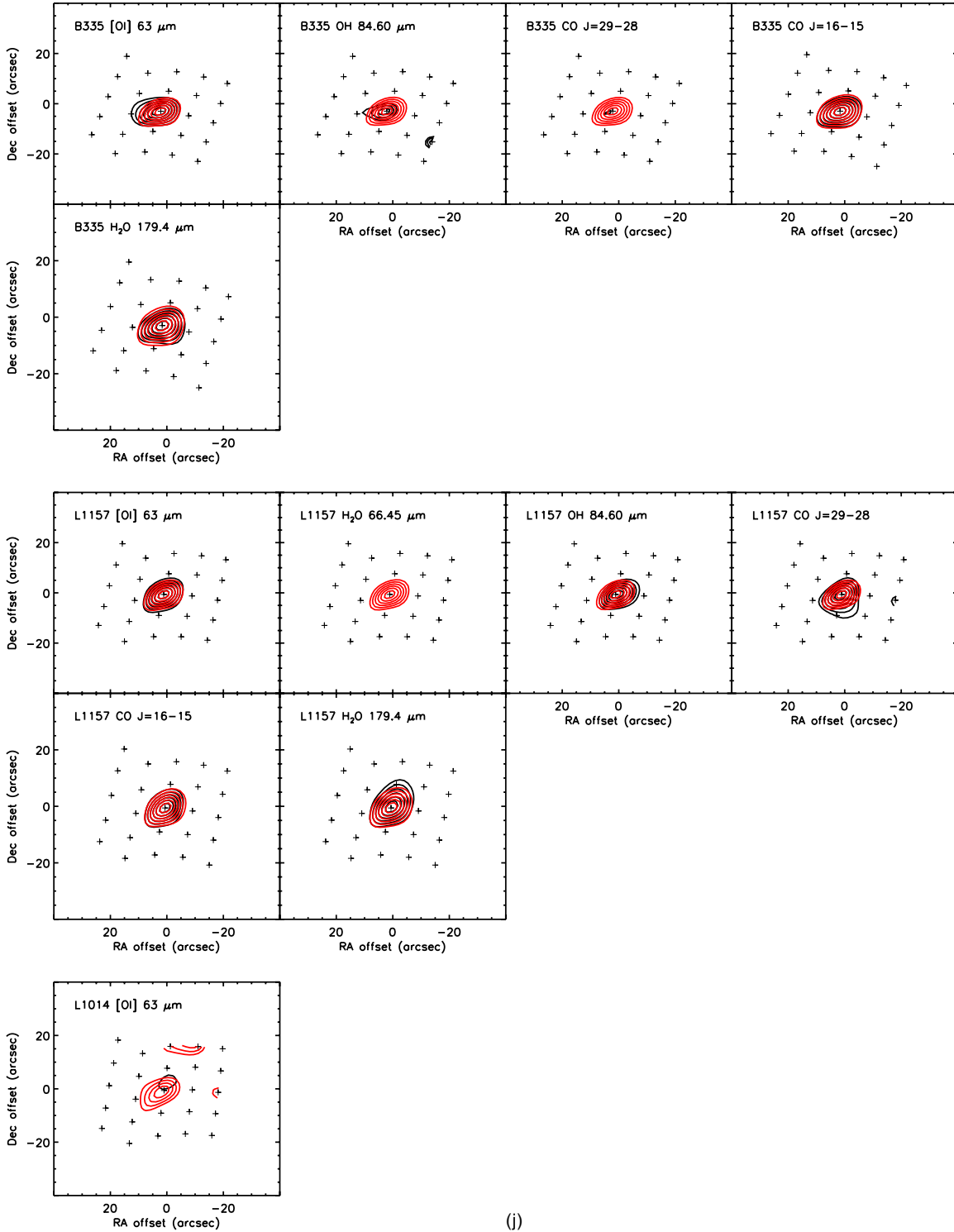
Figure 27. (Continued)

detections) of Class 0 and I sources from 8 and 17, respectively, to 9 and 16, respectively. Measured by the metric of L_{bol}/L_{submm}, we find 16 Class 0 and 9 Class I sources, unaffected by the addition of the PACS data. We do find substantial changes in L_{bol} or T_{bol} in several sources, but usually they are caused by complicated emitting regions or sparse data in the IR and millimeter regimes prior to the addition of the *Herschel* data. In the relatively isolated sources, the *Herschel* spectrum did not significantly alter the bolometric temperature or luminosity.

2. We detect over 100 rotational transitions of CO, OH, and H_2O, as well as [O I] $^3P_1-^3P_2$ and $^3P_0-^3P_1$, associated with the sources. Diffuse [C II] $(^2P_{3/2}-^2P_{1/2})$ is also detected, but its connection to the sources is weak. No other species have been identified.

3. All 30 sources show detectable line emission. We select characteristic "cool," "warm," and "hot" excitation energy

lines for each of CO, OH, and H_2O. The "warm" CO line is detected in 27/30 sources, while the "hot" CO line is detected in 22 of these. The "cool" H_2O line is detected in 24/30 sources, while the "warm" line is detected in 14 of these, although not entirely the same sources as for CO. The "cool" OH line is detected in 27/30 sources, while the "warm" OH line appears in 15 of these. The lowest excitation OH line at $119\,\mu m$ is detected in absorption toward two sources; in those sources the "cool" OH line is in emission. The 557 GHz H_2O line is detected in 9 of 13 HIFI observations, strongly corresponding with the "cool" excitation PACS H_2O. [O I] $63\,\mu m$ is detected in all but one source (B1-c).

4. In many sources, [O I] is of greater spatial extent than CO. However, even among less obviously confused source regions there are sometimes signs of multiple or extended emission sources. The positional uncertainty of line and continuum measurements is between $0\rlap{.}{''}3$ and $3''$ for most sources, comparable to reported pointing uncertainties. However, some sources were substantially ($>3''$) mispointed.

5. We constructed rotational diagrams for all CO, OH, and H_2O detections. Using a breakpoint of $E_u = 1800$ K for a two-temperature fit to the CO, and a single temperature fit for OH and H_2O, we calculate rotational temperatures and total number of molecules for each source. The rotational temperatures for CO have a mean value, $\langle T_{rot} \rangle = 354 \pm 92$ K for the "warm" component, and $\langle T_{rot} \rangle = 932 \pm 217$ K for the "hot" component, while the rotational temperatures for H_2O and OH are much lower, averaging $\langle T_{rot} \rangle = 194 \pm 85$ K and 183 ± 117 K, respectively. The scatter in the H_2O and OH is partially attributable to inhomogeneous excitation conditions among the fitted lines. The average total number of CO molecules in warm and hot components, $\langle \mathcal{N} \rangle = (0.70 \pm 1.12) \times 10^{49}$.

6. The line luminosities of H_2O and OH correlate with those of CO. The total number of molecules in warm and hot CO correlate with L_{bol}. The excitation, measured by T_{rot} or by ratios of the number of CO molecules in warm and hot components does not correlate with L_{bol}. These facts suggest that the amount of excited gas is related to the current source luminosity, but that the excitation is primarily determined by the physics of the interaction (e.g., UV-heating or a shock). No differences between Class 0 and I sources (defined either by T_{bol}, or L_{bol}/L_{submm}) are apparent in these data.

7. The [O I] $63.2\,\mu m$ line flux correlates significantly ($r = 0.85$) with L_{bol}. If used to calculate a current mass loss rate in the wind, the agreement with time averaged mass loss rates from low-J CO maps is poor.

8. There is no discernible link between *Spitzer* and *Herschel* tracers of outflowing gas (H_2 and CO, respectively) or fine structure emission ([O I] and [Fe II]/[Si II], respectively).

APPENDIX A

DATA REDUCTION RECIPE

First, we describe the initial features of reduction that are common to both methods. Each segment is first reduced using a modified pipeline based on the standard spectral reduction script with the relevant version of HIPE; these scripts are described in detail in separate subsections for HIPE 6.0 and 8.0. The "simplecube" pipeline product is a collection of all of the 16 wavelength subarrays with 25 spaxels for each wavelength ($16 \times 5 \times 5$ cubic array). The simplecube is non-uniform in wavelength, and next the pipeline rebins the cube to a uniform wavelength coverage, user-selected. The parameter to determine the uniform wavelength coverage is referred to as "oversampling"—the pixels in the reduced data covering each resolution element. We used an oversampling rate of 2, closely matching the sampling rate of the raw PACS data, with an exception in the case of our science demonstration phase data for DK Cha. This object was observed using a slightly different setup not sufficiently sampled in wavelength, and we reduced our oversample to 1. This process yields two spectral cubes ("rebinned cubes") consisting of 5×5 spaxels for each wavelength, over a uniform set of wavelengths covering the entire module, for each nod position. The nod averaged product ("finalcube") is the average of the two nods and is the final standard data product from the pipeline. The relative spectral response function (RSRF) was determined before launch but modified using calibration data taken in the early phases of the mission, from observations of Neptune, to yield a flux density in jansky (Jy).

After this point, we used two different procedures, optimized to produce the best results for continuum and lines, respectively. This dual procedure was necessary to produce reliable absolute flux calibration, while also obtaining the best S/N on continuum and lines. For convenience, we refer to these two reductions as the "bgcal" (background calibrated; best for absolute flux calibration) and "calblock" (calibration block; best for S/N) spectra.

A.1. Continuum

First, we determined the centroid position of the continuum (using the HIPE 6.0 reduction) for two wavelength regions in each segment, selected to avoid detectable line emission. Using maps of these regions, we were able to interpolate a peak position to within 0.2 spaxel widths. We find by this method that most of the sources have continuum centroids that fall between $0\rlap{.}{''}2$ and $3\rlap{.}{''}0$ of the center coordinates, with the majority landing within $2''$ (0.2 spaxel widths) of the center. For those sources, the pointing is consistent between the "blue" and "red" observations, independent observations executed at different times.

Second, in order to produce a spectrum with the best S/N and an accurate absolute flux density, we chose two apertures for each spectrum: a smaller aperture (S_{sm}) chosen for the best S/N, and a larger aperture (S_{lg}) that included all of the source flux for calibration. To do this, we determined by inspection which spaxels contained high-S/N spectra of the source continuum and summed the flux in those spaxels, producing a single spectrum:

$$S_{sm} = \Sigma_i S_i (\text{high S/N}). \tag{A1}$$

In most cases, we simply use the central spaxel for this purpose. For some sources we measured a centroid offset from the center of greater than 0.2 spaxels; in these cases we include additional spaxels with significant continuum.

Third, we determined the largest set of spaxels containing the source without contamination from other sources in the field-of-view; in most cases this was the full 5×5 array, but in some cases we selected a smaller set of spaxels (see section on extended emission, below). We then computed the flux density summed over these spaxels (the total flux), S_{lg}:

$$S_{lg} = \Sigma_i S_i. \tag{A2}$$

Fourth, we fitted a second (or smaller) order polynomial scaling factor in wavelength, determined from the ratio of the flux density in the larger aperture (S_{lg}) to that in the smaller aperture (S_{sm}):

$$S_{lg}/S_{sm} \approx a\lambda^2 + b\lambda + c, \tag{A3}$$

where λ is wavelength, and a, b, and c are fitted constants.

Fifth, we scale S_{sm} to S_{lg} using this correction factor:

$$S_{final} = S_{sm} \times (a\lambda^2 + b\lambda + c). \tag{A4}$$

This correction is applied module-by-module (e.g., a separate polynomial for each range of 50–75, 70–95, 100–145, and 145–190 μm). After scaling S_{sm} to S_{lg}, the two "blue" (50–75 and 70–95 μm) and the two "red" (100–145 and 145–190 μm) modules were generally well-aligned with each other (less than 5% difference on average), but retained the S/N of S_{sm}. Unfortunately, even after applying this entire procedure, $S_{lg}(\text{red}) > S_{lg}(\text{blue})$ in all cases, a systematic discontinuity at 100 μm for every source.

A.2. Lines

Our reduction technique for lines utilizes HIPE 6.0 *and* HIPE version 8.0.2489 with the "calibration block," referred to as the "calblock" reduction, which multiplies the chopped spectrum by a similar spectrum of an on-board calibration source. It works in a similar fashion to the continuum procedure, but with several key differences.

Our objective here is to measure line EWs for gas phase lines, which are spectrally unresolved, or in a few cases, perhaps slightly resolved. This reduction produced the lowest local (point-to-point) noise but larger shifts between modules and an overall calibration less consistent with photometry. Tests indicate that the EW of lines is independent of reduction. Consequently, we use the calblock reduction to define the EW of lines and then use the bgcal reduction of the same spectral region to convert to line fluxes. Mathematically, the process is as follows:

$$EW = F_{line}(\text{calblock})/S_\lambda(\text{calblock}), \tag{A5}$$

where S_λ is the adjacent continuum flux density, with units of W m^{-2} μm^{-1}, and F_{line} is the line flux, with units of W m^{-2}, followed by

$$F_{line}(\text{Final}) = EW \times S_\lambda(\text{bgcal}). \tag{A6}$$

The first step is to extract line fluxes from the HIPE 8 calblock reduction using a narrow region to define the continuum (S_λ) and calculate the EW. We utilized a modified version of the SMART reduction package (Higdon et al. 2004) to fit Gaussians and first or second-order baselines to the spectra to remove local continuum features. The LAMDA database of lines (Schöier et al. 2005), supplemented by HITRAN (Rothman et al. 2005), was used to identify the features. The fit for the line center varies only by 0.01 μm or less for our different extraction methods (10%–20% of a resolution element); therefore the fit uncertainty in velocity space is ~30–50 km s^{-1}. Line centers usually lie within 50 km s^{-1} of the theoretical line center from laboratory measurements. At our level of precision, we do not observe believable shifts in our data; nonetheless, this is still consistent with shifts observed in other datasets (e.g., Karska et al. 2013). However, the location of the source within each slit also affects the velocity. The uncertainty in EW caused by the fit is quite small (S/N ratios as high as 300 were obtained on bright lines, particularly [O I]), but for faint lines, the uncertainty rises to 20%. In this treatment we do not include lines within the masked wavelength regions (<55 μm, 95–102.5 μm, >190 μm) as they exhibit large calibration uncertainties. The one exception is the CO $J = 27 \rightarrow 26$ line at 96.77 μm; the local rms uncertainty is somewhat larger than, but still comparable to, the local continuum surrounding the CO $J = 28 \rightarrow 27$ line at 93.3 μm, and we only include this line in sources with confirmed detections of CO lines at shorter wavelengths. The line does not significantly affect the derived source properties in the following sections.

A.2.1. Corrections for Spatial Extent, and Comparison to the Empirical PSF

Second, the line fluxes were corrected for PSF and extended emission. As with the continuum, simply adding all the spaxels caused a serious loss of S/N and a diminished rate of line detection, and the PSF correction provided in the standard pipeline does not account for extended emission. Thus we do *not* use the PSF correction function, but instead compare the flux over different sized apertures to determine an empirical correction for each source. In order to do this, we measured the line flux, $F_{line}(\text{sm})$, in the central spaxel (or a sum over a few spaxels for poorly centered sources) that gave the best S/N on relatively strong lines. Mathematically, the process is identical to the continuum, except for line flux rather than flux density:

$$F_{line}(\text{sm}) = \Sigma_i F_{line}(i), \tag{A7}$$

where i is the set of spaxels with good S/N on all lines.

Additionally, we correct the fluxes by the ratio between the bgcal and calblock local continuum for each individual line. Because the spatial distribution of line emission could in principle differ from that of the continuum, we did not simply scale the value in the central spaxel by the continuum ratios. To determine the total line fluxes, $F_{line}(\text{lg})$, we applied a polynomial correction, developed by comparing the spectral line flux detected in the central spaxel compared to that in the surrounding spaxels for strong lines—mostly CO lines, but also including strong H$_2$O lines. We did not include the 63

and 145 μm [O I] lines in this correction because they were frequently extended compared with these species and to the PSF (see Section 3.1). Weaker lines of all species were then scaled with the same factors.

Mathematically, the procedure is similar to the correction to the continuum. First, the line fluxes, measured originally from the calblock reduction, are scaled to the bgcal level. Then, as for continuum we derive the small aperture line flux (F_{line}(sm), typically the central spaxel) and the large aperture (F_{line}(lg)). Then we correct the final line fluxes (F_{line}(final)) by a first-order polynomial fitted to the ratio of the fluxes in the apertures. We only summed over the central 3×3 spaxels to calculate F_{line}(lg), rather than the full (5×5) array. Mathematically:

$$F_{line}(lg) = \Sigma_i F_{line\,i} \qquad (A8)$$

where i is the index of the spaxels falling within the large aperture:

$$F_{line}(lg)/F_{line}(sm) \approx a\lambda + b \qquad (A9)$$

$$F_{line}(final) = F_{line}(sm) \times (a\lambda + b). \qquad (A10)$$

This method assumes that weak and strong lines have similar spatial distributions. In Figure 2, we plot line fluxes of all species measured from 3×3 spaxel regions versus line fluxes contained within just the central spaxel, for four well-pointed sources. For each source we fit a constant ratio from 50–100 μm, and a first order polynomial from 100 to 200 μm, a simplified fitted version of the PSF correction, to the bright CO and H_2O lines. For this exercise we set a minimum correction factor of 1.4 to the 50–100 μm fit, approximately the PSF correction. Although additional lines are plotted, they are not considered in the fit. In cases for which we lack sufficient strong lines to determine the correction, we use a linear approximation to the PSF correction.

A.3. Detailed Steps in the Pipeline Procedure for HIPE6 (Continuum)

The HIPE pipeline is a Python script that executes Java modules line-by-line in the interactive environment. The "flux calibrated" version of our script uses calibration sets that were part of HIPE 6.0. The steps executed in the pipeline are as follows, through Level 0 (raw data), Level 0.5 (sliced data frames), Level 1 (the datacubes at the raw, non-uniform wavelength sampling), and Level 2 (the final datacubes after wavelength calibration, rebinning, nod averaging).

First, we step the data from Level 0 to 0.5. Saturated frames are flagged and removed from the ramps. The data is converted from digital flux units to volts. The timestamp of the observation is reconstructed from the header, and pointing information is added. Next the details of the chopper throw are reconstructed ($6'$ in the case of all DIGIT observations in this paper, or the "large chopper throw" setting). Then a correction is applied for *Herschel*'s velocity based on the pointing, UTC time, and location of *Herschel*. Next, noisy/bad pixels are flagged. Finally the data is split into manageable "slices" to conserve RAM, and the Level 0.5 products are produced.

Next the data is reduced to Level 1. First, the masks are removed to apply the glitch-flagging routines, producing a glitch mask. The signal level is converted to the reference integration capacitance using a calibration file. A differential signal is computed for each on/off-position pair of datapoints, for each chopper cycle. Then the spectrum is divided by the RSRF, and the nominal response function, in effect a flatfielding correction

utilizing calibration observations of Neptune and Vesta. This is then recorded as a "PacsCube" dataproduct, which contains the spectrum *prior* to wavelength calibration, rebinning and nod averaging; this is the Level 1 product.

The last set of pipeline subroutines takes the Level 1 product to Level 2. A user-selected "oversampling" parameter is used to rebin to a uniform spectral resolution. An oversample of 2 indicates that the data are binned so that each resolution element is covered by two pixels in the reduced data. Outliers are flagged with sigma-clipping in the wavelength domain. The "RebinnedCube" product is the output of this routine, a spectrum for each nod-difference spectrum. In the standard chop-nod setting, this produces two spectra. The final step is to take the difference of the two nods by combining the two RebinnedCube products into a single "FinalCube" product, for each of the 25 spaxels. A post-HIPE routine is used to convert this to a datacube for final analysis.

A.4. Detailed Steps in the Pipeline Procedure for HIPE8 (Lines)

The best S/N is in most cases generated using the current pipeline calibration set from HIPE 8.0.2489. The steps executed in this version of the pipeline are similar to the HIPE 6.0 procedure, but with significant differences.

To step from Level 0 to 0.5, the pipeline begins by flagging and removing saturated frames from the ramps. Then the signal is converted from digital flux units to volts. Next the timestamp and spatial coordinates of each pixel are reconstructed from the header. The wavelength calibration is determined. A correction is applied for *Herschel*'s velocity based on the pointing, the location of *Herschel*, and UTC time. Noisy/bad pixels are flagged, as are data affected by chopper and grating movement.

Next the data are processed to Level 1. The masks are removed to apply the glitch-flagging routine and to make a glitch mask, and then all masks are activated. The signal is converted to reference integration capacitance. *In the case of the DIGIT pipeline, we derive the detector response from the standard calibration block to improve S/N, rather than the standard pipeline procedure.* Then the on–off position difference signal is computed for each pair of datapoints per chopper cycle. The signal is divided by the RSRF; an independent function is applied for each module. The flatfield is refined using a sub-procedure. Finally the frames are converted to a set of PacsCubes, the Level 1 dataproduct.

The last subsection processes the data to the Level 2 stage, where they are ready for analysis. First, the good (unmasked) data is located, and an upsample of 1 and oversampling parameter of 2 are used, in all cases except for the science demonstration phase observations of DK Cha (which was executed in a slightly different engineering mode that lacked sufficient spectral sampling for an oversample of 2; in this case we select oversample=1). A clarification on terminology: in the context of PACS, upsampling refers to the addition of artificial bins between datapoints; an upsample of 1 does not use this interpolation. Oversampling indicates a rebinning to a user-defined wavelength scale: the oversampling parameter indicates the number of pixels covering each element in the reduced data. The wavelength grid is set by these parameters to rebin the data. A 5σ clipped mean flags and removes any remaining outliers. The data is rebinned at the selected sampling to create a pair of RebinnedCube products (one each for the source difference with Nod A, and the source difference with Nod B). Finally

the RebinnedCubes are averaged to form a single "FinalCube" product.

As an additional post-processing step, we apply a PSF correction (derived from the PACS manual) to the well-pointed (centroid within $\sim 2''$ of the center coordinates of the central spaxel), pointlike (non-extended) sources in our sample. This does not apply to any sources in the DIGIT embedded sample, which show some indication of extended or diffuse emission.

APPENDIX B

COMPARISON OF SPATIAL EXTENT FOR LINES AND CONTINUUM ACROSS THE DIGIT SAMPLE

In this section, we present the spatial distribution of all detected spectral lines in the DIGIT embedded sample (black), plotted against their local continuum (red) emission, drawn from linefree portions of spectra within $1\,\mu$m of the target line. We plot 10% contours (Figure 27), cutting off at twice the rms noise of the outer ring of spaxels, except where noted below.

APPENDIX C

PROCEDURE TO CREATE A ROTATIONAL DIAGRAM

The line luminosities are simply computed from the line fluxes:

$$L_J = F_{\text{line}} \times 4\pi D^2, \tag{C1}$$

where D is the distance to the source. We use the subscript J as shorthand for the full state descriptor for the more complex species characterized by multiple quantum numbers.

If the emission lines are optically thin, the total numbers of molecules in the upper state of the transition, $\mathcal{N}_J$, are related to the line luminosities by

$$\mathcal{N}_J = L_J/(A(J)h\nu(J)), \tag{C2}$$

where $A(J)$ and $\nu(J)$ are the Einstein coefficient and frequency of the transition.

These populations can also be characterized by a Boltzmann distribution:

$$\frac{\mathcal{N}_J}{g_J} = \frac{\mathcal{N}}{Q} \exp\left(\frac{-E_u}{T_{\text{rot}}}\right), \tag{C3}$$

where Q is the partition function and $\mathcal{N}$, g_J, and E_u are the total number of molecules, degeneracy of the upper level, and excitation energy (in K), respectively, of upper state J.

When the logarithm of $\mathcal{N}_J/g_J$ is plotted versus E_u, this rotation diagram can provide a first, rough diagnosis of the physical conditions in the emitting gas. If the lines are optically thin and the energy level populations are characterized by a single effective temperature (T_{rot}, which may or may not correspond to the kinetic temperature T_K) the points can be fitted by a straight line, with slope of $-T_{\text{rot}}^{-1}$. If the rotational temperature is in equilibrium with the kinetic (translational) temperature ($T_{\text{rot}} = T_K$), the temperature of the emitting gas is determined. The intercept of the fit, together with an evaluation of Q, provides a measure of the total number of molecules in all levels ($\mathcal{N}$). For simple, linear molecules (Kassel 1936),

$$Q = kT/hcB, \quad hcB \ll kT, \tag{C4}$$

where h is Planck's constant, c is the speed of light, k is Boltzmann's constant, and B is the rotational constant for the species in question. $B = 192.25$ m^{-1} for CO. For H$_2$O we

used a polynomial function in terms of T_{rot} to find Q (Fischer & Gamache 2002):

$$Q = -4.9589 + 0.28147 \times T_{\text{rot}} + 0.0012848 \times T_{\text{rot}}^2 \\ - 5.8343 \times 10^{-7} \times T_{\text{rot}}^3 \tag{C5}$$

and for OH:

$$Q = 7.7363 + 0.17152 \times T_{\text{rot}} + 0.00034886 \times T_{\text{rot}}^2 \\ - 3.3504 \times 10^{-7} \times T_{\text{rot}}^3. \tag{C6}$$

Note that the equations for H$_2$O and OH apply if a single T_{rot} between 100 and 450 K describes the populations.

If the lower excitation lines become optically thick, the state populations derived from the optically thin approximation would exhibit curvature and diverge from the fitted line. If the higher excitation lines are sub-thermally populated, the derived state populations may fall below the fitted line. Neither of these effects is seen in CO rotation diagrams for this sample, for which the direct correspondence between E_u and the wavelength of the transition simplifies the analysis, but they are likely to cause some of the larger scatter in the diagrams for OH and H$_2$O.

REFERENCES

Apai, D., Tóth, L. V., Henning, T., et al. 2005, A&A, 433, L33
Benedettini, M., Busquet, G., Lefloch, B., et al. 2012, A&A, 539, L3
Boogert, A. C. A., Pontoppidan, K. M., Knez, C., et al. 2008, ApJ, 678, 985
Brinch, C., Crapsi, A., Hogerheijde, M. R., & Jørgensen, J. K. 2007, A&A, 461, 1037
Ceccarelli, C., Caux, E., Loinard, L., et al. 1999, A&A, 342, L21
Ceccarelli, C., Haas, M. R., Hollenbach, D. J., & Rudolph, A. L. 1997, ApJ, 476, 771
Chen, H., Myers, P. C., Ladd, E. F., & Wood, D. O. S. 1995, ApJ, 445, 377
Chen, X. P., Launhardt, R., & Henning, T. 2007, A&A, 475, 277
Cieza, L. A., Olofsson, J., Harvey, P. M., et al. 2013, ApJ, 762, 100
de Graauw, T., Helmich, F. P., Phillips, T. G., et al. 2010, A&A, 518, L6
Di Francesco, J., Johnstone, D., Kirk, H., MacKenzie, T., & Ledwosinska, E. 2008, ApJS, 175, 277
Dionatos, O., Jørgensen, J. K., Green, J. D., et al. 2013, A&A, submitted
Dunham, M. M., Arce, H. G., Allen, L. E., et al. 2013, AJ, 145, 94
Dunham, M. M., Evans, N. J., Terebey, S., Dullemond, C. P., & Young, C. H. 2010, ApJ, 710, 470
Dunham, M. M., Evans, N. J., II., Bourke, T. L., et al. 2006, ApJ, 651, 945
Dzib, S., Loinard, L., Mioduszewski, A. J., et al. 2010, ApJ, 718, 610
Dzib, S., Loinard, L., Mioduszewski, A. J., et al. 2011, RMxAC, 40, 231
Enoch, M. L., Evans, N. J., II, Sargent, A. I., & Glenn, J. 2009, ApJ, 692, 973
Enoch, M. L., Young, K. E., Glenn, J., et al. 2006, ApJ, 638, 293
Evans, N. J., Dunham, M. M., Jørgensen, J. K., et al. 2009, ApJS, 181, 321
Fedele, D., Bruderer, S., van Dishoeck, E. F., et al. 2012, A&A, 544, L9
Fedele, D., Bruderer, S., van Dishoeck, E. F., et al. 2013, A&A, submitted
Fischer, J., & Gamache, R. R. 2002, JQSRT, 74, 263
Flower, D. R., & Pineau Des Forêts, G. 2010, MNRAS, 406, 1745
Furlan, E., Hartmann, L., Calvet, N., et al. 2006, ApJS, 165, 568
Giannini, T., Lorenzetti, D., Tommasi, E., et al. 1999, A&A, 346, 617
Giannini, T., Nisini, B., & Lorenzetti, D. 2001, ApJ, 555, 40
Goicoechea, J. R., Cernicharo, J., Karska, A., et al. 2012, A&A, 548, 77
Goldsmith, P. F., & Langer, W. D. 1999, ApJ, 517, 209
Haisch, K. E., Jr., Greene, T. P., Barsony, M., & Stahler, S. W. 2004, AJ, 127, 1747
Herczeg, G. J., Karska, A., Bruderer, S., et al. 2012, A&A, 540, A84
Higdon, S. J. U., Devost, D., Higdon, J. L., et al. 2004, PASP, 116, 975
Hirota, T., Honma, M., Imai, H., et al. 2011, PASJ, 63, 1
Hollenbach, D. 1985, Icar, 61, 36
Hollenbach, D. 1997, in IAU Symp. 182, Herbig–Haro Flows and the Birth of Stars, ed. B. Reipurth & C. Bertout (Dordrecht: Kluwer), 181
Hollenbach, D., & McKee, C. F. 1989, ApJ, 342, 306
Houck, J. R., Roellig, T. L., van Cleve, J., et al. 2004, ApJS, 154, 18
Johnstone, D., Wilson, C. D., Moriarty-Schieven, G., et al. 2000, ApJ, 545, 327
Jørgensen, J. K., Harvey, P. M., Evans, N. J., II, et al. 2006, ApJ, 645, 1246
Jørgensen, J. K., van Dishoeck, E. F., Visser, R., et al. 2009, A&A, 507, 861

Karska, A., Herczeg, G. J., van Dishoeck, E. F., et al. 2013, A&A, in press (arXiv:1301.4821)
Kassel, L. 1936, Chem. Rev., 18, 277
Kaufman, M. J., & Neufeld, D. A. 1996, ApJ, 456, 611
Kristensen, L. E., van Dishoeck, E. F., Bergin, E. A., et al. 2012, A&A, 542, A8
Kristensen, L. E., van Dishoeck, E. F., Tafalla, M., et al. 2011, A&A, 531, L1
Lahuis, F., Kessler-Silacci, J. E., Knez, C., et al. 2006, c2d Spectroscopy Explanatory Supplement (Pasadena, CA: Spitzer Science Center)
Lahuis, F., van Dishoeck, E. F., Jørgensen, J. K., Blake, G. A., & Evans, N. J. 2010, A&A, 519, A3
Launhardt, R., Stutz, A. M., Schmiedeke, A., et al. 2013, A&A, 551, A98
Lee, J.-E., Lees, S., Green, J. D., et al. 2013, A&A, submitted
Lefloch, B., Cabrit, S., Codella, C., et al. 2010, A&A, 518, L113
Lindberg, J. E., Jorgensen, J. K., & Herschel DIGIT Team. 2011, in IAU Symp. 280, The Molecular Universe, ed. J. Cernicharo & R. Bachiller (Cambridge: Cambridge Univ. Press), 235
Linke, R. A., Frerking, M. A., & Thaddeus, P. 1979, ApJL, 234, L139
Lorenzetti, D., Giannini, T., Nisini, B., et al. 2000, A&A, 357, 1035
Lorenzetti, D., Tommasi, E., Giannini, T., et al. 1999, A&A, 346, 604
Manoj, P., Watson, D. M., Neufeld, D. A., et al. 2013, ApJ, 763, 83
Maret, S., Bergin, E. A., Neufeld, D. A., et al. 2009, ApJ, 698, 1244
Meeus, G., Salyk, C., Evans, N. J., II, et al. 2013, A&A, submitted
Motte, F., & André, P. 2001, A&A, 365, 440
Myers, P. C., & Ladd, E. F. 1993, ApJL, 413, L47
Neufeld, D. A. 2012, ApJ, 749, 125
Neuhäuser, R., & Forbrich, J. 2008, in The Corona Australis Star Forming Region, Handbook of Star Forming Regions, Vol. II, ed. B. Reipurth (San Francisco, CA: ASP), 735
Nisini, B., Antoniucci, S., Giannini, T., & Lorenzetti, D. 2005, A&A, 429, 543
Nisini, B., Benedettini, M., Codella, C., et al. 2010, A&A, 518, L120
Nisini, B., Giannini, T., & Lorenzetti, D. 2002, ApJ, 574, 246
Nisini, B., Santangelo, G., Antoniucci, S., et al. 2013, A&A, 549, A16
Olofsson, S., & Olofsson, G. 2009, A&A, 498, 455
Ott, S. 2010, in ASP Conf. Ser. 434, Astronomical Data Analysis Software and Systems XIX, ed. Y. Mizumoto, K.-I. Morita, & M. Ohishi (San Francisco, CA: ASP), 139

Pilbratt, G. L., Riedinger, J. R., Passvogel, T., et al. 2010, A&A, 518, L1
Podio, L., Kamp, I., Flower, D., et al. 2012, A&A, 545, A44
Poglitsch, A., Waelkens, C., Geis, N., et al. 2010, A&A, 518, L2
Roelfsema, P. R., Helmich, F. P., Teyssier, D., et al. 2012, A&A, 537, A17
Rothman, L. S., Jacquemart, D., Barbe, A., et al. 2005, JQSRT, 96, 139
Santangelo, G., Nisini, B., Giannini, T., et al. 2012, A&A, 538, A45
Schöier, F. L., van der Tak, F. F. S., van Dishoeck, E. F., & Black, J. H. 2005, A&A, 432, 369
Sicilia-Aguilar, A., Henning, T., Linz, H., et al. 2013, A&A, 551, A34
Sturm, B., Bouwman, J., Henning, T., et al. 2010, A&A, 518, L129
Sturm, B., Bouwman, J., Henning, T., et al. 2013, A&A, 553, A5
Tafalla, M., Liseau, R., Nisini, B., et al. 2013, A&A, 551, A116
van Dishoeck, E. F., Kristensen, L. E., Benz, A. O., et al. 2011, PASP, 123, 138
van Kempen, T. A., Green, J. D., Evans, N. J., et al. 2010a, A&A, 518, L128
van Kempen, T. A., Kristensen, L. E., Herczeg, G. J., et al. 2010b, A&A, 518, L121
van Kempen, T. A., van Dishoeck, E. F., Salter, D. M., et al. 2009, A&A, 498, 167
Vasta, M., Codella, C., Lorenzani, A., et al. 2012, A&A, 537, A98
Visser, A. E., Richer, J. S., & Chandler, C. J. 2002, AJ, 124, 2756
Visser, R., Kristensen, L. E., Bruderer, S., et al. 2012, A&A, 537, A55
Wampfler, S. F., Bruderer, S., Karska, A., et al. 2013, A&A, 552, A56
Wampfler, S. F., Herczeg, G. J., Bruderer, S., et al. 2010, A&A, 521, L36
Watson, D. M., Bohac, C. J., Hull, C., et al. 2007, Natur, 448, 1026
Werner, M. W., Roellig, T. L., Low, F. J., et al. 2004, ApJS, 154, 1
Wilson, C. D., Avery, L. W., Fich, M., et al. 1999, ApJL, 513, L139
Wu, J., Dunham, M. M., Evans, N. J., II, Bourke, T. L., & Young, C. H. 2007, AJ, 133, 1560
Yang, B., Stancil, P. C., Balakrishnan, N., & Forrey, R. C. 2010, ApJ, 718, 1062
Yıldız, U. A., Kristensen, L. E., van Dishoeck, E. F., et al. 2012, A&A, 542, A86
Yıldız, U. A., Kristensen, L. E., van Dishoeck, E. F., et al. 2013, A&A, submitted
Young, C. H., & Evans, N. J., II 2005, ApJ, 627, 293
Young, C. H., Jørgensen, J. K., Shirley, Y. L., et al. 2004, ApJS, 154, 396